A MICROFLUIDICS APPROACH TOWARDS THE INVESTIGATION OF FREE HEME EFFECTS ON SICKLE CELL HEMOGLOBIN POLYMERIZATION

A Thesis

Presented to

the Faculty of the Department of Chemical and Biomolecular Engineering

University of Houston

In Partial Fulfillment

of the Requirements for the Degree

Master of Science

in Chemical Engineering

by

Anupam Aich

May 2012

ACKNOWLEDGEMENTS

I would like to express my heartfelt gratitude to my thesis advisor, Dr. Peter G. Vekilov, for his sincere, insightful and timely remarks throughout the research work, which has been essential for bringing this thesis to reality. His continuous motivation has worked as a strong driving force in bringing the best out of me.

I would also like to extend my gratitude to Dr. Jeffrey Rimer and Dr. Vassiliy Lubchenko for serving on my thesis committee. I would like to especially thank my colleague Dr. Elena V. Petrova, without her continuous mentoring and suggestions this research would not have been possible. Her technical guidance and helping with experiments paved the way towards realization of the project.

I would also like to thank Dr. Kelley R. Bradley and Dr. Shivakumar Bhaskaran for their extensive and continuous support in UH Nanofabrication Facility. I would also like to thank Dr. Dong Liu for his suggestions and Aritra Sur for performing the computer simulations.

I would like to thank my co-workers Ye Li, Duong Lam, Katelyn Tran and K.C. Schuette for their contribution to various phases of the project. I am thanking Maria Vorontsova, Dmitry Galushko and Melissa Freundlich for their encouraging comments.

I would also like to thank Dr. Gila Stein, Dr. Jacinta Conrad and Dr. Paul Ruchhoeft for their valuable suggestions at different stages of the project. I would like to thank my friends whose continuous support was always the best part to cherish. Finally, I am grateful to my beloved parents and my brother, who have always been supportive and encouraging to me in the time when I needed them most.

A MICROFLUIDICS APPROACH TOWARDS THE INVESTIGATION OF FREE HEME EFFECTS ON SICKLE CELL HEMOGLOBIN POLYMERIZATION

An Abstract

of a

Thesis

Presented to

the Faculty of the Department of Chemical and Biomolecular Engineering

University of Houston

In Partial Fulfillment

of the Requirements for the Degree

Master of Science

in Chemical Engineering

by

Anupam Aich

May 2012

ABSTRACT

Sickle cell hemoglobin (HbS) polymerization is considered to be the primary pathogenic event in sickle cell anemia. In this work we aim at fabricating an integrated microfluidic device with a localized microheater for the study of HbS polymerization kinetics. We developed fabrication recipes for both an SU-8 based microchannel and a thin film resistive Cu-Cr microheater.

We calibrated the heater with both infrared camera and Peltier element and found that a limit exists on the power input to the heater. Computer simulations were carried out to find time resolution of heating process and also the temperature field. Bonding recipe for chip integration has been developed. Surface characterization techniques such as AFM and measuring contact angle with goniometer were used to confirm that oxygen plasma enhances hydrophilicity in SU-8 layer. We found the bonding temperature from differential scanning calorimetry data. Plug flow of liquid in channel has been observed.

TABLE OF CONTENTS

LIST OF FIGURES

LIST OF TABLES

CHAPTER 1

INTRODUCTION

Sickle cell anemia is a hemolytic anemia with acute and chronic manifestations (1). The current treatment options have downsides or significant adverse effects and the search for alternative therapeutic options continues.

Many cellular and molecular factors are implicated in the pathogenesis of sickle cell anemia, but the polymerization of a mutant hemoglobin, called sickle cell hemoglobin (HbS), which is expressed in the erythrocytes of sickle cell patients, is considered the primary event (2). The polymers stretch and rigidify the erythrocytes and alter the normal composition of the erythrocyte membrane (3). Results with transgenic mice expressing human HbS (4) have demonstrated that delaying polymerization inhibits red blood cell sickling and ameliorates two of the disease symptoms. Thus, despite past disappointments and frustrations, slowing the polymerization rate is a practical venue in the search of additional therapeutic strategies for sickle cell anemia.

Our group has recently found that the kinetics of polymerization are profoundly sensitive to the concentration of free heme (5). Heme may be excessively released in sickle erythrocytes due to autoxidation of HbS to unstable met-HbS (6). The sole determination of the mean concentration of free heme in sickle red cells has yielded a relatively low value of < 1 μM (7), but its variation and response to environmental stress is unknown.

Further work will test if *free* heme is a significant factor for the polymerization of sickle cell hemoglobin (HbS). These tests consist of the search for answers to two scientific questions: (i) Does the absence of free heme delay or arrest HbS

polymerization? and (ii) To what extent do heme concentrations of order 10-100 μM affect the rates of nucleation and growth of HbS polymers?

To test the hypothesis of the free heme effects, the rate of HbS polymerization needs to be tested in a huge field of concentrations of free heme and hemoglobin. The enormity of this task defines the need for a new experimental technique. The design of this technique was the main objective of the work discussed here.

Correspondingly, this thesis consists of the following six parts:

In Chapter 2, I review the current state-of-the-art in the area of sickle cell hemoglobin polymerization and the recent findings of effects of free heme on the kinetics of this process.

In Chapter 3, I discuss the design considerations of a microfluidics device which will allow high-throughput determinations of the rate of sickle cell hemoglobin polymerization in the presence of heme. Here I also discuss the fabrication procedure and processing conditions for microchannel in the low volume microfluidic chip.

In Chapter 4, I discuss the fabrication of localized thin film heater, another integrated part of the microfluidic chip. Fast egress to required sickle cell hemoglobin (HbS) supersaturation is the requirement and I discuss the processing parameters and calibration procedure of the heater. I also discuss the simulations performed and the results obtained. I compare the experimental data with the simulation results.

In Chapter 5, I discuss the bonding procedure of two segments of the microfluidic device: microfluidic channel and localized microheater. I also discuss surface

characterizing techniques used and parameters crucial for ensuring good adhesion between the two parts.

In Chapter 6, I discuss the management and control schemes of the microfluidic device. Fast temperature control and HbS aqueous solution droplet generation are the most crucial parameters for HbS polymer nucleation experiment.

In Chapter 7, I formulate the main conclusions of this work and indicate possible future studies.

CHAPTER 2

SICKLE CELL HEMOGLOBIN POLYMERIZATION & FREE HEME EFFECTS

2.1. Hemoglobin and Heme

2.1.1. Hemoglobin

Hemoglobin, found in red blood cells of all of the vertebrates and some invertebrates, is an iron containing metalloprotein which carries oxygen to cells (8). In humans it takes the oxygen from the lungs at a pressure of about 100 torr and then delivers it to the cells where the oxygen pressure is lower, about 40 torr. The oxygen affinity increases with increasing saturation in the hemoglobin and this leads to the co-operative binding of oxygen to hemoglobin. The word "hemoglobin" was coined by Felix Hoppe Seyler in 1866 (9). Hemoglobin is a hetero-tetramer protein with 4 sub-units ($\alpha_2\beta_2$) in quaternary structure which was the first protein to be characterized by X-Ray crystallography by Max Perutz (10). The heme molecule at the center of these four sub-units is the iron-containing molecule which is responsible for the red color of blood. The four oxygen molecules that bind to hemoglobin are bound at the sites where the four monomer globins are attached to the respective heme molecules (8,11). This oxygen binding is parameterized by different factors and is co-operative meaning the more the oxygen is added the more the affinity of the molecule towards oxygen increases.

The normal adult hemoglobin molecule (HbA) weighs about 64650 g/mol and has two α subunits of 141 residues each and two β subunits (figure 2.1.)(12) of 146 residues each (13). The non-α subunits in normal and different hemoglobin variants (β, γ or δ) are the primary reason for the variation in the characteristics. Fetal hemoglobin, containing

the γ sub-units, is mostly found in fetuses and new-born infants. As age increases, the genes expressing the fetal hemoglobin are repressed and the adult hemoglobin (HbA) becomes prevalent. The lowest contributor (2.5%) of total adult hemoglobin is the δ chained hemoglobin A2 (11). The three different non-α sub-units (β, γ or δ) have the same length while they differ in the constituent residues governing their functions.

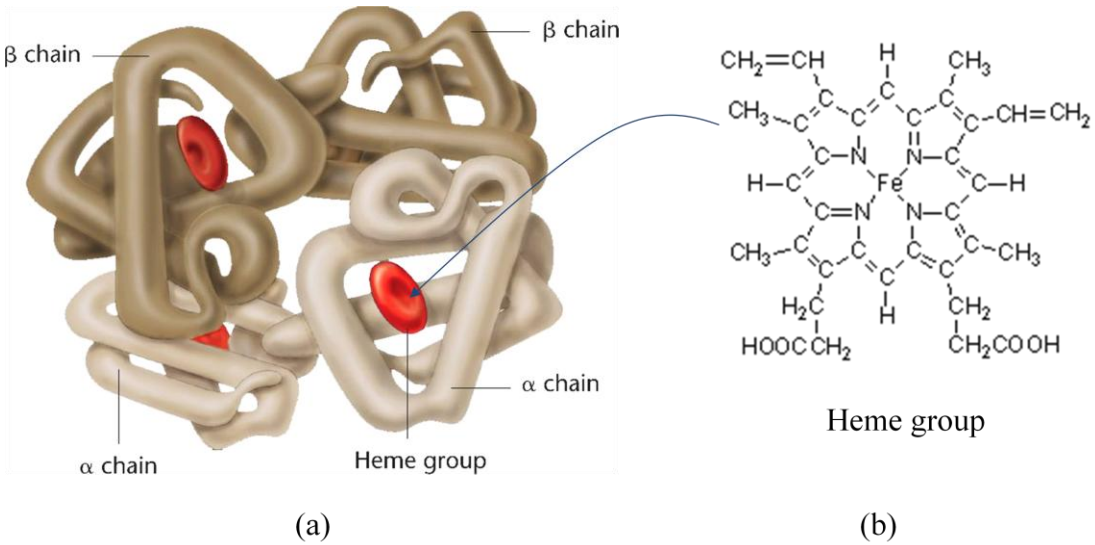

Figure 2.1. (a) Schematic of quaternary structure of hemoglobin showing α-β subunits and heme pockets. (b) Structure of heme molecule. (12)

2.1.2. Heme

The four sub-units in hemoglobin molecules form interface with each other mainly through hydrophobic contacts and each has a hollow centre where there is heme as a prosthetic group as it can be seen from the figure 2.1. Thus one hemoglobin molecule contains four heme group within it. Heme is a porphyrin derivative which has four methane bridge pyrrole rings (8). The groups attached to the pyrrole rings can vary and this gives rise to different classes of heme. This porphyrin derivative in human hemoglobin, known as protoporphyrin IX (b-type heme) and containing four methyl, two propionate and two vinyl substituent, has a iron Fe(II) atom bound at its centre and this

iron atom is responsible for the co-ordinated binding of oxygen molecules to hemoglobin (14). The other types of heme are heme-a and heme-c. The a-type heme has a formyl group instead of a methyl group and the c-type has vinyl-thioether in place of vinyls. These variations result in changes in fundamental chemistry and has been found that the c-type hemes are co-valently bound(15) to hemoproteins while a and b-types are not. This characteristic facilitates easy removal of heme from the hemoproteins and thus under specific conditions heme may act as cell signaling messengers through reversible binding with hemoproteins.

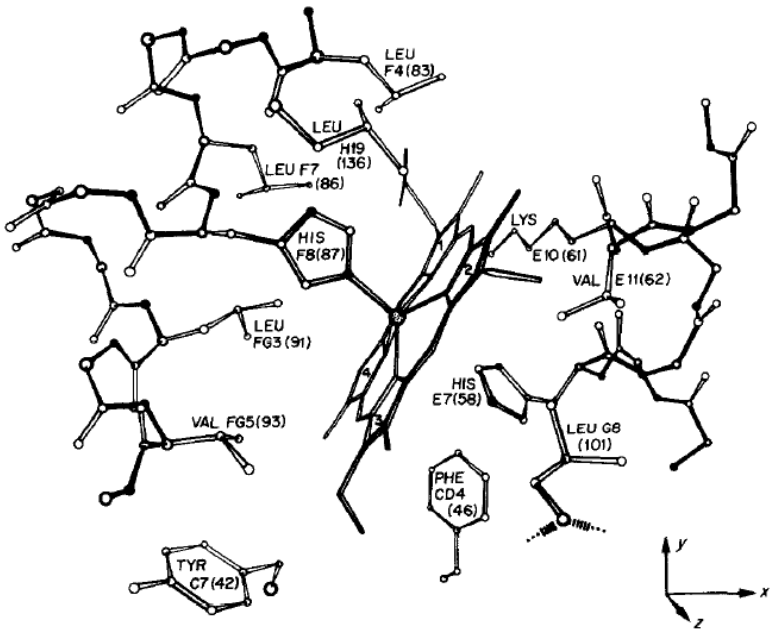

Figure 2.2. Heme group in its environment in an unliganded α chain. Selected side chains are shown omitting heme-4-propionate. (15)

The solubility of free heme is in the millimolar range (determination in our laboratory yielded ~ 2 mM) (5), similar to many other hydrophobic compounds (16). Heme is mostly found attached to the membrane and cytoskeleton of the red cell (7,17-22); however, heme attachment to the cell membrane is driven by thermodynamics of hydrophobicity, similar to that of heme crystallization. Thus, at equilibrium between the

cytosol and the membrane-attached state, heme concentration in the cytosol may be comparable to this solubility. Since the erythrocyte membrane does not contain pores sufficiently wide for the passage of the relatively large heme molecules, a likely mechanism of heme removal is crossing the lipid bilayer of the cell membrane. The interactions of heme with the membrane are complicated and not completely understood.

Heme toxicity for the cells is well documented. In vitro heme is a potent lytic agent for erythrocytes (23,24) and some eukaryotes, including the malaria agents *Plasmodium berghei* (25) and *Plasmodium falciparum* (26). Heme is toxic to neuron, neuron-like and myocardial cell cultures (27-29). Several human pathological conditions are related to levels of heme inside the erythrocyte or in plasma and tissues increased due to intra- and extravascular hemolysis. Accordingly, heme toxicity plays an important role in hemorrhages and hemorrhagic infarctions of the central nervous system (27,28), congenital Heinz body hemolytic anemia (30), glucose-6-phosphate-dehydrogenase deficiency (31). Heme is a powerful *in vitro* inducer of low-density-lipoprotein (LDL) oxidation and is thus implicated in the development of atherosclerosis *in vivo* (32,33).

2.1.3. T-R conformation of hemoglobin and O_2 dissociation curve

The binding of oxygen with hemoglobin is accompanied by change in the conformation of the molecule. In the deoxy state, the iron atom has five co-ordination bonds with four nitrogens from each of four pyrrole rings and the other with *His* ligand of the corresponding sub-unit of the hemoglobin. So when hemoglobin is oxygenated, the iron binds the oxygen to its another co-ordination site octahedrally, thus changing the electronic configuration of Fe (II). This governs the color change of the blood from dark

purple to the scarlet. The co-ordination between the oxygen and the Fe(II) atom happens on the opposite side to the His ligand of the sub-unit (8). So four sub-units bind four oxygens at the site of their attachment with heme molecule. The deoxystate is known the **Tense (T) state** of the ligand while oxy state is known as **Relaxed (R-state)** and the quaternary structures of these two states are quite different (8,11,34).

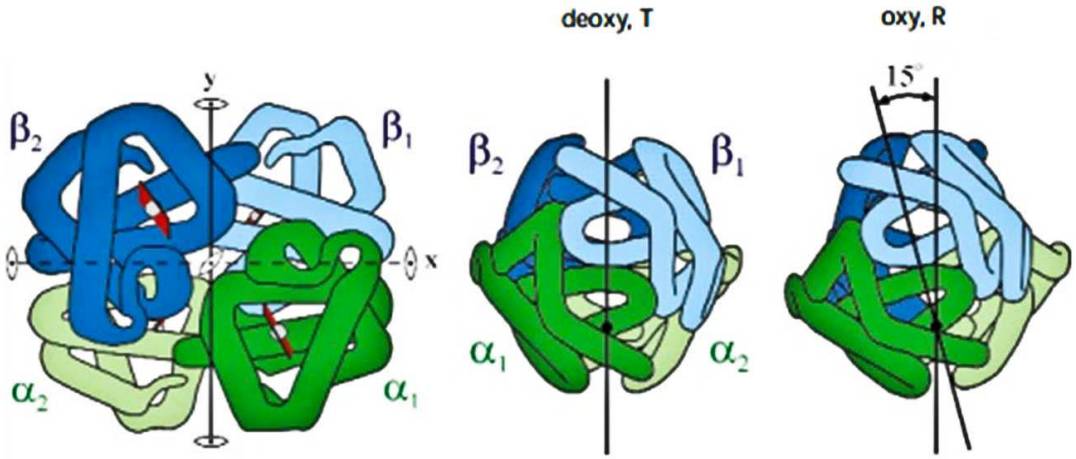

Figure 2.3. Conformational transition of hemoglobin molecule between T (deoxy) state and R (oxy) state (34). Rotation of symmetrically related αβ dimers by ~15˚ relative to each other and translation of ~0.1 nm along the rotational axis is shown here.

The co-operative binding of the oxygen with hemoglobin is represented by a sigmoid shaped curve when the saturation is plotted as a function of the oxygen partial pressure representing the oxygen concentration. The O_2 dissociation curve shown in figure 2.4 (35) implicates the fact that the conformational change of the protein takes place in a very narrow range of O_2 saturation. This addresses the shift in the affinity of the hemoglobin molecule for the oxygen molecule as it binds one after another.

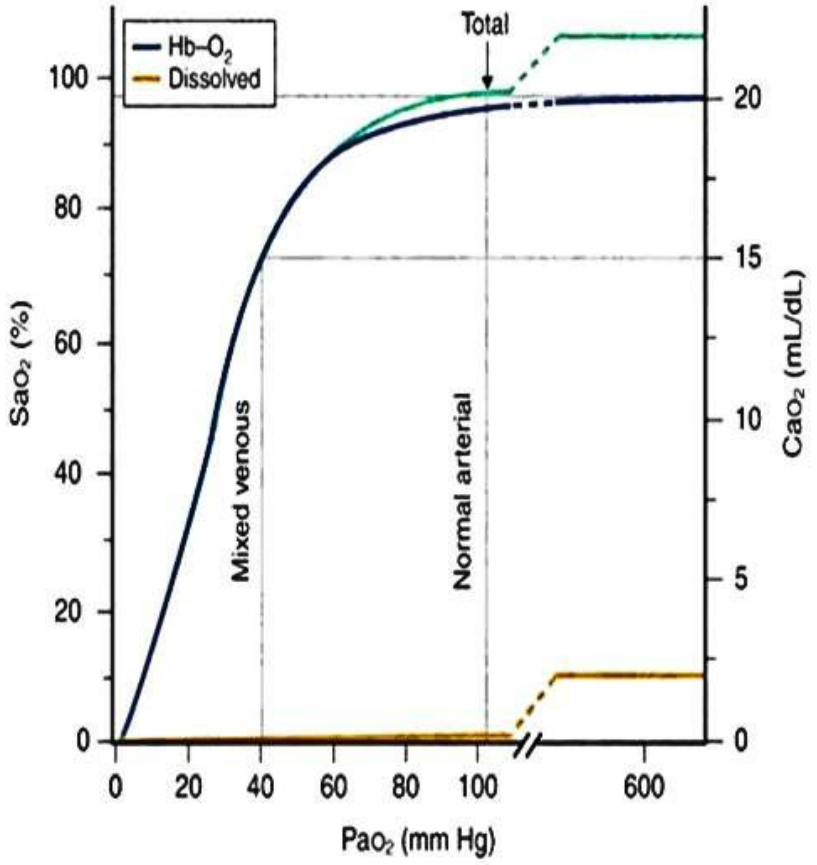

Figure 2.4. The oxyhemoglobin association-dissociation curve. The axis for Sao_2 is oxygen saturation and Cao_2 is arterial content of oxygen. Cao_2 is the sum of the oxygen dissolved in plasma (denoted "Dissolved" in the figure) plus the oxygen bound to hemoglobin (Hb-O_2). (35)

The reversible reaction of oxy-deoxy states of hemoglobin can be written as follows (11):

$$Hb_4^{\,T} \xleftrightarrow{LC^n} Hb_4^{\,R}, \qquad .(2.1)$$

where, n = number of ligands bound to Hb

$$L = [Hb_4^{\,T}]/[Hb_4^{\,R}]$$

$$C = K_R/K_T;$$

(K_R and K_T are the ligand dissociation constants in the R and T states, respectively.)

So from the reaction above the fractional saturation of oxygen bound to hemoglobin can be found from the equation below:

$$Y_{O_2} = \frac{(pO_2)^n}{K + (pO_2)^n} . \quad (2.2)$$

Equation 2.2 is known as the Hill equation. It was formulated by Archibald Hill in 1910. Y_{O_2} is oxygen saturation and pO_2 is the partial pressure. K here is the dissociation constant and n is the ligand number. When we plot Y_{O_2} vs. pO_2 *(in figure 2.4 depicted as* Sao_2 *vs.* Pao_2*)*, it gives a sigmoidal graph. It can be seen that Y_{O_2} = 0.95 at 100 torr which is close to the pressure in the lungs (95 torr) and Y_{O_2} = 0.55 at 30 torr which is close to pressure in the tissues (0.40 torr). This means about 0.40 fraction of the oxygen consumed in the lungs is delivered to the tissues. This understanding is of great physiological importance. This means the initial oxygen addition to the T-state of hemoglobin gives rise in the oxygen affinity leading to faster saturation at high oxygen pressure and vice versa.

The reversible reaction of oxygen association and dissociation can be modeled as two-state model of R and T-states which can be explained by both (i) Monod, Wyman, and Changeux (MWC) model and (ii) sequential model by Koshland, Nemethy, and Filmer (36). The MWC model postulates that the conformational change in one sub-unit of the protein lead to induction for conformational change in the other sub-unit i.e., all the sub-units should be present in same conformation at the same time whether it is T or R-state. The equilibrium between two states has a shift depending on the presence of substrate. On the other hand, the sequential model states that the conformational change are not interdependent and change of conformation in one subunit is not propagated

through the structure. The change only slightly alters the activity of the other sub-units which in turn leads to binding to other (allosteric) sites. Experimental evidences are present both in favor of both the mechanisms and thus the combined mechanism may prevail in the nature (36).

2.2. Sickle Cell Anemia

2.2.1. Definition and manifestations

Protein aggregations in physiological conditions lead to rise of different forms of pathological conditions. Sickle cell anemia, such a disease, is the first molecular disease to be discovered which is caused due to genetic disorder leading to mutation in hemoglobin genes. Thus Sickle Cell Anemia (SCA) is a hemolytic anemia having both chronic and acute manifestations arising from the polymerization of Sickle cell hemoglobin (HbS) in its deoxygenated **T state (2,37)**.

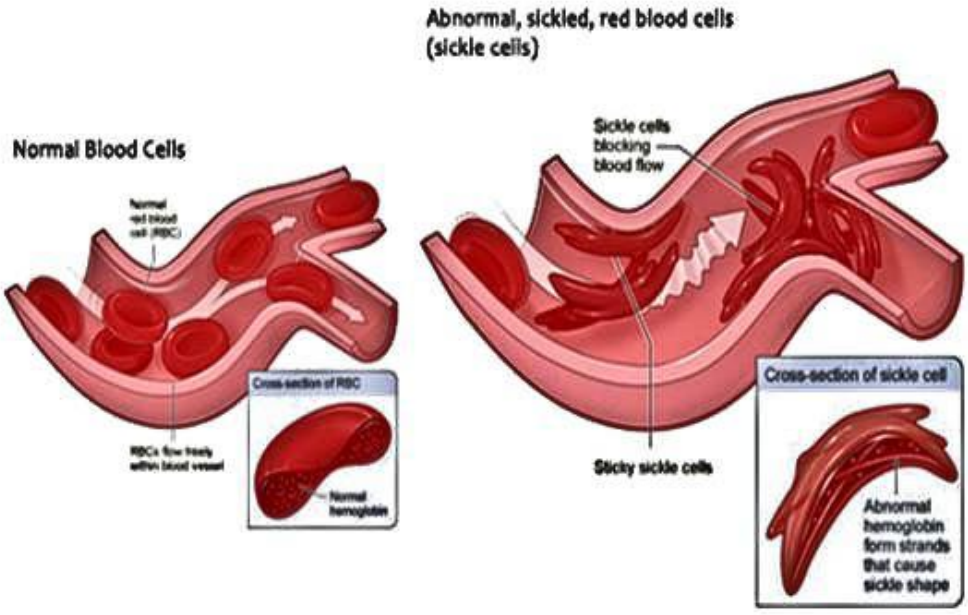

Figure 2.5. Cross-sectional view of blood flow in both normal and sickle cell patient circulation system. (38)

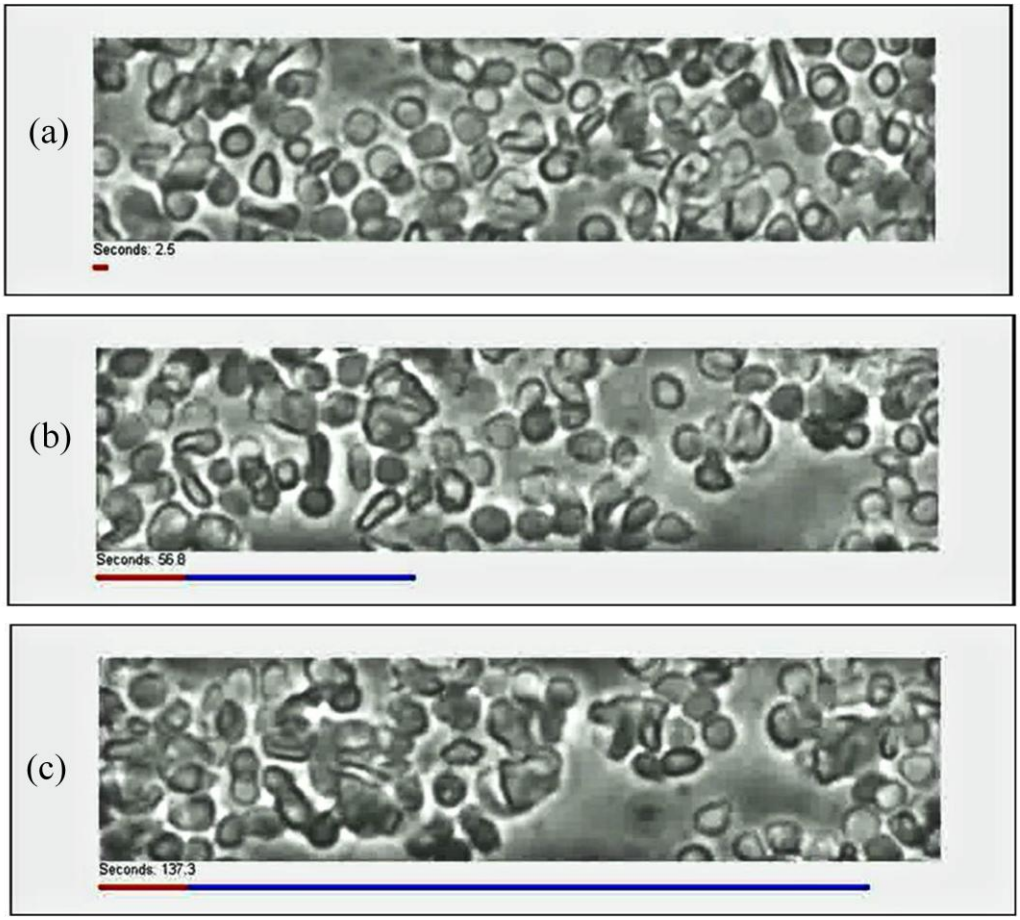

Figure 2.6. Snapshots from a movie of vaso-occlusion process from Higgins *et al*. (39)

The polymers of HbS deform the shape of the discoid erythrocytes from which the name "Sickle" arises and also increase the viscosity of the red blood cells (RBC). The acute vaso-occulsion is the result of blockage of flow in the blood vessels (figure 2.5 (38)) due to induced high viscosity of the blood originating from the deformed RBCs which introduces severe pain in those areas and is also known as sickle cell pain crisis. Not only the viscosity of the RBCs, but also interactions between endothelium, plasma factors, leucocytes and rigid sickled blood cells may lead to vaso-occlusion. The vaso-occlusive crises generally cause pain in bones, chest and abdomen and they may affect any tissue. Spleen infarction is very common demonstration of the crises causing severe abdominal pain. Figure 2.6 (39) shows snapshots from a movie of simulated vaso-

occlusion in a microfluidic device. In the experiment deoxy-HbS containing blood was subjected to oxygen environment. (a) At initial moments the blood contains low amount of deformed erythrocytes so the RBC distribution is uniform throughout field of view. (b) As the time progresses oxygenated HbS go under polymerization and RBCs deform resulting in higher rigidity and loss of velocity in the flow, the RBC distribution is less uniform. (c) As more time pass the rigidity and deformation of RBCs reach extreme level and agglomeration of RBCs is observed and eventually the flow stops after some time.

Hemolytic crisis is the chronic manifestation arising from RBC deformation and lowering of RBC life from 120 days to 17 days (13). The rigid deformed shape of sickled RBCs make them susceptible to extravascular (mostly) and intravascular destruction and thus lowering of RBCs in the blood stream lead to anemic condition of patients suffering from the disease. This may lead to formation of bile stones, jaundice and gallstones etc..

Sudden pooling of RBCs in the spleen (mostly) and other places in the body may lead to cardiovascular failure and/or hypovolemic shock. Children and infants having both sickle cell genes and thelassimea genes may undergo this crisis known as acute sequestration crisis. The crisis happens due to the lowering of hemoglobin to a level less than 6 g/dl (major crisis) or closer to 6 g/dl (minor crisis) (1).

The hemolytic condition of sickle cell patients may sometimes be aggravated due to lowering in output from bone marrow which in conjugation with low RBC counts may lead to massive lowering of hemoglobin level. This is known as aplastic crisis.

Apart from the clinical manifestations discussed above, the sickle cell patients may have abnormal growth (in case of children), bone abnormalities (swelling of dorsal

surfaces known as "hand-foot syndrome, medullary irregularities, osteosclerosis, bone pain due to osteonecrosis and arthritis manifestations), kidney infarctions causing renal failure, priaprism causing permanent impotence in adults, Splenomegaly & splenic fibrosis, hepatomegaly (common in sickle cell patients leading to enlargement of liver, formation of gallstones), cardiopulmonary infarctions (*acute chest syndrome*, *corpulmonale* due to combined increased flow rate and pulmonary vaso-occlusions), retinal vessel obstruction or *sickle retinopathy* (resulting in hemorrhage, scarring, retinal detachment and blindness), cerebrovascular infarctions (prevalent in children), hemorrhagic strokes (prevalent in patients of 20-29 age), leg ulcers (common major source of morbidity), higher rate of infections (single most reason for hospitalization sickle cell patients), and pregnancy complications (pulmonary infarctions, acute chest syndrome, prematurity, fetal death etc.) (1). These manifestations lead to death in extreme severity decreasing the life expectancy of the adult homozygous sickle cell patients to the order of 40 years and till date, apart from hydroxyurea which is only 50% successful in healing patients there has been found, no substantial drug which can inhibit the polymerization or at least decrease the severity to a substantial extent. The only clinical procedure available is regular transfusion of blood and for cure from the disease, is replacement of bone marrow which might be dangerous for the patient from immunological point of view. Thus search for a reliable treatment strategy and preferable cure is under investigation throughout the scientific world where teams of engineers, physicists, chemists, physicians are working together to better understand the pathophysiology, kinetics, molecular, genetic, and other factors which may contribute to the proliferation of this disease.

2.2.2. SCA epidemiology, history and molecular basis

SCA is an evolutionary genetic disorder which is prevalent in populations originated from four specific regions. The African haplotypes are originated in the areas of Batun, Benin and Senegal and another independent origin has been found to be of Asian haplotype mainly in Saudi Arabia and central part of India. Due to migration of people from these regions, now SCA heterozygosity is found to be among 8% of African-Americans and also in populations of Southern Europe and the Caribbean with different frequencies of occurrence. Sickle cell heterozygous people are known as having "sickle cell traits" and has been found to have some resistance against malaria. SCA homozygous people are exposed to different complexities of physical crises and the severity of the disease extends from simple occurrences of painful crisis to higher morbidity with variation of the ages ranging from new born infants to 40 years old persons (40).

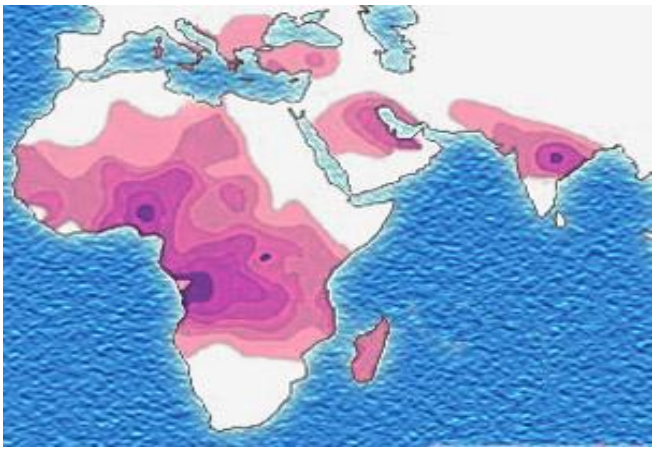

Figure 2.7. Prevalence of Sickle Cell Disease around the world. (40)

SCA was first reported by James Herrick in 1910 (41) when he found deformed shaped erythrocytes in the blood of a young African patient who was suffering from severe pain crisis in several places at different stages of his life. While Emmel's findings

indicated towards genetic inheritance of the SCA trait and microvascular obstructions were found to be the prime reason for the painful crises in 1934, Hahn and Gillespie recognized the contribution of deoxy state of the HbS to the polymerization. In 1949 Linus Pauling (42) suggested that two extra positive charges are found to be on the surface of HbS molecule when it is compared with HbA molecule and the birefringence observed by Sherman (1940) indicated existence of an ordered structure (13).

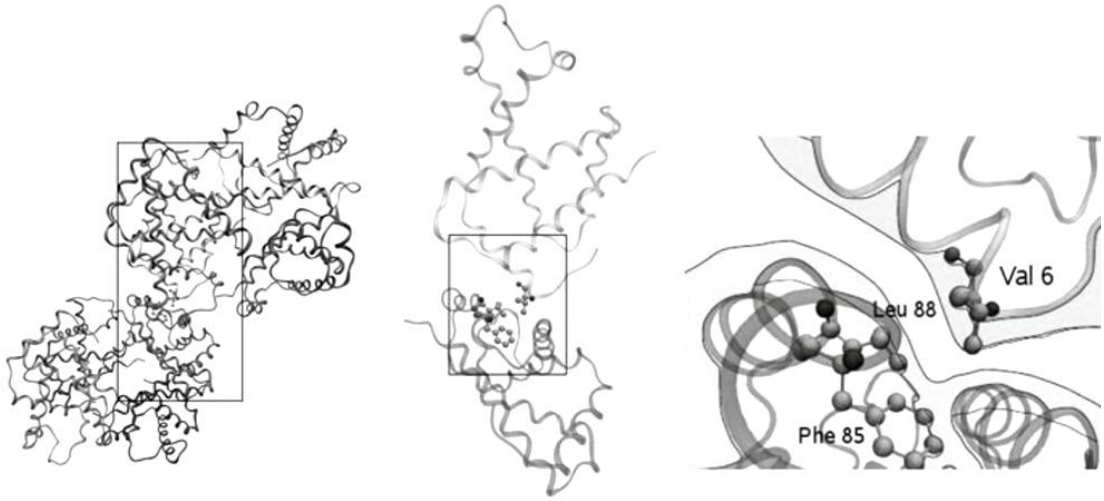

(a) (b) (c)

Figure 2.8. Donor and acceptor during deoxygenated states of sickle cell hemoglobin: (a) global view, (b) enlarged view from (a), and (c) closest view of donor and acceptor. (45)

These observations lead to the extensive study of peptide fingerprinting by Ingram (43) and he found that the homozygous genetic disorder comes from a single mutation of human hemoglobin genes. This is attributed to the change from GTG to GAG in the sixth codon of the ß6 gene (44) which encodes for the nonpolar valine instead of glutamic acid on the surface of the ß-globin (figure 2.8 (45)). Thus SCA became the first molecular disease to be identified.

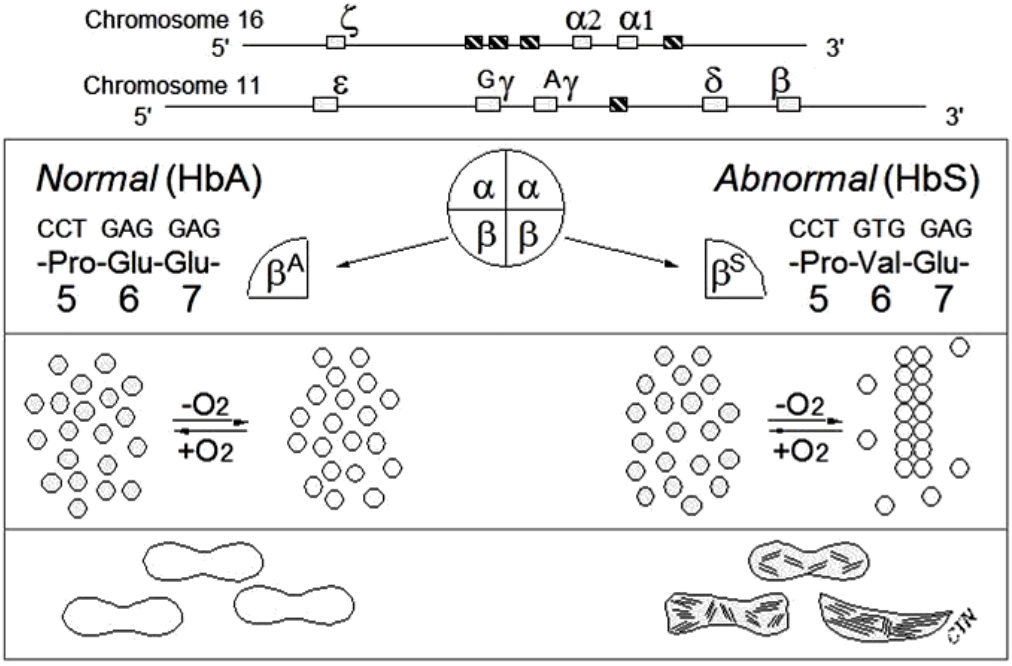

Figure 2.9. Genetic basis of differences between HbA and HbA and its consequences (44). The position of hemoglobin genes in human chromosomes. It also shows the differences between genetic configurations of normal adult hemoglobin and sickle cell hemoglobin; the oxygenated and deoxygenated form of two hemoglobins and the final form of the erythocytes.

2.3. Sickle cell anemia and HbS polymerization

In 1950 Harris suggested that the birefringent structures in the erythrocyte come from polymerization which confirmed the observation of Perutz and Mitchison opposing single ordered crystals (13). The transition to nonpolar valine on the surface of HbS though does not change the conformation of the protein, in the deoxy state of sickle cell hemoglobin the surface of the ß chain which has nonpolar valine is induced to have hydrophobic contact (46) with other nonpolar residues from other HbS molecules such as with leucine, alanine and phenylalanine. This leads to the formation of 14 member fiber which is composed of seven double strands in staggered fashion. The arrangement consists of two contacting regions known as diagonal contact between molecules named

lateral contact and axial contact region which is not so specific. Figures 2.10 (47) and 2.11 (48,49) demonstrate the contacts between the molecules forming the polymers.

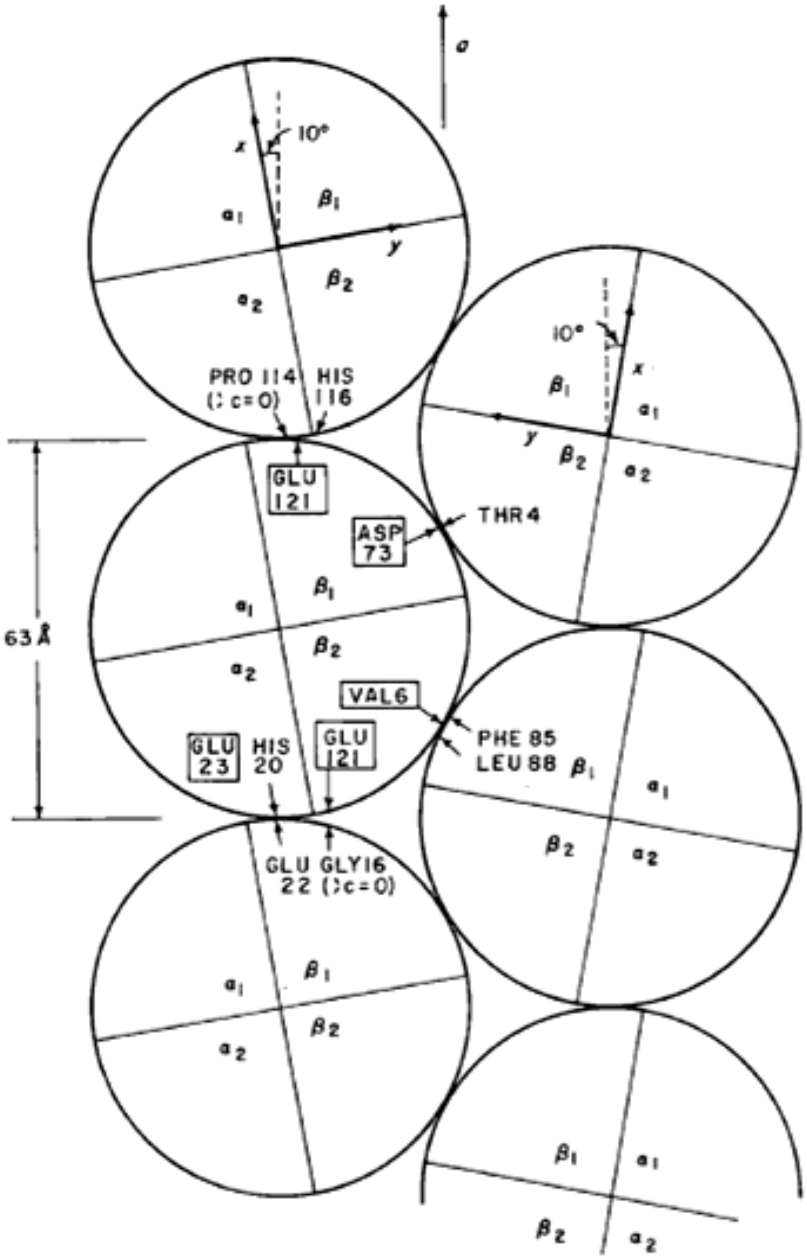

Figure 2.10. The intermolecular contacts in the crystal structure of deoxy HbS (47). It is important to note that the intermolecular contacts are only associated with Val 6β of subunit β_2, Val 6 of subunit β_1 is free.

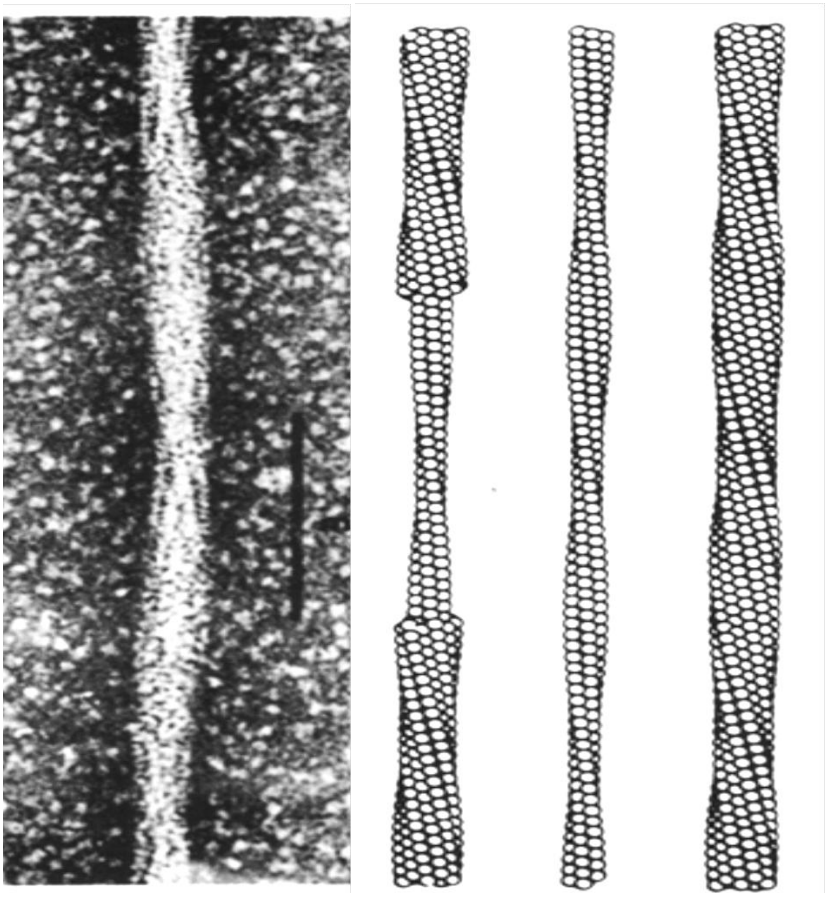

(a) (b) (c) (d)

Figure 2.11. (a) Scanning electron micrograph of HbS fibers. (b), (c) and (c) show the model of HbS polymer from image reconstruction of SEM images. (b) the outer 10 strands, (c) the inner core of 4 strands and (c) both inner and outer strands. (48, 49)

2.3.1. Nucleation mechanism and contradictions regarding primary pathogenic event revisited

The polymerization of sickle cell hemoglobin is a first order phase transition (due to the constant density and structure of the polymer) in its deoxy state at low oxygen pressure (46). This event has shown up to 50th order i.e., exponential dependence of the characteristic time for the nucleation on the hemoglobin concentration in the red blood cells (50). This is has been predicted by **double nucleation mechanism** of hemoglobin polymerization kinetics and also validated experimentally by Cao *et al* (51-53). The

double nucleation mechanism was first proposed by Ferrone *et al* in 1980 (46) and was directly observed. The mechanism introduces that there are two consecutive pathways for the entire polymerization reaction: ***Homogeneous nucleation*** is the first step and also the rate limiting step of the double nucleation mechanism for HbS polymerization. In this step in a HbS solution, with no polymer present, under oxidative stress the monomers spontaneously come together to form aggregates which are 14 stranded polymer nucleus having a finite number of polymers. These act as nucleus (2) to induce further growth of the polymer aggregates which in turn reduces the intrinsic instability of the "homogeneous" nucleus and form a larger polymer aggregate that acts as substrate or site for growth and branching of the HbS polymers; this step is known as ***Heterogeneous nucleation***. These aggregates from heterogeneous nucleation have greater stability than the smaller aggregates formed from homogeneous nucleation.

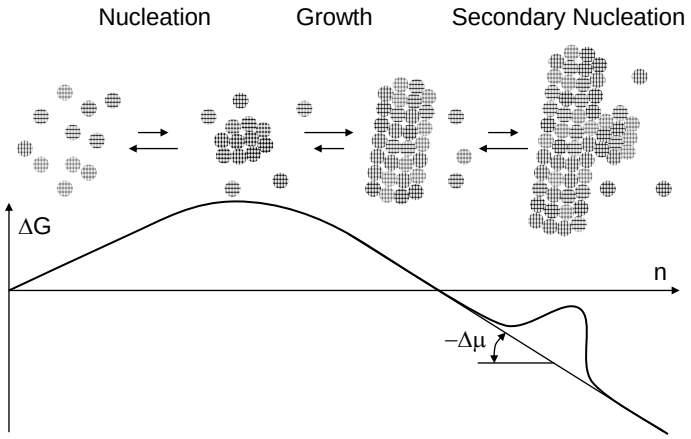

Figure 2.12. Schematic of the formation of sickle-cell hemoglobin (HbS) polymers in a supersaturated HbS solution. (2).

In figure 2.12 three major steps of double nucleation mechanism are highlighted: homogeneous nucleation of polymer fibers, their growth, and their branching by heterogeneous nucleation of new fibers on top of existing ones. The changes in the free

energy G of the system are schematically plotted as a function of the number of molecules n, which transfer from the solution to the polymer. The starting point of *G* is its value in the supersaturated HbS solution. The homogeneous formation of nuclei is accompanied by an increase of G, growth leads to lowering of *G*, the heterogeneous formation of secondary nuclei overcomes a G-barrier lower than the one for homogeneous nucleation. The slope of the decreasing *G* during the growth of a new phase is the solution supersaturation with respect to the polymer.

The first test and first triumph of the double nucleation mechanism was the understanding of the time dependencies of the degree of HbS polymerization, which consist of delay time and sharp increase, followed by saturation. These dependencies, while common for first-order phase transitions (HbS polymerization was shown to be such a transition (54,55), were unusual from the viewpoint of chemical and biochemical kinetics (51,56-58). The double nucleation mechanism helped to rationalize several features of the disease and the action of several treatment strategies: The higher severity of disease in patients with acidosis was explained with the decrease of HbS solubility at lower pH and the resulting increase in the driving force for polymerization (59). The rationale for the hydroxyurea (60) and dehydration prevention (61) treatments was based on the reduction of HbS activity. The long term effects of hydroxyurea were attributed to the enhanced expression of fetal hemoglobin in adults which reduced the HbS concentration and its activity (62,63). Similarly, hydration reduces HbS concentration and activity by increasing the water content of the red cells (64).

The molecular-level data on the variant hemoglobin and the fiber structure gave rise to hope that understanding of HbS polymerization, the initiator of the sequence, will

lead to cure (65). A treatment avenue was suggested: to find a hemoglobin ligand, which directly or through allostery would prevent the hydrophobic contact and the formation of the fiber (66-69). After more than 30 years of research, yielding about 200 molecules which, in vitro, bind to hemoglobin and prevent polymerization, this hope has not been fulfilled (70). A major obstacle for antisickling drugs has been the high concentration of hemoglobin inside the erythrocytes, ~5 mmol l^{-1}, which requires unacceptable concentrations of a ligand targeting most HbS molecules (71).

The clinical failure of the above linear scenario, initiated by polymerization, has been compounded by a plethora of observations which appear to contradict it (72,73). It was found that: more than half of the red cells of sickle cell patients undergo sickling on every passage through the venous circulation, yet sickle cell crises are significantly rarer (74); the propensity for sickling of different red cells is not correlated to their density (73); etc. While the rate of polymerization in individual cells was found to scale with the concentration of HbS in them (75), several studies showed that the clinical manifestations of sickle cell anemia are dramatically different in patients with identical concentrations of HbS in their red blood cells (63,76-78).

With these contradictions, it was suggested that the HbS polymerization is just one of many events in the sickle cell anemia pathophysiology, and that other factors, such as adhesion of the outsides of the red cell membranes, adhesion of the endothelial walls (79), flexibility and permeability of the red cell membrane, and others, may be equally or more important for the onset and frequency of sickle cell crises.

Besides transfusions with normal blood (free of HbS), two other main treatments for sickle cell anemia are currently applied in the clinic: bone marrow transplantation and

hydroxyurea. Clearly, the former is a difficult and risky procedure, and few cases are treated in this way. The beneficial effects of hydroxyurea are limited to less than half of all sickle cell patients (63). Thus, fundamental studies of novel potential treatment pathways are still underway. These studies are focused on red cell adhesion, endothelial activation, platelet activation, membrane damage and many other factors (73,80-82). In view of the failures of the polymerization scenario, discussed above, it is perhaps understandable why the current clinical treatment strategies do not include attempts to directly inhibit hemoglobin polymerization (83).

There is a potent recent finding, which suggests that delaying polymerization may still be a practical venue in the search for clinical therapies. Transgenic mice expressing human HbS were employed (4). Their HbS was genetically modified: valine at the β6 position was left intact, but the residues, with which it forms hydrophobic contacts in the fiber, were modified. In this way, the sickle cell gene was not touched, and its suspected pleiotropic consequences would not be affected. It was found that the additional mutations inhibit incorporation of the modified HbS into the polymer. The modification was found to delay polymerization, strongly reduce the fraction of sickled red blood cells, and reduce the severity of sickle crises. Significantly, two features of the disease, red cell dehydration and the count of irreversibly sickled cells, sometimes considered as independent factors for the disease, were also reduced (4). These results provide a cure for sickle cell anemia, at least in mice, other than bone marrow transplantation. The remarkable fact is that the cure works through delay of HbS polymerization. This delay was achieved through a genetic modification of hemoglobin, and it is likely that such

gene therapy in humans will be delayed by many years. Hence, other means to delay polymerization should be sought.

The finding that delaying HbS polymerization leads to sickle cell anemia cure is in apparent contradiction with the slate of facts about the disease which defy the primary role of polymerization. Some contradictions can be resolved within the framework of the current knowledge on HbS polymerization: the increased adhesion and other modifications of membrane properties of sickle red cells may be due to the repeated cycles of sickling and deformation that such cells undergo (84). Since venules are the blood vessels of highest shear rates of the blood flow, it is likely that this is the explanation of the increased propensity of sickling in the venules (85): shear is transferred into the cells utilizing the tank-threading mechanism (86,87) and high shear rate is known to increase the rate of HbS polymerization (88,89). Clearly, endothelial activation must be a factor independent of red cell sickling, which likely increases the severity of the disease (80). However, the disease variability in patients with identical expression of HbS (78), in particular the increasing evidence, sometimes anecdotal, of individuals with sickle cell genotype, who never experience sickle cell symptoms (90), and uncorrelated cell density and sickling propensity cannot be rationalized in this way.

2.3.2. Characterization of kinetics of HbS polymerization: current state of the art and interpretation of data

For quantitative understanding of nucleation and growth, data on the two processes need to be collected independently of one another. The kinetics of polymerization has been studied by many groups, the earliest evidence being the study by

Ferrone *et al* (57). The two most important criteria for characterizing the polymerization kinetics are: nucleation rate (J) and delay time (θ). A good way to accomplish this is by direct monitoring of a supersaturated solution of HbS. Our group used this procedure to collect the kinetic data and the procedure for fast creation of supersaturated deoxy-HbS solution is by the **photolysis of CO-HbS by a laser**, as done with bulk samples before (57,58).

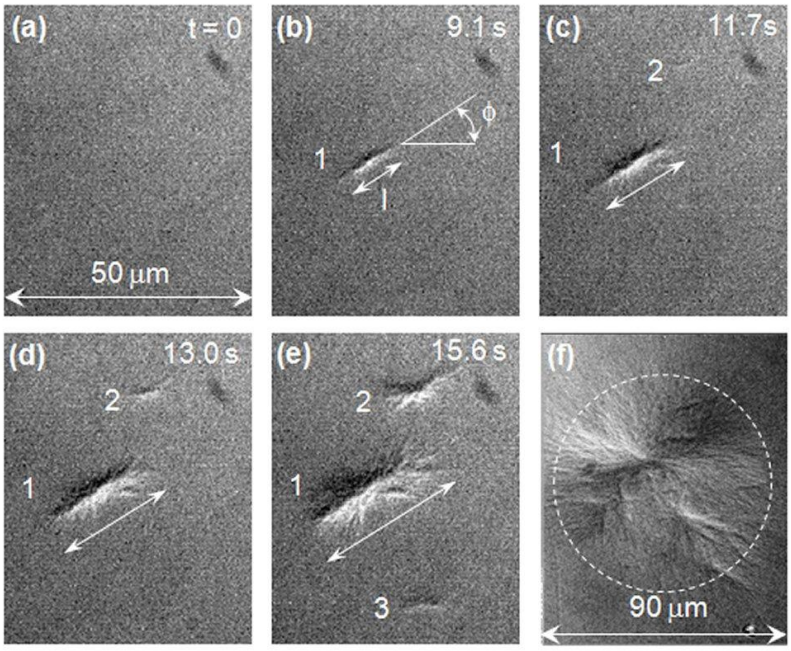

Figure 2.13. Evolution of HbS polymerization monitored by differential interference contrast microscopy in a 25 μm thick slide of supersaturated HbS solution. (93, 94)

If the solution is held in thin slide, individual fibers as short as 0.5–1 mm can be detected by differential interference contrast microscopy (DIC) (91,92). A typical sequence of images of the evolution of HbS polymerization is shown in Figure 2.13, where the determinations of the fiber length, fiber orientation, and the time of appearance of individual fibers is also illustrated. Times for (a) – (e) are indicated on panels, image in (f) corresponds to equilibrium between polymers and solution reached after ~ 1 min of polymerization. Elongated spherulites in (b) – (e) evolve into isometric spherulites in (f).

Width of panels (a) – (e) is shown in (a). Determinations of fiber length *L* and orientation angle *f* are illustrated in (b). Individual spherulites traced through (b) – (e) are labeled with numbers. The numbers of spherulites appearing at certain conditions for a certain time *t* after supersaturation was imposed were averaged. From the dependence of the mean number $\bar{N}$ of spherulites for each *t*, our group determined the nucleation rate *J* and the nucleation delay time θ, as discussed in detail in Refs.(93,94). The delay time θ, defined from the dependencies of the number of nuclei on elapsed time after supersaturation is imposed, is a characteristic of the homogeneous nucleation only and is unaffected by the kinetics of growth and branching. This delay time is modeled by nucleation theories and data on it allow critical test of these theories and the models that they represent.

Figures 2.14(a) and (b) show the dependencies of the nucleation rate *J* and the nucleation delay time θ of the polymers on temperature at three different HbS concentrations. Data from our group suggested that homogeneous nucleation rate is an exponential function of temperature which also indicated the confirmation of there is no heterogeneous substrate present when the nucleation is initiated. The in vitro experimental nucleation rate (J) is found to be of the order of 10^9 $cm^{-3}s^{-1}$ which characterizes the fast growth of HbS in vivo. The faster rate may be representative of dense liquid phase present in the solution within which the concentration is higher than the homogeneous solution and within which the nucleation takes place (95). The unusual faster exponential rate (than linear kinetics of usual protein aggregations) dependence on concentration can be proof of either lower, one dimensional translational symmetry of HbS polymers which may lead to lower barrier for the second stage; or the second order

parameter of polymerization, high density fluctuations within mesoscopic dense phase, may have exponentially faster kinetics of probing the exact fit structures to form (94).

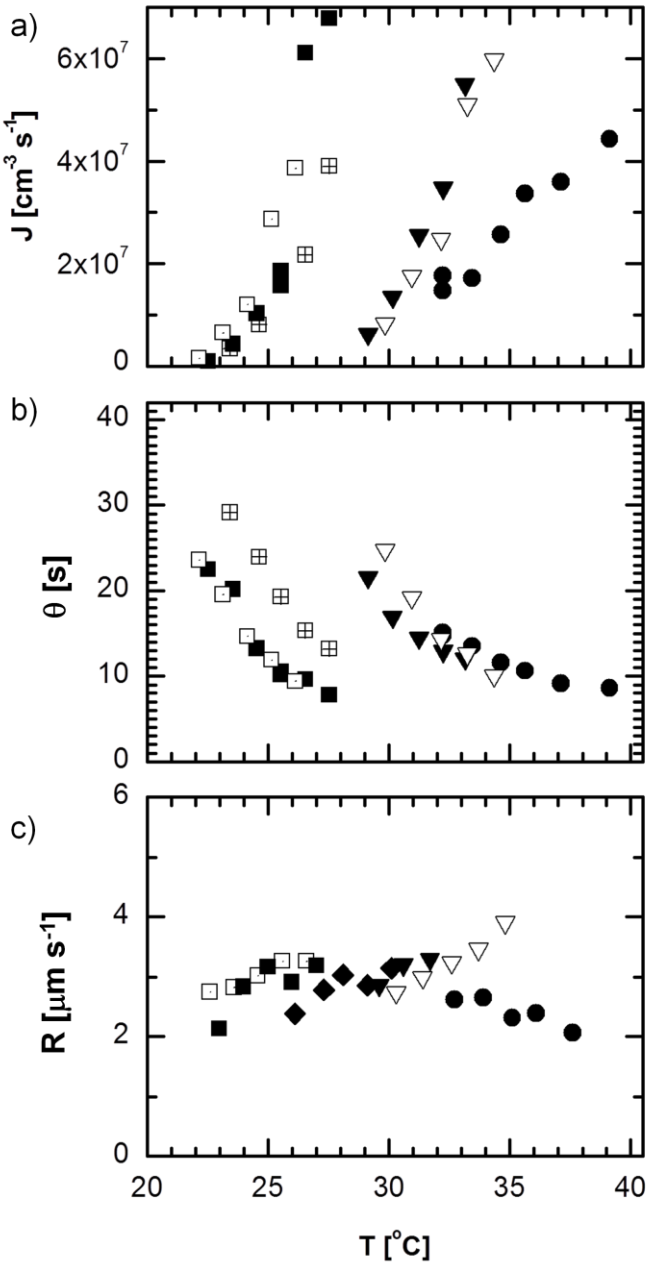

Figure 2.14. Kinetics of nucleation and growth of the HbS polymers. Circles C_{HbS} = 201 mg ml^{-1}; inverted triangles C_{HbS} = 210 mg ml^{-1}; squares C_{HbS} = 230 mg ml^{-1}. Different symbols correspond to different experiment series. (a) Nucleation rate J. (b) Nucleation delay time θ. (c) Rate of growth HbS polymer fibers R.

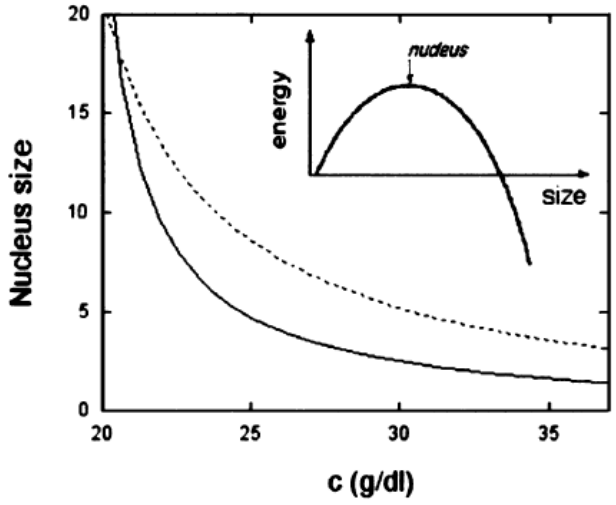

Figure 2.15. Dependence of nucleus size of heterogeneous nucleation (solid line) and homogeneous nucleation (dashed line) and energy barrier for nucleation.

The homogeneous nucleus size (n^*), that is the principle rate limiting characteristics of the process, was found to be 11.4≈11 or 12 at 25°C and 232 $mgml^{-1}$. According to classical nucleation theorem (96), the nucleus size depends on the supersaturation and previous studies based on reaction order estimate did not give conclusive result about the nucleus size. The double nucleation theory predicted it to be 7 which was experimentally validated (94) for lower supersaturation.

2.3.3. Growth of fibers and transition state entropy

In contrast to nucleation rates, the average fiber growth rates only weakly depend on temperature. The individual growth rates vary by up to 40 % under identical conditions. These variations are attributed to instability of the coupled kinetics and diffusion towards the growing end of a fiber. It was shown that due to this coupling, the

average growth rate of the HbS fibers is reduced, in comparison to the case of infinitely fast supply of material, by a factor $k \approx 3$ (93).

The fiber growth rates R in figure 2.14(c) are 2-4 mm s^{-1}, i.e., if similar rates are found in the red cells of sickle cell patients, the fibers would reach the cell walls and stretch the cells within 2-3 s. These rates are faster by at least factor of 10× than the fastest rate recorded for the growth of any protein ordered structure (97). Analyses of the dependencies of the fiber growth rates on HbS concentration and temperature revealed that the incorporation of the HbS molecules from the solution into the polymer fibers follows a first order kinetics described by a Kramers-type kinetic law. The enthalpic penalty is due to the van der waals interaction and hydrogen bonding inside the hydration layer around the polymer which is quite typical for the protein molecules the value being in the order of ~30 $kJmol^{-1}$. The calculation estimated the value here to be 28 $kJmol^{-1}$ which is of the same order as those in the literature. The entropic contributions come from two processes: (i) loss of entropy due to loss of rotational and translational degrees of freedom of the molecule which is joining the fiber and (ii) loss or gain in entropy due changes in the hydration layer around the fiber or around the HbS molecules present in the solution. The total entropy is found to be 95 $Jmol^{-1}K^{-1}$ which basically comes from the contribution of the hydration layer change around molecules in the solution as the gap between the fibers are too small to accommodate sufficient number of water molecules to compensate for the total entropy change (98).

The positive sign of $\Delta S^{\neq}$ is remarkable: it indicates that the entropy contribution to the free energy barrier $\Delta G^{\neq}$ for incorporation lowers this barrier and accelerates the growth of the polymer. The value of $\Delta S^{\neq}$ likely indicates an overwhelming contribution

from the gain of degrees of freedom of the water molecules, which are associated to the HbS molecules in the solution and are set free upon the formation of the transition state. Such gain is expected for the hydrophobic contacts which form between the valine at the β6 site and the alanine, phenylalanine, and leucine from the adjacent HbS molecules (47,49,99,100). The sign of $\Delta S^{\neq}$ agrees with an estimate from molecular dynamics simulations of the free energy of the hydrophobic interaction between two flat sheets of 60 carbon atoms each, approaching each other in water (101-103). However, the magnitude of $\Delta S^{\neq}$ for HbS polymerization is greater than the value resulting from the simulations, ~ 25 J mol^{-1} K^{-1} per carbon atom, indicating stronger structuring of the water around the HbS residues involved in the contacts in the HbS polymer than around bare carbon atoms. From the values of $\Delta H^{\neq}$ and $\Delta S^{\neq}$, $\Delta G^{\neq}$ is negligible, i.e., the entropy and enthalpy contributions to the incorporation barrier cancel out and incorporation is effectively barrier-free and accounts for the very fast growth of fibers.

It is tempting to suggest that if $\Delta S^{\neq}$ could be lowered, this could slow down the rate of fiber growth. Indeed, bringing down $\Delta S^{\neq}$ to 50 J $mol^{-1}K^{-1}$ would slow down the rate of fiber growth by a factor of ~5000×, from a few mm s^{-1} to a few mm $hour^{-1}$. The consequences for the disease pathophysiology would be that even if HbS polymers nucleate in the erythrocyte cytosol, the fibers would not grow to a size comparable to that of the cell, ~ 7 micrometers, for the ~ 15 s that red blood cells spend in the venous circulation. Growth regulation via rearrangement of water structures has been accomplished for two systems, insulin and calcite (104,105).

2.3.4. Two step mechanism of polymerization

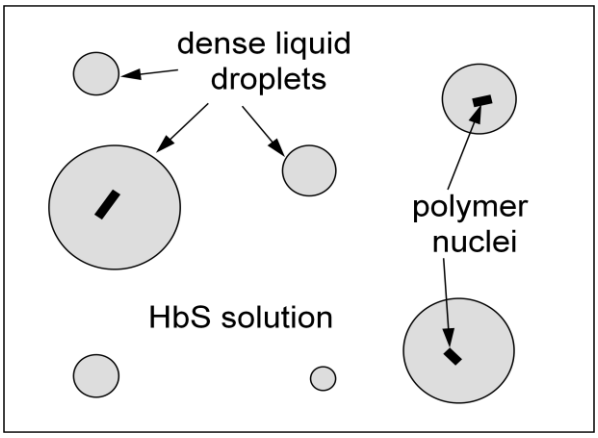

Figure 2.16. Schematic illustration of the two-step mechanism of nucleation of HbS polymer fibers. Step 1 is the formation of dense liquid droplets. Step 2 is the formation of fiber nuclei within these droplets.

The quantification of the kinetics of nucleation of individual fibers from image sequences such as the one in figure 2.13, in terms of nucleation rate, i.e., number of nuclei appearing per unit volume per unit time, and nucleation delay time, i.e., the time during which the probability of having even one nucleus is zero, is discussed in Refs. (93,94,106). In combination with the data on the growth rate, discussed above, the data on the nucleation rate and delay times at different HbS concentrations and temperatures provide insight on the mechanism of homogeneous nucleation of HbS fibers. In studies to-date, it has been implicitly or explicitly assumed that this nucleation is a one-step process: the disordered HbS molecules from the solution assemble into an ordered nucleus which has the same structure as long HbS fibers. An alternative mechanism was suggested by recent results on another first-order phase transition with proteins: formation of crystals. Both experiment and theory revealed that, for protein crystallization, the formation of dense liquid droplets may precede and facilitate the formation of ordered nuclei as illustrated in figure 2.16 (107-112). The dense liquid may

in some cases be stable with respect to the dilute solution (113,114), or, in other cases, it may be metastable (110,115,116). Comparing Figure 2.16 with Figure 2.12, the dense liquid droplets would be placed in the schematic in figure 2.12 between the single molecules and the polymer nuclei.

After the first data obtained with protein solutions, the applicability of the two-step mechanism has been demonstrated for crystallization in a variety of systems: colloid materials (117), non-polar (118,119) and ionic (120,121) small-molecule compounds, and even for formation of another ordered solid phase of proteins, amyloid fibrils (122).

Our group has demonstrated that the two-step mechanism applies to the nucleation of sickle cell hemoglobin fibers (50,93,106). It was shown that *stable* dense liquid HbS phase does not exist in the HbS solutions in which the nucleation kinetics was studied (95). However, dynamic light scattering monitoring of these solutions revealed *metastable* dense liquid clusters in these solutions (50). The metastable clusters are similar to those seen with the proteins lumazine synthase (123,124) and lysozyme (125). In deoxy-HbS solutions, the clusters are present immediately after solution preparation and overall their radius is relatively steady. They exist in broad temperature and Hb concentration ranges. The correlation function reveals two processes: the one with characteristic time of ~ 0.04 ms is the Brownian motion of single HbS molecules and it is present at all solution concentrations. A second process has a longer characteristic time and its amplitude increases with higher hemoglobin concentrations. It was shown that this slower time corresponds to HbS clusters suspended in the HbS solution, and not to single HbS molecules embedded in a loose network structure constraining their free diffusion. The clusters have macroscopic lifetimes and occupy $f = 10^{-4} - 10^{-2}$ of the

solution volume (50). The dense liquid spinodal, observed in a series of studies (126,127) is likely a characteristic of these clusters. Such "hidden" spinodals have been defined and observed in other systems (128,129).

The two-step mechanism of homogeneous nucleation of HbS polymers treats the first step of the overall mechanism of HbS polymerization, illustrated in figure 2.12 and modeled by the double-nucleation mechanism (46,57,58). No contradictions between the two models exist and the two-step nucleation mechanism of nucleation of HbS polymers suggests that the presence of a disordered precursor may be a general feature of the self-assembly of ordered structures in new class of solution systems.

2.4. Molecular interactions in HbS fibers and free heme perspective

Jones *et al* (130) concluded that the fibers of sickle cell hemoglobin polymers are strongly bound to each other. Though both circular cylinder model and helical model of HbS fibers indicated higher than the experimental value, it reflected the necessity of restating the depletion interaction for unknown characteristics of the protein fibers (130). Heme is excessively released in sickle erythrocytes due to autooxidation of hemoglobin to met-hemoglobin, which has lower stability (6). If the iron ions, which are in their Fe^{2+} form in heme, are oxidized to Fe^{3+}, the compound is called hemin; thus, it is likely that the heme released from met-Hb is in the form of hemin. While the form of iron in the intra-erythrocytic free heme has not been determined, in view of the lack of reducing stress in the red cell cytosol, it is unlikely that the released hemin is reduced. The stability of HbS to auto-oxidation is lower than that of HbA (this lower stability has been pointed out as another consequence, significant for the pathophysiology of the sickle cell

anemia, of the sickle-cell mutation (72)) and hence the amount of free heme in the red cells of sickle cell patients may be higher than in healthy adults (6).

The free heme has been implicated in damage of the red cell membrane, leading to higher red cell adhesion to the endothelium (80). Existing evidence suggests that higher frequency and severity of sickle cell crises in patients with equal expression of HbS, such as monozygotic twins, may be related to enhanced release of heme, exhibited as membrane-bound iron (77). While in Ref. (77) the deleterious effects of heme released form HbS were assigned to damage to the erythrocyte membrane, it is possible that the increased severity may be due to other consequences of the increased concentration of free heme in the cytosol.

The preliminary results (5) show that free heme at concentrations of order 100 μM enhances the polymerization of sickle cell hemoglobin by orders of magnitude, and that its removal prevents polymerization. The lack of polymerization after removal of the released heme is not due to conversion of HbS to apo-Hb: less than 4% of the HbS in the solutions loses its heme, see determinations below, and such decrease in HbS concentration leads at best to a weak polymerization slowdown. With regard to the unexplained clinical features of sickle anemia, discussed above, potential findings on the role of heme in the polymerization of HbS may provide new avenues, through which polymerization may be controlled and delayed, and new therapeutic strategies may operate.

2.4.1. Free heme determination

The absorption of light by heme and its derivatives in aqueous solutions has not been extensively studied: the existing measurements are mostly in organic solvents or, if in aqueous solutions, encapsulated in detergent micelles (131). Since light absorption by heme, both when part of hemoglobin and when free in solution, strongly depends on the kind of solvent, we took to characterize it. The heme spectra in figure 2.17 are similar to those of met-Hb and indicate that the heme iron is in Fe^{3+} form and heme is in the form of hemin, even in the presence of dithionite. From the data in figure 2.18, he extinction coefficient of heme at λ = 630 nm, in the region where deoxy- and oxy-Hb absorb less than 0.01 of the incident light, is ε = 5.89 mM^{-1} cm^{-1}; in solutions saturated with O_2 (spectra not shown) this coefficient is 6.07 mM^{-1} cm^{-1}.

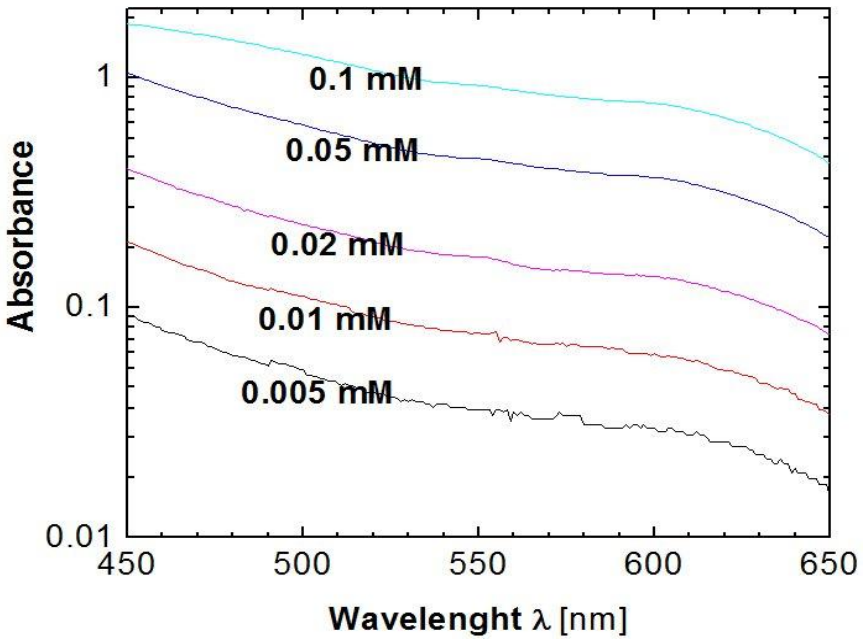

Figure 2.17. Spectra of heme at five heme concentrations in solution saturated with CO in the presence of 50 mM sodium dithionite. (5)

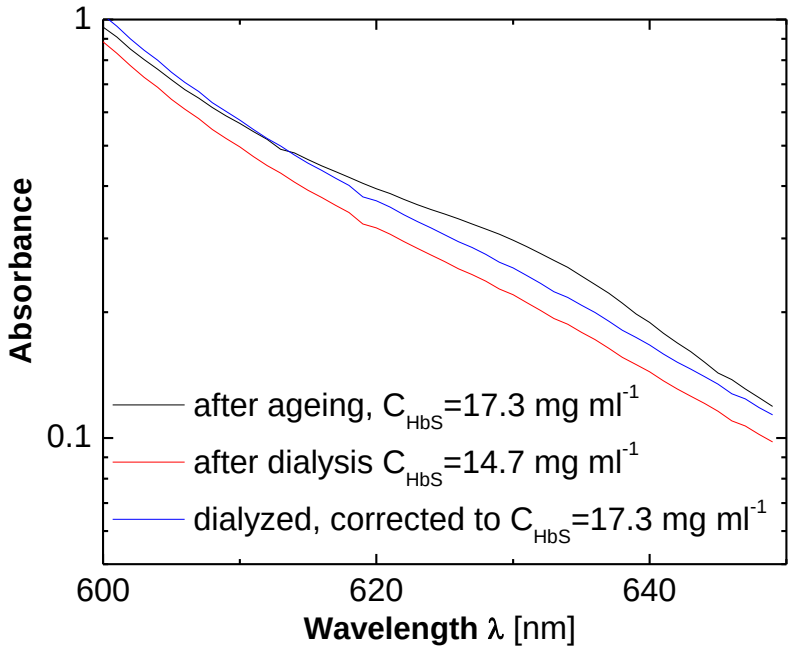

Figure 2.18. Spectra of HbS aged at T=25°C in oxygenated phosphate, buffer before and after dialysis [5]. Both samples were saturated with CO; 50 mM dithionite was added.

Free heme has similar spectrum to met-hemoglobin and not all met-HbS releases its heme. Hence, the determination of the concentration of heme in the presence of HbS requires separation of the two species. We dialyzed a HbS solution sample aged overnight at 25^{o}C and representative of the solution in figure 2.19(c) through a membrane with a molecular mass M_w cutoff 2000 g mol^{-1}; heme with M_w = 617 g mol^{-1} dialyzes out. Heme concentration was determined from the difference of absorbance at 630 nm before and after dialysis, figures 2.17 and 2.18. With the above ε, this determination yields the concentration of free heme in the solution is 0.007 mM = 26 mole HbS/mole heme. Thus, in a 200 mg ml^{-1} = 3.1 mM solution of HbS, free heme concentration of 80 μM is expected. Extended dialysis did not increase this result. Re-ageing of dialyzed sample over another 20 h at room temperature produced similar heme amounts.

2.4.2. The role of the heme in HbS polymerization

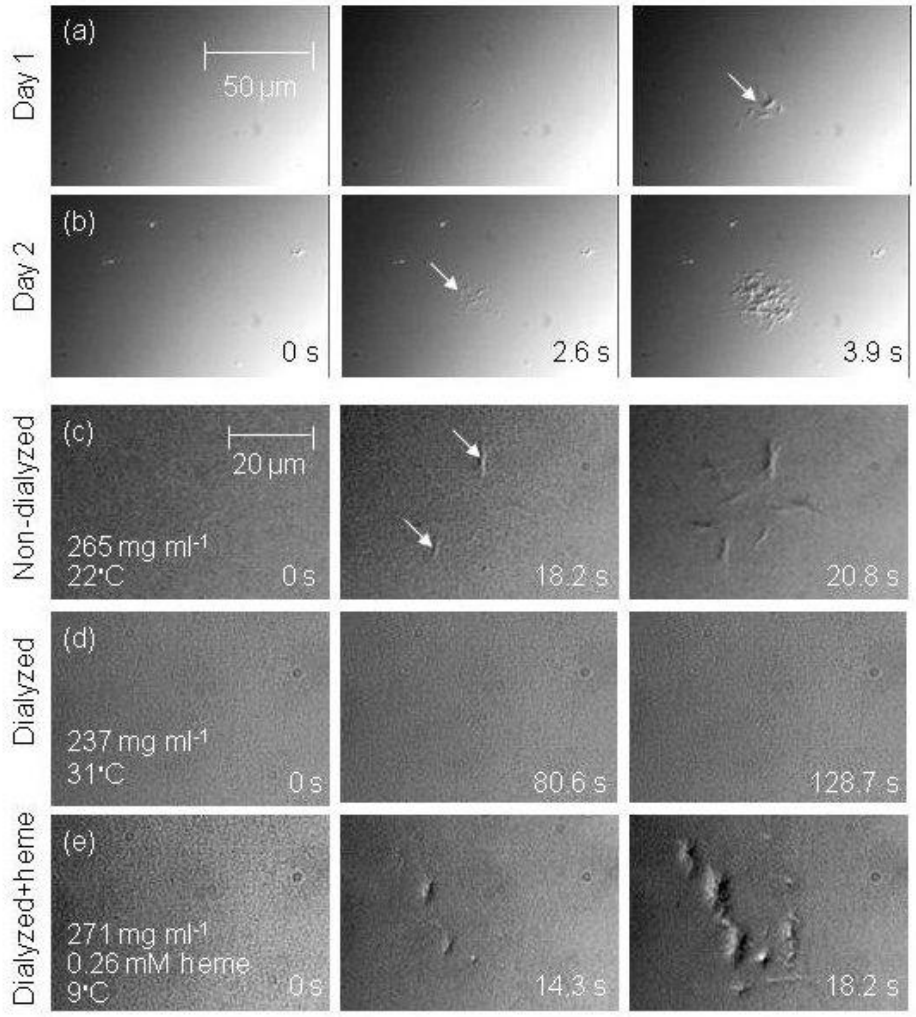

Figure 2.19. Effects of aging and heme on the polymerization of sickle cell hemoglobin. (5)

Most recently our group (5) showed that complete removal of free heme arrests polymerization and also it was tested whether increasing free heme concentration increase the polymerization rate and it was found to be positive. The dialyzed solution free of heme did not show any evidence of polymerization during longer period of time and the non-dialyzed and solution with added heme showed evidence of polymerization. It can also be seen from the figure above that upon ageing of HbS solution has higher rate

of polymerization. Characterization of the aged HbS solution by mass spectroscopy reveals that no unexpected species, e.g., pieces of protein chains, appear in the solution upon ageing, and that heme is the only solution component, which appears to increase its concentration (mass spectroscopy cannot be used for quantification of the detected species). Fe^{3+}, while not seen in the mass spectra, has solubility in the attomolar range at the solution pH. In the dialyzed solution (for removing free heme), no polymers form, even at temperatures as high as 36.5^{o}C (higher concentrations and temperatures lead to faster polymerization); an illustrative example is shown in figure 2.19(e). In figure 2.19 solution of CO-HbS is held in slides of uniform 5 mm thickness. The panels in each row represent the evolution of polymerization under a set of conditions. Time after start of photolysis is indicated in each panel. HbS concentration and temperature for each row are indicated in left panel. (a)-(b) have same concentration and temperature. Scales for (a)-(b) and (c)-(e) are different. White arrows point at HbS polymer domains.

In figure 2.19, (a)-(b) show evolution of polymerization in solution prepared from one-month old stock stored under liquid nitrogen: solution used in (a) was freshly prepared solution and in (b) was prepared from stock stored at room temperature for one day. (c)-(e) show the effect of heme on HbS polymerization: (c) HbS polymerization in a solution prepared from one-week old stock; (d) removal of small molecules by dialysis with molecular weight cut-off 2000 g mol^{-1} prevents polymerization even at higher temperature; (e) heme at shown concentration was added, temperature was lowered to suppress polymerization. Eight combinations of HbS concentration and temperature were tested at which polymers appear within a few seconds in normally prepared HbS solutions, but did not appear after dialysis. The addition of 0.26 mM of heme to the

dialyzed solution led to nucleation and growth rates significantly faster than before dialysis, figure 2.19(f).

Quantification of the kinetics of nucleation and growth shows that (i) The rates of nucleation and growth in solutions prepared from one-week old stock are lower and the nucleation delay times are longer than in solutions prepared from one-month old stock in Refs. (93,94,106). As in figure 2.19, we conclude that the faster rates after longer storage are due to release of heme, likely during thawing and re-freezing. (ii) After dialysis, no HbS polymers nucleate, i.e., $J = 0$, $\theta = \infty$, and R is undefined (for definition of symbols, see figure 2.14). (iii) The addition of 160 or 260 μM of heme to dialyzed solutions enhances J and R by more than two orders of magnitude and shortens θ by approximately the same factor in comparison with the rates and times prior to heme removal. Since according to the above determinations, in the undialyzed solutions heme concentration is ~ 80 μM, this acceleration is consistent with higher polymerization rates at higher heme concentrations.

These observations show that free heme accelerates HbS polymerization; in the absence of heme, polymerization is prevented under the conditions tested here and, likely, is significantly delayed in a broader range of conditions. The low concentration of heme, 160 or 260 μM, required for significant effect on nucleation and growth, would be released if, e.g., < 2 % of HbS molecules, whose concentration is ~ 4 mM, lose their four hemes. From static light scattering data, our group also demonstrated that heme interacts with hemoglobin molecules through electrostatic repulsion causing them to fell apart from each other and then attract due to van der waals interaction, and as one heme

molecule can interact with number of hemoglobin molecule, this contributes to the high rate of polymerization in presence of heme.

The existing therapeutic strategies (as well as some of the failed ones) have been based on lowering the concentration of sickle cell hemoglobin: by increasing the expression of fetal hemoglobin via hydroxyurea; by binding of so-called anti-sicklers to hemoglobin; or by bone marrow transplant. If the role of the heme is demonstrated, then an alternative therapy pathway could be the removal of the free heme from the red cell cytosol via binding agents, or decreasing its release by introducing anti-oxidative drugs.

For investigating the effect of small concentration molecules like heme on HbS polymerization kinetics it is necessary to have a robust and reliable experimental setup for nucleation experiments. For this reason we intend to employ a microfluidic platform to study the polymerization of sickle cell hemoglobin. The fabrication and management of this device is what we are going to discuss in the following chapters.

CHAPTER 3

MICROFLUIDIC DEVICE DESIGN & MICROCHANNEL FABRICATION

The present work focuses on the design of new experimental setup for observation of automation of studying HbS polymerization kinetics. Determination of nucleation rate of sickle cell hemoglobin (HbS) polymers from supersaturated HbS solution, HbS fiber growth rate and knowing effects of different solution components and physiological parameters on these rates require a large amount of statistics from nucleation experiments to be processed. For this purpose, we intend to implement two recent advances in the experimental technology: microfluidics and thin film heaters. Microfluidics allow manipulation and observation of small solution volumes, while thin film heaters allow localized fast temperature ramps, inaccessible to the classical tools of temperature control. The greatest advantage of the proposed setup is its simplicity of use. The proposed setup will allow data to be collected from kinetics observations within array of droplets managed in microfluidic device which is necessary for the improvement in the statistics of the experiments and also this will enable faster manipulation of different experimental conditions and observation of effects of different small concentration additives.

The conventional procedure for HbS polymerization kinetics data is the use of laser photolysis of carbomonoxy sickle hemoglobin (CO-HbS) which was first introduced in the 1980s (46). In this method, the solution sample of CO-HbS is heated by laser and the supersaturation is achieved within fractions of second. The red blood cells spend about 15s in the venous circulation for which the investigation at very small time scale is

required. Though the photolysis procedure was much faster than the classical ones (57,58) which had time scales on the order of minutes, the rate limiting step for this procedure was the diffusion of the released CO. The diffusion requires at least 1 second which limits the time scale for measurement. Also the overheating of the solution and diffusion of CO lead to non-uniformities in the temperature and concentrations of HbS solution (93). These non-uniformities impose limitations on the external parameters, which could be experimentally probed: HbS concentration, temperature, degree of oxygenation, additive type and concentration, etc. These limitations lead us to think about the microfluidics manipulation of the solution so that assay for such parameters can be tested easily.

The modification of environment into micro space and volume representing similar physical, chemical and kinetic behavior of the system is the very basic of microfluidic manipulation of any kind. The necessity arising from low volume generation by various systems & their low detection level and the requirement of handling as less of the reagents as possible for experimental works are the very bases of microfluidic devices fabrication (132,133). The evolution of MEMS technology also induced the search for ways to manipulate the applicability of such systems within the experimental setups which has enabled the scientific community to come up with means to manipulate systems with low volume characteristics and also to help with the analysis and detection in these systems. The devices which actually play with the volume of fluid of around 10^{-9} to 10^{-18} liters need to be of dimension in micrometer range in one direction. This validates the naming of these devices or systems as microfluidics (132). So the

microfluidics is the science of fluid motion behaving differently from traditional fluid mechanics associated with the small length scale (133).

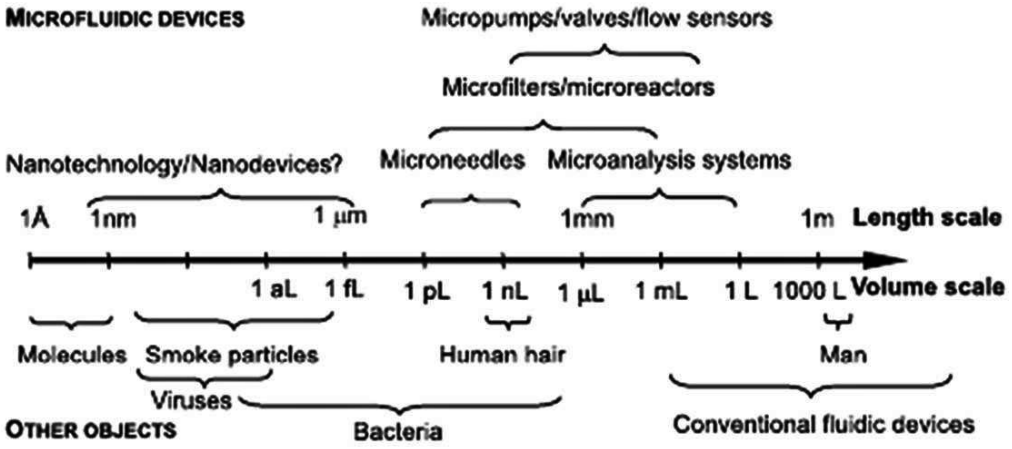

Figure 3.1. Size characteristics of microfluidic devices in use. (132)

The microfluidic system can be viewed as a combination of miniature unit operation modules which are integrated in the same platform to ensure feasible handling and compactness of a process rather using multiple conventional units to process systems to analyze data. The potential of microfluidic devices as high throughput-low cost system for analysis of biological, chemical and physical processes and well established development technology of MEMS have contributed to its rapid development and usage during last two decades (132).

3.1. Design considerations for microfluidic channel and microheater assembly

We developed the principal features of our microfluidic lab-on-chip device based on the requirements for achieving uniform solution concentration and temperature of the sickle cell hemoglobin solution during the polymerization experiment. HbS solution shows retrograde phenomena (46) which means for this temperature regime the solubility

of HbS solution decreases with increasing temperature. This can be seen from figure 3.2. The difference in two data series shown in this figure arises from pH of the solutions.

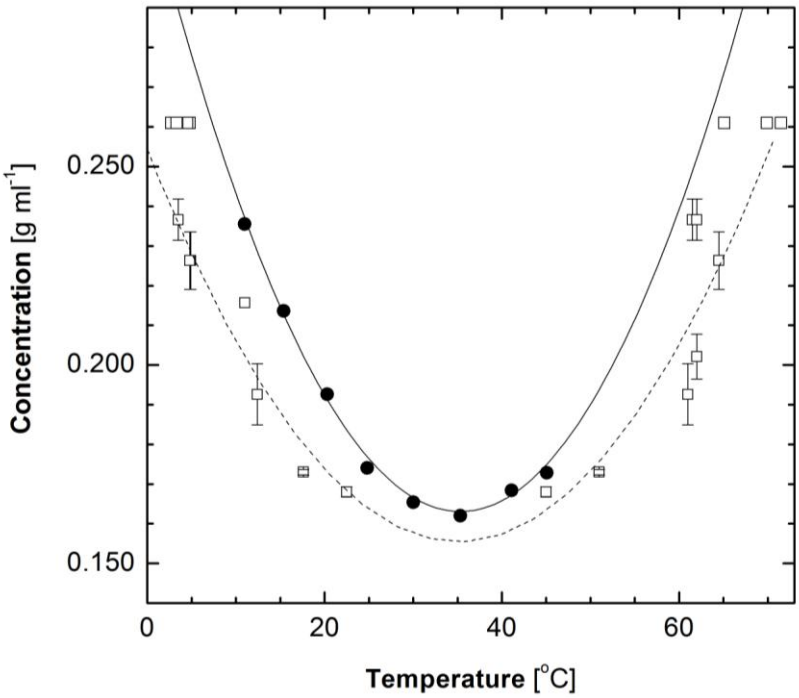

Figure 3.2. The solubility curve of aqueous HbS solution. (•) Black circles (pH=7.15) represent the data from ref (46) and (□) open rectangles (pH=7.35) represent the result obtained by Oleg Galkin in our lab.

We will raise the temperature of 200-250 mg/ml HbS solution droplet within very short period of time (on the order of tens of milliseconds) from 5˚C to 25˚C. Under these conditions, the supersaturation $\sigma=\ln(C/C_e)$ is very high and this leads to polymerization of HbS molecules. We will directly observe the nucleation of polymers using Differential Interference Contrast (DIC) microscopy as in Refs. (93,94).

We aim to achieve faster heating of the solution to simulate and achieve timescale comparable with in vivo polymerization processes. These requirements are very crucial for proper characterization of kinetics of HbS polymerization processes. So our microfluidics device has two significant features: 1) microchannel fabricated from

polymer on a glass substrate for formation of HbS solution droplets and 2) a microheater on the back of another microscope coverslip for localized heating of the HbS solution droplets. We will combine these two pieces of device together to form the sandwich microfluidic chip as shown in figure 3.3.

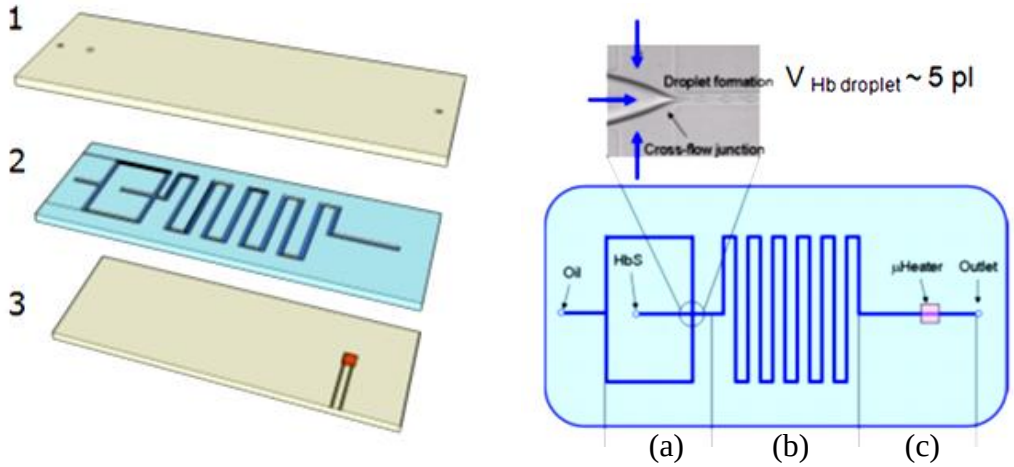

Figure 3.3. The design of microfluidics assembly with flow focusing and localized microheater. 1) 1mm glass substrate with ports to the channels, 2) 5 µm polymer layer with channels and 3) 200 µm thin glass with heater on the bottom. (a) Mixing section, (b) storage section and (c) heating section.

We designed the microfluidic channel for droplet formation on the basis of immiscibility of liquids. Our aim is to form trains of droplets of aqueous HbS solution in silicone oil which will act as the carrier fluid. We want to simulate the in vivo environment of the venules which have diameters between 7-50 µm. We also want to have small volume droplets to ensure uniformity of the solution concentration. For these reasons, we have a design of flow focusing channels where the HbS solutions will be focused by carrier silicone oil and by manipulating the flow rates of these two fluids we will vary the droplet size as per desire. We will use the spiral section of the storage of droplets. The large amount (almost 1000) of droplets are required for the statistics of the

experiment. For fast and controlled heating, we have a circular resistive heater which is aligned with the channel localized at a certain point and will be heating only one droplet at a time. We have designed the heater in such a way that the heat distribution will not affect the droplets waiting near the heating zone. We tested our design with computer simulations for heat transfer in both steady state and transient state.

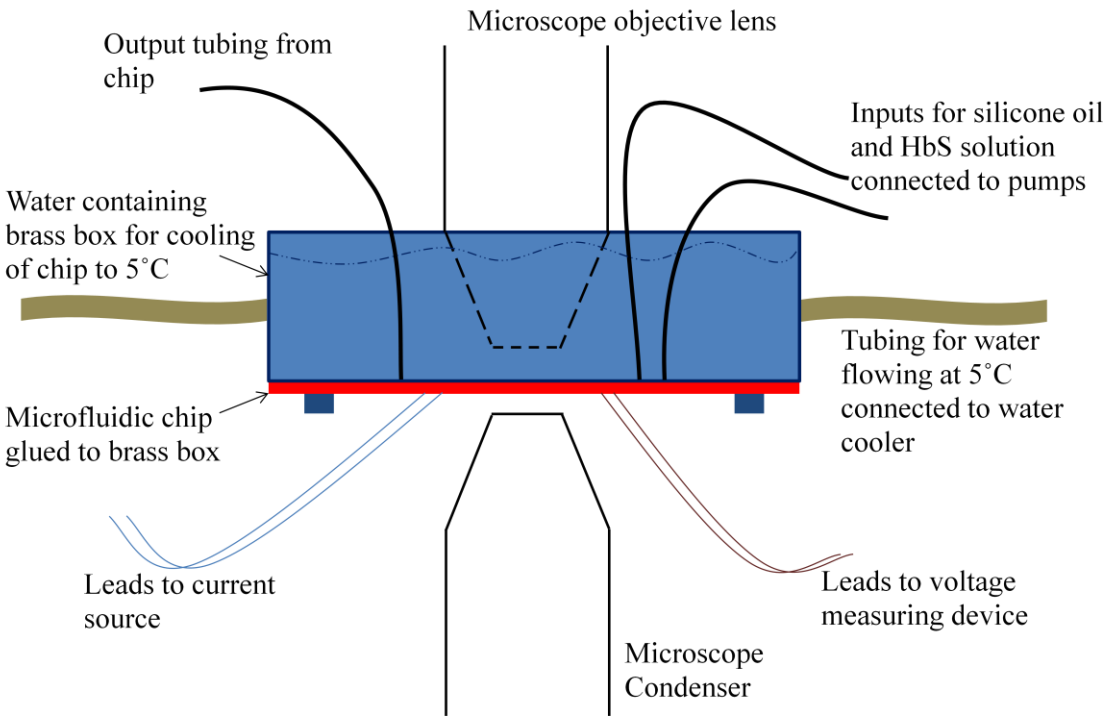

Figure 3.4. Schematic representation of proposed experimental setup.

The temperature will primarily be maintained at 5˚C by a water circulator which will flow cold water to the brass box (as in figure 3.4) attached to the top of the microfluidics chip. The nucleation of polymers will be observed through high speed camera by water immersion DIC microscopy.

Table 3.1. Principal features of microfluidics according to the design considerations.

Feature	**Justification**
Channel height of 5 µm & width of 20-40 µm	i) For comparing with RBC diameter of about 7 µm & to simulate venule diameter of 7-50 µm. ii) To make the volumes of droplets as small as 5pL which is of the same order of the volume of 20 erythrocytes. iii) To enhance faster heat conductance.
Spiral storage section	For storing large amount of droplets to obtain larger statistics of kinetics data.
Channel walls must be air impermeable	To simulate deoxygenated environment.
Two channel inputs	For carrier fluid (Silicone oil) and HbS solution forming droplets using the immiscibility of liquids and their hydrophobic and hydrophilic nature.
The brass box on top of the channel side	To maintain the solution environment (except specific droplet for heating) at 5˚C by water flow.
Microheater having circular dimension of radius 160 µm	i) To obtain fast heating from 5˚C to 25˚C on the order of tens of milliseconds. ii) With small temperature distribution to ensure that the resting droplets are not heated. iii) To attain supersaturation of HbS solution promptly.
Leads connected to heater	To input current and measure voltage to sense temperature.

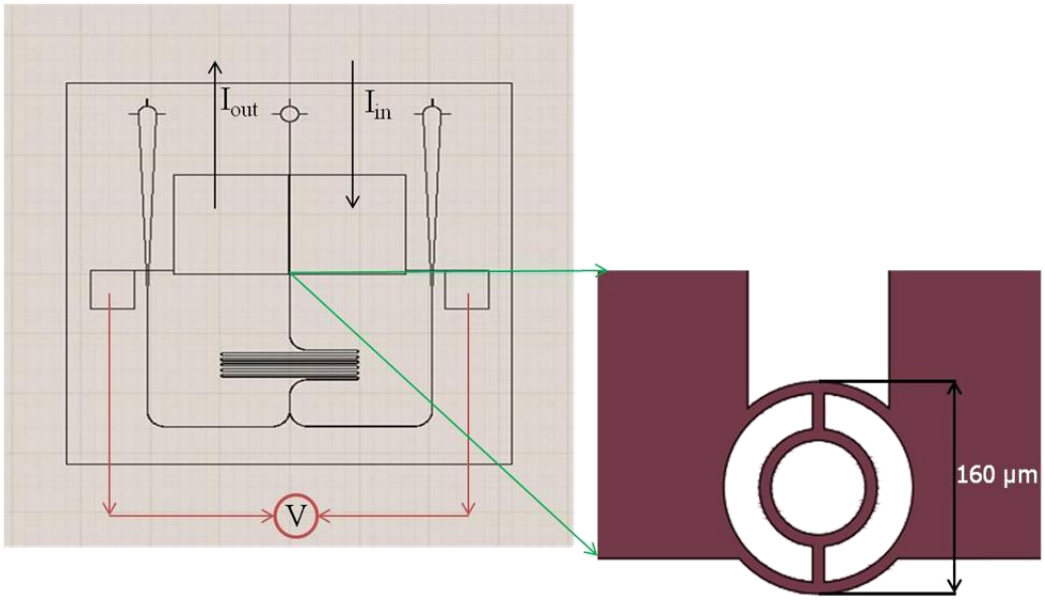

Figure 3.5. Features of preliminary design of microfluidics chip with Y junction for silicone oil and HbS solution mixing and droplet formation. Inset picture shows the heater structure with heat spreading structure.

Though our final design will contain the flow-focusing type microfluidic channel as in figure 3.3, the current design contains the Y configuration of the junction where the two mixing input channels contain the carrier fluid (silicone oil) and HbS solution separately. The primary design of the heater is also shown in figure 3.5.

3.2. Microfluidics channel fabrication

We used conventional photolithography in UH Nanofabrication Facility for the microfluidics channel preparation. At first we looked into the materials which we can use as the final structure material for our channel. The most conventional material used for channel fabrication is polydimethylsiloxane (PDMS). But as we need to deal with deoxygenated HbS solution, we found that oxygen permeability of PDMS (134) hinders

us from using this well-characterized material. So we decided to use another photoresist material SU-8 (135) which is usually used as mould for soft lithography processes.

3.2.1. Photolithography

Photolithography is a process of pattering a design on a photosensitive material through the use of appropriate radiation. The geometry is defined on a mask through which UV-vis light is shone. Photolithography is one of the most used techniques of pattern transfer from design to structure material in MEMS and microfluidics industry. The name is derived from the resemblance of the process with photography (132).

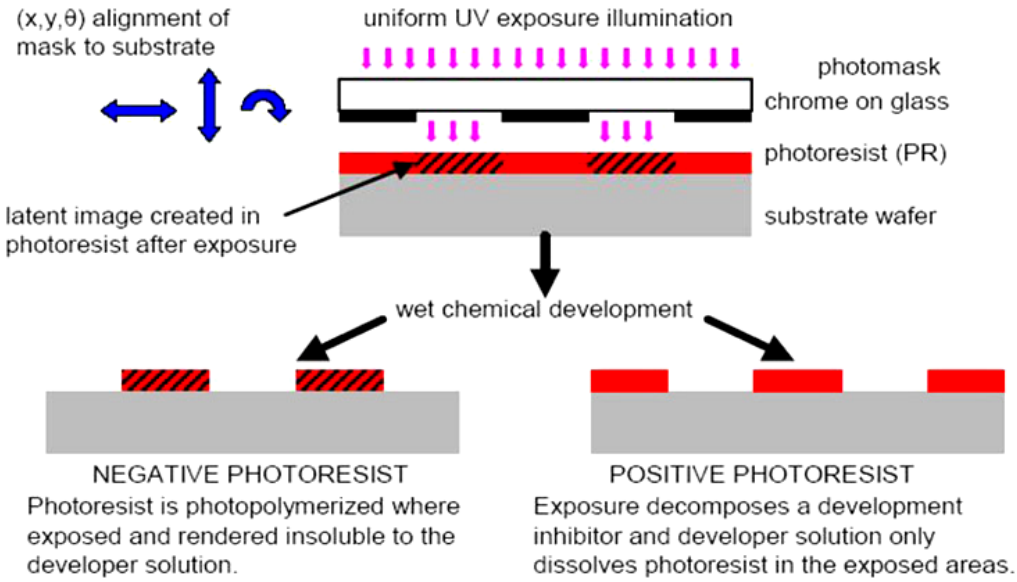

Figure 3.6. Distinction between positive and negative photoresist pattern formation. (136)

The photosensitive polymer material which is exposed to radiation (136) for pattern formation is known as photoresist. Photoresists are basically polymers which upon being exposed to generally UV radiation (from 300 nm to 400 nm) undergo chemical reactions. After reaction they are developed by a developer solution. This process is known as etching. There are two types of photoresists based on the chemical

reaction: positive and negative photoresist. Positive photoresists are those which dissolve in the developer solution after they have been exposed. In negative photoresists exposed portion becomes crosslinked and the unexposed portions dissolve in the developer solution. So the masks used for the photolithographic process are also of two types depending on which photoresist is going to be used. Photolithography, therefore, acts as popular MEMS fabrication process.

3.2.2. SU-8 chemistry and recipe for channel fabrication

SU-8 photoresist (introduced by IBM) (137) is a class of negative photoresists which is widely used (138) for formation of thick microstructures exceeding height of about 1000 microns having aspect ratio structures (139,140) of up to 65:1 (141). This is an epoxy-based photoresist which has low molecular weight component dissolved in a highly concentrated solvent. This makes SU-8 a very good candidate for attaining high aspect ratio structures while having enough mechanical stability. This happens upon UV exposure due to strong crosslinking among the eight epoxy functional groups of Bisphenol A Novolak epoxy oligomer (figure 3.7. (142), named EPON resin (143), within itself and also with neighboring molecules. The photo initiator is triarylsulfonium hexafluoroantimonate salt (139,144), a product of Union Carbide (143), which is used with the resin in 10% of the mass of the resin and then the resultant mixture is dissolved in the organic solvent gamma-butyrolacton (GBL) (145) in high concentration around 70-80%. This produces high viscous liquid whose level of viscosity depend upon the fraction of solvent used for dissolution and depending on the viscosity a broad thickness range for coating of a substrate and thereby a broad high aspect ratio range for microstructures has been obtained.

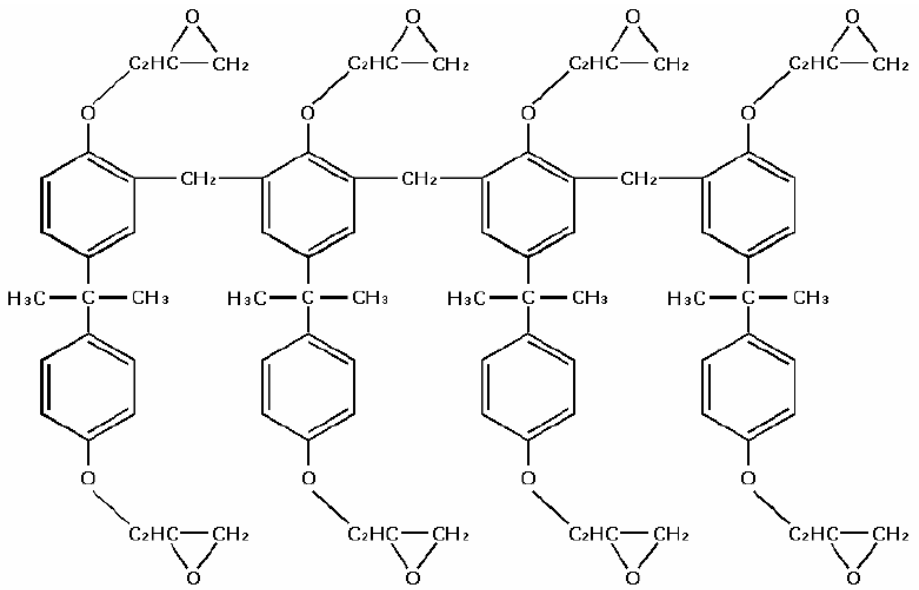

Figure 3.7. SU-8 molecule with 8 epoxy groups on average (142).

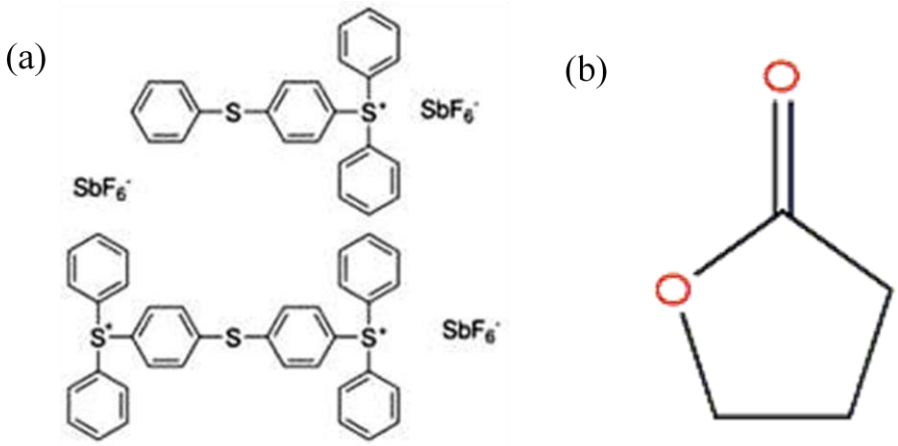

Figure 3.9. (a) Triarylsulfonium hexafluoroantimonate, the photoinitiator in SU-8 resin (144) and (b) gamma-butyrolacton, solvent of SU-8. (145)

SU-8 as structure material has several advantages: (i) it poses good mechanical and chemical strength when fully crosslinked (146), (ii) it can be processed through inexpensive near UV radiation and hence it needs to be exposed in the band width of 365-436 nm (147), (iii) high optical transparency is the key issue for using SU-8 (148) in most

microscopy applications and (iv) most importantly, it is a biocompatible (149) material which suits the objective of our project. Though SU-8 is generally used to produce high aspect ratio microstructures (143) and our objective is to have very thin layer of SU-8, the biocompatibility, impermeability to O_2 (150) and strong mechanical and chemical properties (149) of SU-8 have directed us to choose it as the structural material for our microfluidic device on the soda-lime glass substrate Corning 2978.

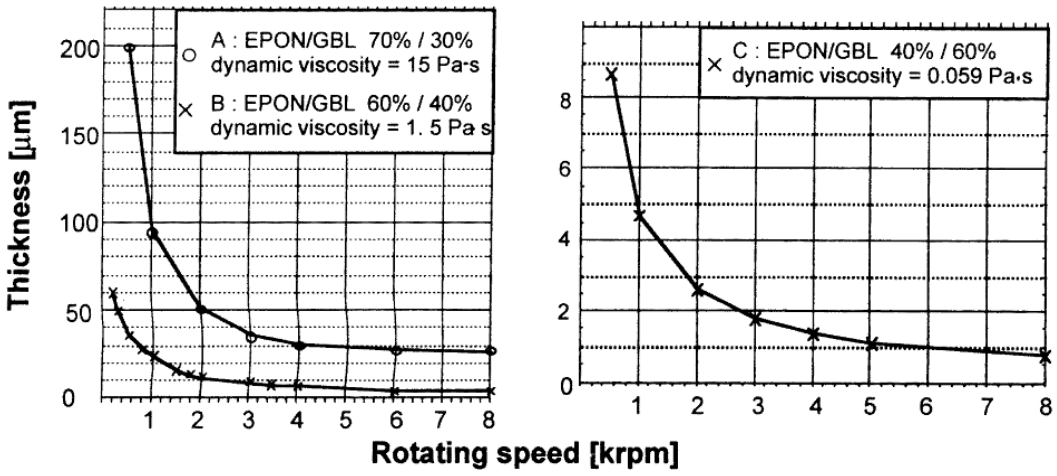

Figure 3.10. Thicknesses of three different blends of SU-8 versus spin speed. (139, 148)

The processing of SU-8 3005 (148) on glass substrate is as follows:

A. Substrate preparation: Substrate preparation is the first crucial step which involves the cleaning of glass substrate. The substrate which is 1 mm microscope slide (Corning 2978) should be free of any kind of particle and also have some intrinsic roughness which will provide good adhesion energy (151) between the substrate and SU-8 layer. Currently we have the following steps of cleaning the substrate:

a) We rinse the substrates in DI water to wash the big particles from the surface.

b) Then we do two-step ultrasonication in 8891 Ultrasonic bath from Cole-Palmer: first in 30% Alcanox soap solution for 25 minutes at 50˚C and later in DI water for another 25 minutes at 50˚C (94).

c) After ultrasonication, we put the substrates into 3:1 H_2SO_4:HNO_3 solution (94) and boil on hot hotplate until the solution is vigorously bubbling. We do this to remove the organic residues from the surface of the substrate.

d) Next we rinse the slides with DI water at least for three times and then store in a container under DI water.

e) When the substrates are required to be prepared for use we take them to UH Nanofabrication facility. We rinse with acetone and DI water just before using.

f) A very crucial parameter for optimizing the adhesion property of SU-8 layer to substrate is dryness of the substrate (152). The moisture present in the substrate may hinder the proper adhesion to occur between the substrate and SU-8 layer. Thus we heat the substrates at 150°C for 10 minutes as per literature (152).

B. Photoresist Coating: We use Brewer Cee 200 spin coater at UH Nanofabrication facility to deposit ~5 μm thin film of SU-8 layer on the glass substrate. The uniformity of SU-8 layer is very important to have good structures on it which can be hindered by high viscosity of photoresist solution. The recipe provided by microchem (148) was not accurate to deal with our substrate. We needed to improve it to the following recipe: a. 500 rpm @ 100 rpm/s (10 sec), b. 3000 rpm @ 300 rpm/s (30 sec).

Figure 3.11. Brewer Cee 200 spin coater in UH nanofabrication facility.

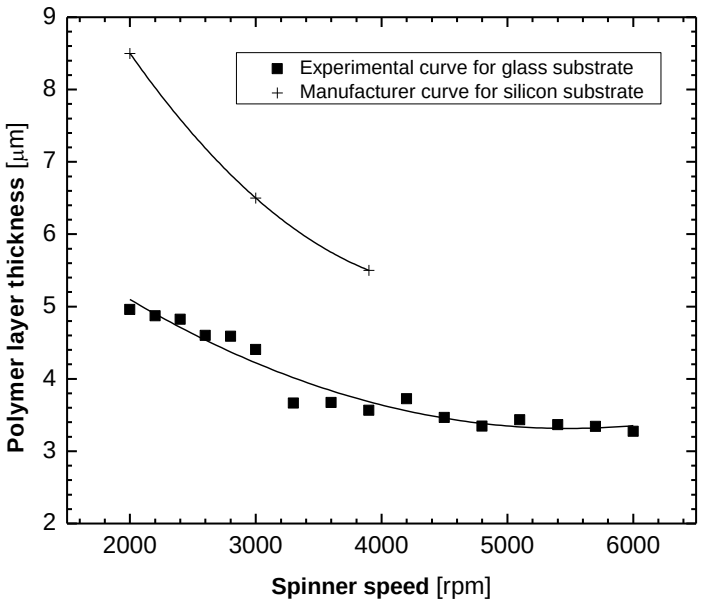

Figure 3.12. Polymer layer thickness vs. spinner speed curve for comparison between manufacturer and experimental data.

We also produced new layer thickness vs. spinner speed curve (figure 3.12) which showed marked difference with the manufacturer supplied recipe (148).

C. Post-coating relaxation: The post-coating relaxation is required for the outgassing of the solvent and low level of surface contraction of the SU-8 layer. It also helps bursting of the bubbles that were formed during the spin coating process (152,153). The solvent evaporation in this step should be controlled through implementation of covering the samples and also low relaxation time which should not exceed 10-15 minutes.

We used a 15 minute relaxation time to ensure primary solvent evaporation. During evaporation we provided a cover for the substrates using a Petri dish.

D. Soft bake: Soft bake is used to densify the SU-8 layer (148) i.e., to remove the solvent from the SU-8 layer. This is a very important step which has important influence in the resolution and structure of the features on the layer (154). Lowering the soft baking temperature (155) from traditional soft baking temperature of 95°C has shown significant impact on lowering the residual stress and avoiding cracking of the layer after development. The diffusion mechanism through the film described in ref (156) also indicates that the fast evaporation of the solvent near surface may induce large concentration gradient in the film which leads to increase in the residual stress in the film. The nonuniformity of concentration of solvent in the layers would lead to compression of the layers during the contact printing under UV mask aligner and this would cause the exposed part to bend and required unexposed part to be exposed leading to non-vertical sidewalls (156). Results have been reported of improved layer uniformity and lower residual stress in case of baking at 60°C for 5-10 minutes for layers below 15μm (157). Soft baking step allows the SU-8 to reflow as T_g of uncrosslinked SU-8 is 55°C and self planarize the layer and for this reason the flatness of the hot plate is desired. There has

been report to cool down with ramping after the second step of soft bake which also provides good solution the problem of cracking due to residual stress (157). Low temperature soft bake (156) may lead to uniform concentration level inside the layer which may later help in the kinetic movement of SU-8 and photoacid molecules in PEB step and enhance the crosslinking in this way (158). Finally we use two step soft bake: 65°C/1min and 95°C/10 min.

E. Pre-exposure Relaxation: Relaxation in between steps of soft bake and exposure is required to outgas the solvent which leads to surface contraction which enhances the flatness of the surface. We are using 4 hour relaxation time after optimizing several intervals ranging from 1 hour to 24 hours.

F. Exposure: Exposure to near UV spectrum of 365-436 nm is the key to initialization of the cross linking on the polymer layer and pattern formation according to the mask prepared.

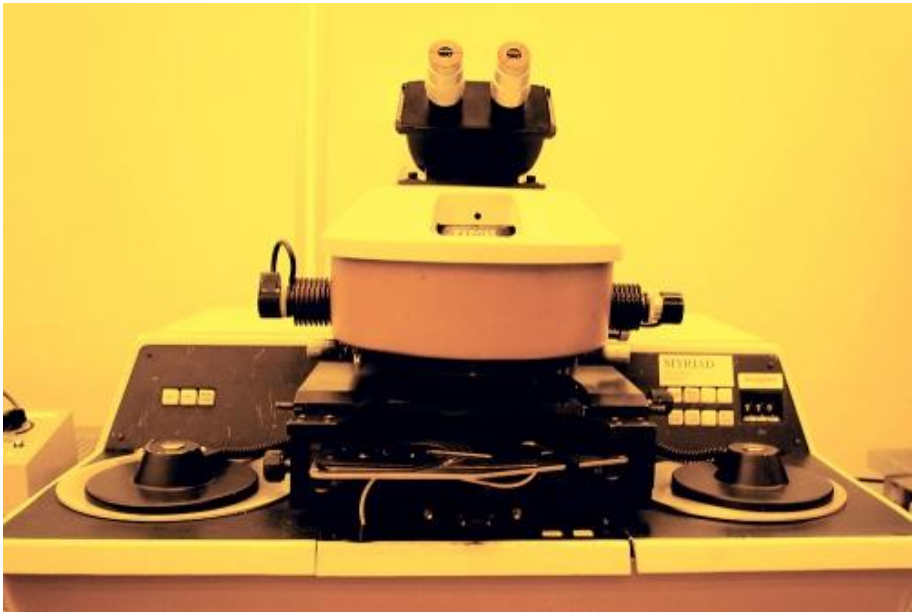

Figure 3.13. Kasper mask aligner in UH nanofabrication facility.

As soon as the layer is exposed the photo initiator decomposes to produce a photoacid (143) which in turn protonates the epoxides on the oligomer. The crosslinking reaction is initiated at this step which is enhanced further in the post exposure bake step.

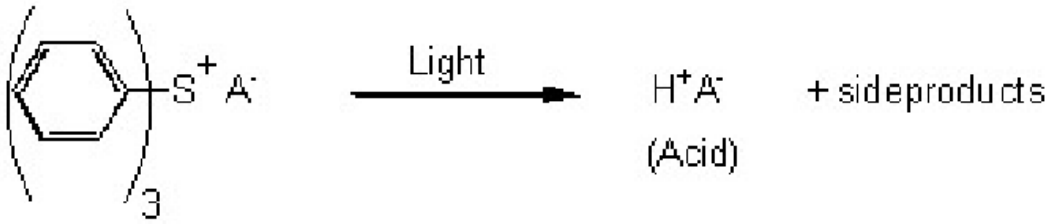

Figure 3.14. Photoimaging mechanism during the exposure.

The exposure enhances the adhesion between the substrate and SU-8 layer. Overexposure may lead to backscatter which will expose the required unexposed region; on the other hand underexposure may lead to peel off during development (154,159).

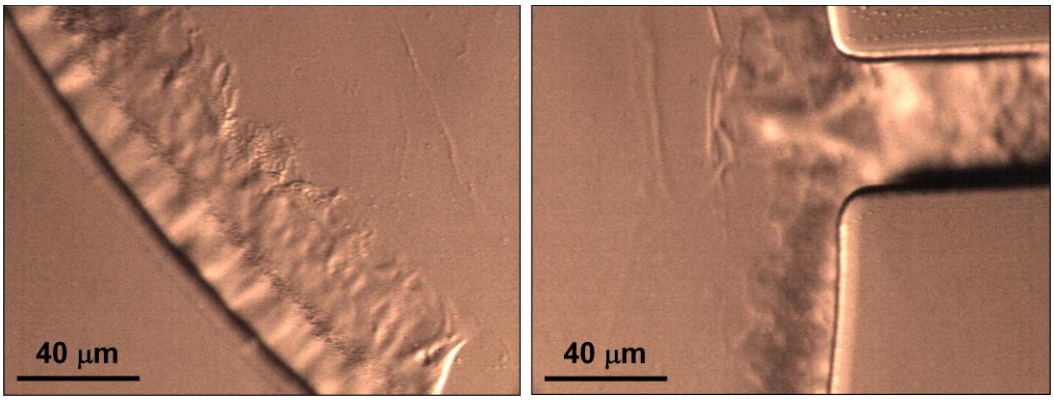

Figure 3.15. (a) Not straight walls and (b) residue of polymer in the channel. This illustrates the necessity of rigorous experimentation for optimizing the parameters during photolithography for glass substrate and SU-8 polymer combination.

In figure 3.15 we can see the effects of inappropriate exposure level and also it may be an artifact due to lower development time which we will discuss later. The exposure level is dependent upon the selective usage of filter (155). The low absorbance at higher wavelengths and reciprocal properties of SU-8 (141,160) and nonuniformity of the layer surface (140) cause mismatch of exposure among the top and bottom layer

which is known as top edge effect and diffraction error resulting in collapse of the structure (141). These defects can be reduced by introduction of a layer of glycerol in between the mask and SU-8 surface (141) and using a filter (160) to limit the band width of UV-light that is used for exposing the film. The filter only passes the UV lights that are above 350nm and hence reduces exposure non-uniformity inside the film.

In our case, we are using the filter and exposing the SU-8 layer for 75 s which is much longer than the exposure time 15 s when we did not use the filter. This demonstrates the lower absorption rate of energy by SU-8 layer at higher wavelengths.

G. Post-exposure relaxation: Post exposure relaxation is required for reducing the stress of the film and also for improving crosslinking and thereby adhesion to substrate of the SU-8 layer. The improved adhesion and crosslinking due to prolonged relaxation after exposure have been reported to extend to about 24 hours (152). In our case, we waited for 15 minutes for relaxation and this helped to reduce the stress that is in the film.

H. Post exposure bake: While heat is given after the post exposure relaxation of the film, as the kinetics of the crosslinking is very slow at room temperature, at higher temperature the mobility of the SU-8 molecules help to crosslink themselves better. The crosslinking is catalyzed by the photoacid which helps the SU-8 molecules to form epoxide bonds among themselves and with neighboring molecules (147). Longer PEB enhances crosslinking; on the other hand contributes to the residual stress if not controlled carefully (161). To avoid adhesion problem and reduce cracked area (152), primary heating at 65°C near T_g of SU-8 is conducted.

In our experiment, we do PEB at 65°C for 1 minute and at 95°C for 5 minutes. Optimizing this step is the key to have good result in the samples.

I. Predevelopment Relaxation: After the post exposure, cooling and relaxation is required to reduce the residual stress in the SU-8 film (154,162). This relaxation may take up to 48 hours depending on the layer thickness. In our experiment, we are using 24 hours relaxation time before development.

J. Development: The development of the image is done by washing with PGMEA (propyleneglycol monomethylether acetate**)** (135)**.** Developer solution diffusion depends on the time spent by the structure within the solution and also on the temperature of the solution (143).

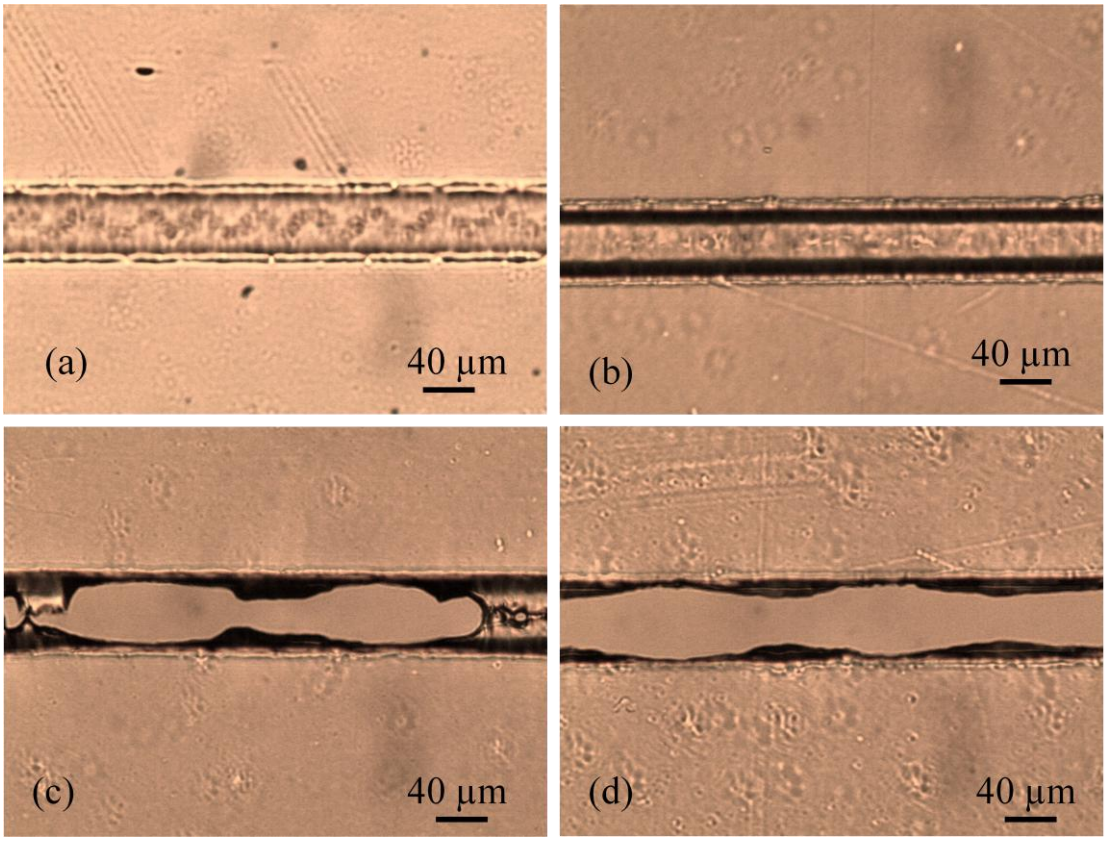

Figure 3.16. Multietching experiment for gradual development of the channel. (a) After 1st development for 30 s, (b) after 2nd development of 30 s, (c) after 4th development of 30 s and (d) after 5th development of 30 s.

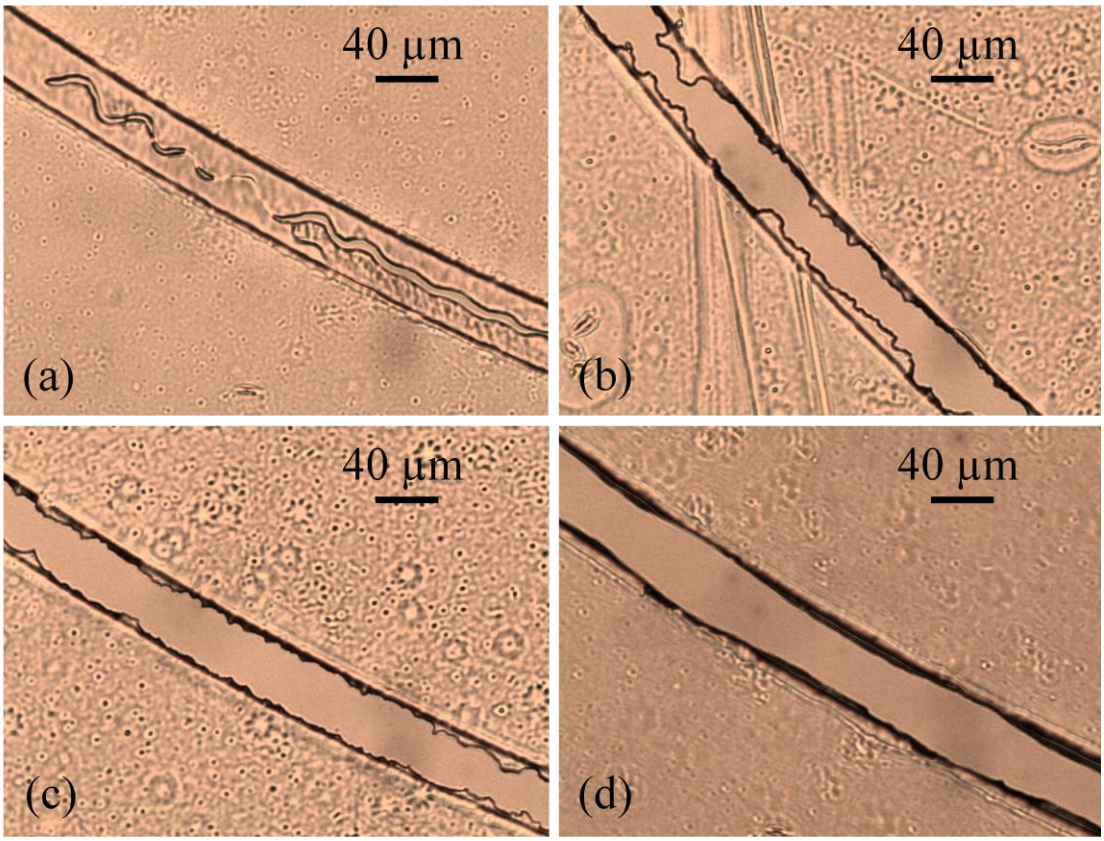

Figure 3.17. Multietching experiment for gradual development of the channel. (a) After 1st development for 10 s, (b) after 2nd development of 30 s, (c) after 3rd development of 30 s and (d) after 4th development of 30 s.

The residual stress developed due to the volume compression also adds to the problem which causes peeling off of the whole layer. The solvent evaporation during Isopropanol rinsing causes cracking to occur in the layer and the surface tension effect of the rinsing liquid causes capillary force to lead to debonding of the layer (143). These issues have to be handled with utmost care to ensure good layer adhesion.

We use ultra sonic bath to induce higher diffusion of developer into unexposed polymer layer and lower temperature (5˚C) to reduce the aggressive reactivity of the developer in our current formulation. The development is done in stepwise fashion where we do first development in 10seconds and subsequent developments are done at 30 seconds in each run till the channel gets the desired structure (figures 3.16. & 3.17.).

3.2.3. Channel quality, swelling tests and final recipe

After extensive trials following the requirements we were able to achieve very good formation of channels (as shown in figure 3.18) out of SU-8 following the above mentioned recipe. The figure shows the straight walls that we achieved and this is very crucial for the flow of fluid through the channel and also for avoiding nucleation from heterogeneous substrates. The junction is the point where the flow of HbS solution and silicone oil will come together to form droplets. The structure of junction is very crucial for obtaining required droplet dimensions and flow rates.

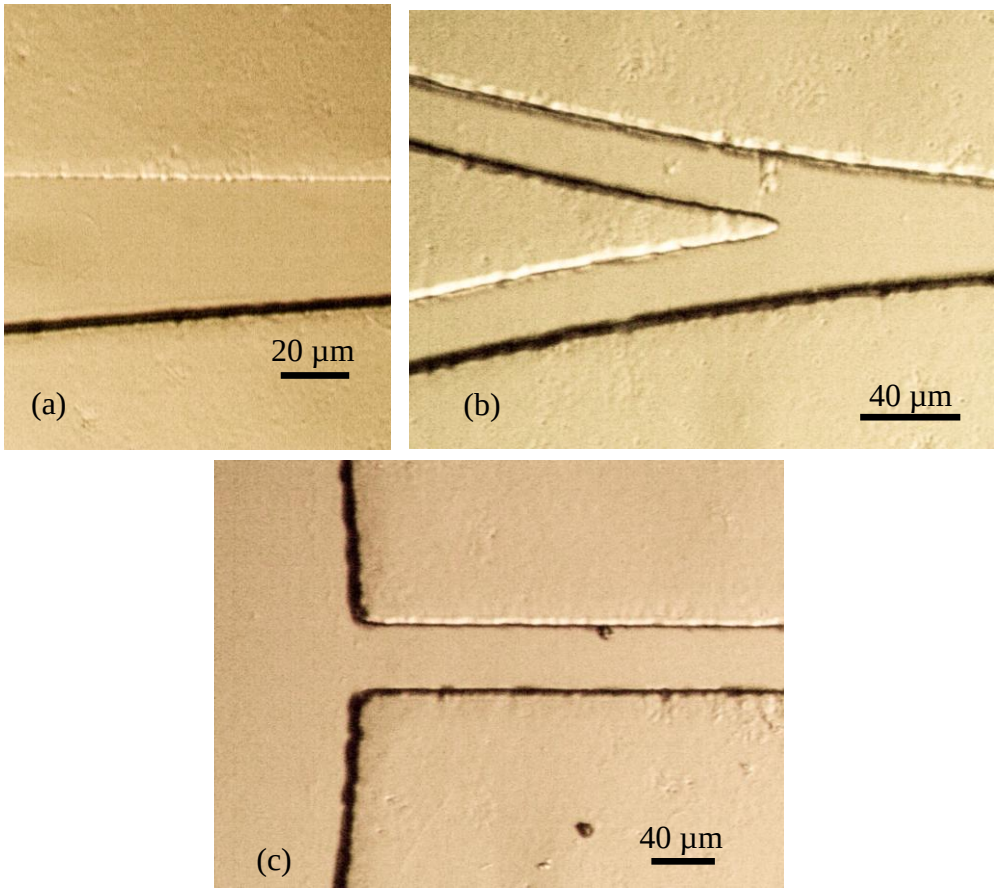

Figure 3.18. Segments of channels fabricated with SU-8 on glass substrate. (a) Channel inlet, (b) channel junction and (c) channel outlet. Straight walls of SU-8 layers are noticeable.

We also need to make sure that the solutions we will work with do not swell the SU-8 layer. If the solutions swell SU-8 layer, then we will not be able to use SU-8 as structure material. For this reason we examined the interaction of the SU-8 layer with different salts, physiological phosphate buffer (pH=7.35), silicone oil and water. From figure 3.19 we can see that water does not swell SU-8 layer.

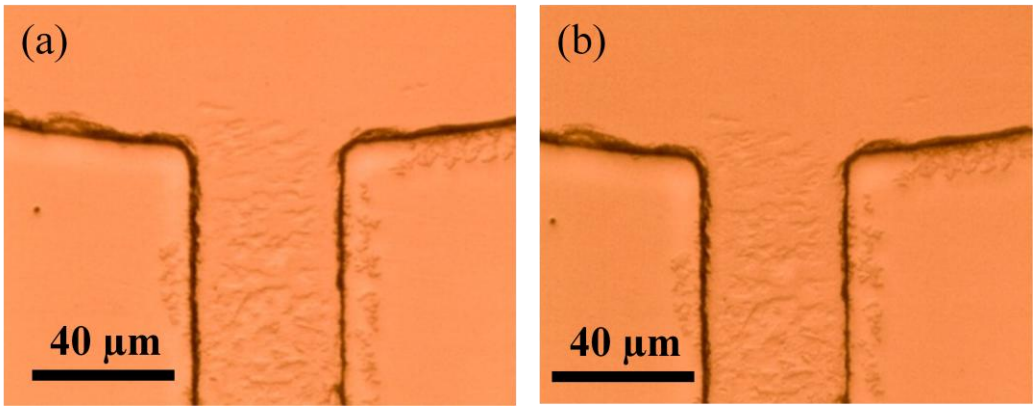

Figure 3.19. Swelling test of SU-8 layer with water. (a) Before adding water and (b) no swelling after 2 hours of adding water.

$CuCl_2$ swells the SU-8 layer which can be seen from figure 3.20. The swelling occurs very fast. Within an hour of adding $CuCl_2$ solution to the layer, the channel closed completely. This indicates very severe reaction of SU-8 layer with Cu^{+2} or Cl^{-} ions. Thus we wanted to try more salts to figure out which salts or ions may have effects on SU-8 layer. Comparing non-swelling behavior for sodium chloride (NaCl) and potassium chloride (KCl) [not shown here], we can conclude that chloride ion was not responsible for swelling. So it indicates that we cannot use Cu^{+2} salts with SU-8 layer.

We will be using phosphate buffered HbS solution. So we tested for swelling character of phosphate buffer at pH 7.35. The results obtained (in figure 3.21) show that phosphate buffer does not swell SU-8 layer even after three days.

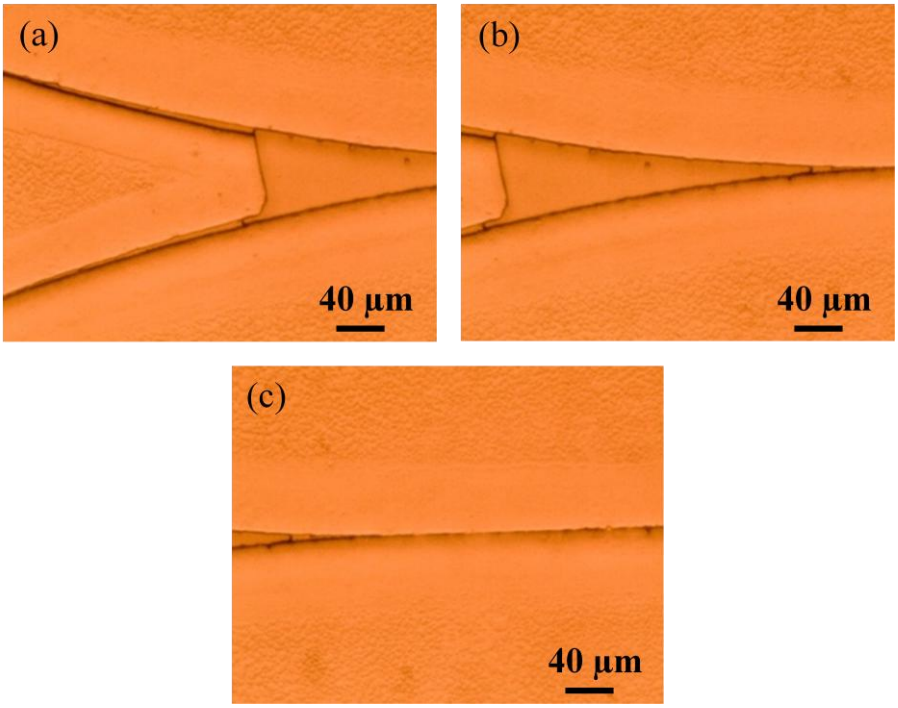

Figure 3.20. Swelling test of SU-8 layer with $CuCl_2$. (a) Channel junction without $CuCl_2$, (b) channel junction swelled and somewhat closed with $CuCl_2$ after 15 min, (c) channel junction swelled and completely closed after 1 hour.

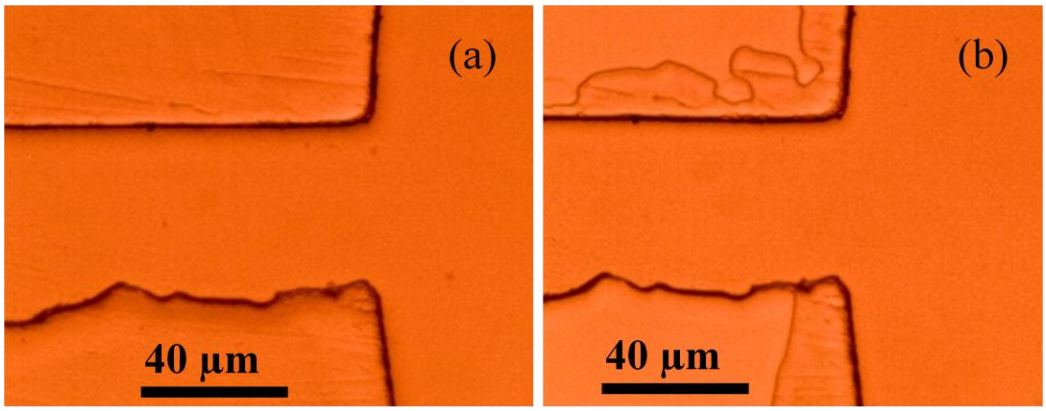

Figure 3.21. Swelling test of SU-8 layer with phosphate buffer (pH=7.35). (a) Channel without phosphate buffer and (b) channel with phosphate buffer after 3 days.

Using immiscibility of liquids we intend to create droplets of HbS solution separated by silicone oil. So we also checked the swelling characteristics of silicone oil on SU-8 surface and found out the SU-8 is not swelled by silicone oil (figure 3.22).

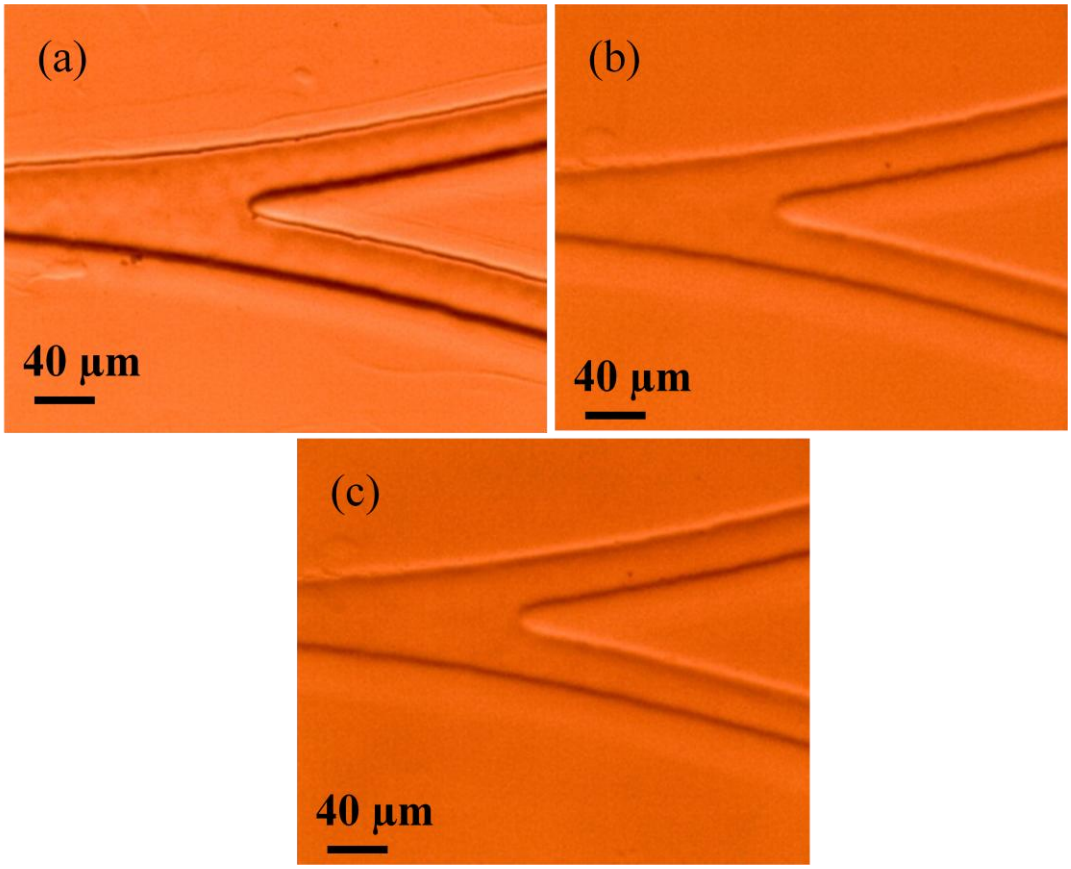

Figure 3.22. No swelling of SU-8 layer from Silicone oil. (a) SU-8 layer without silicone oil, (b) with silicone oil after 1 day and (c) with silicone oil after 3 days.

So from these experiments we can conclude that the solutions which we are going to use in our experiment such as phosphate buffer an silicone oil do not swell or interact with SU-8 layer and thus we can use SU-8 as structure material for our microfluidic channel.

Table 3.2. The final recipe for microfludics channel fabrication and comparison between procedures without filter and with filter.

Process	**Recipe w/o filter**	**Recipe with filter**
Cleaning	1. Soap cleaning in ultrasonic bath 2. Boiling in Sulfuric acid:Nitric Acid (3:1) Mixture 3. Acetone and DI water rinsing 4. Drying with air	1. Soap cleaning in ultrasonic bath 2. Boiling in Sulfuric acid:Nitric Acid (3:1) Mixture 3. Acetone and DI water rinsing 4. Drying with air
Dehydrate	10 min (150°C)	10 min (150°C)
Spin Coating	500 rpm @ 100 rpm/s (10 sec) 4000 rpm @ 300 rpm/s (20 sec)	500 rpm @ 100 rpm/s (10 sec) 3000 rpm @ 300 rpm/s (30 sec)
Post-coating relaxation	------	15-20 min
Soft bake	65°C/1 min 95°C/10 min (Ramped)	65°C/1 min 95°C/10 min (Ramped)
Pre-exposure relaxation & cooling	8 min	14-24 hour
Exposure	15 s	75 s
Post Exposure Bake	65°C/1 min 95°C/5 min (W/o ramping)	65°C/1 min 95°C/5 min (W/o ramping)
Post-exposure relaxation & cooling	4-5 min	14-24 hour
Development	15-30 s **(5°C)**	Step wise development in ultrasonic bath in ice-cold (5˚C) condition having first step for 10s and subsequent steps each for 30s
Rinse and dry	IPA & DI Water followed by air	IPA followed by air drying

Table 3.2 shows the final recipe which we are using to fabricate our channels at present. There are still scopes to improve the process parameters to make it more robust.

3.3. Conclusions

In this chapter, I presented the design considerations for new experimental setup for HbS polymerization study. I showed that SU-8 microfluidic structure fabrication depends on various process parameters such as substrate cleaning, exposure strength, development procedure etc. Interaction of SU-8 layer with different solutions and materials is discussed and I conclude some metal ions such as Cu^{+2} may lead to swelling of SU-8 layer. But the solutions which we intend to use do not interact with SU-8 layer.

CHAPTER 4

LOCALIZED MICROHEATER FABRICATION

For the localized microheater with fast egress to a chosen supersaturation value in the HbS solution, we chose heating the sample using a thin film resistance heater, based in Joule's law of thermal heating. Microheaters are basically popular in gas sensing microdevices and a lot of work has been done in this sector (163-165). Microscale gas chromatography development (166) and reactive biosensors (167) are among the driving forces for research in microheater sector. There are basically two types of microheaters (164): a) closed dielectric membranes and b) micro hotplate devices. Our microheater falls in the second category (168). There have been researches for finding out the best fabrication method for producing low cost microheaters (169). We decided to use the simplest of all: photolithography for patterning and thermal evaporation for metal deposition on the pattern.

We decided to fabricate the thin film microheater on the side of the coverslip that is not in contact with the channel and heat will be conducted through the 200 μm thick Goldseal cover glass No. 1. (48mm×65mm, 1 oz.). The overall fabrication process has three segments:

1. First we deposit a layer of AZ 1512 photoresist by photolithography to make the negative image of the pattern on the coverslip.
2. Then on that layer we deposit the metal layer by thermal evaporation.
3. After depositing the metal layer we etch the polymer layer with acetone and the final heater is outcome of the etching.

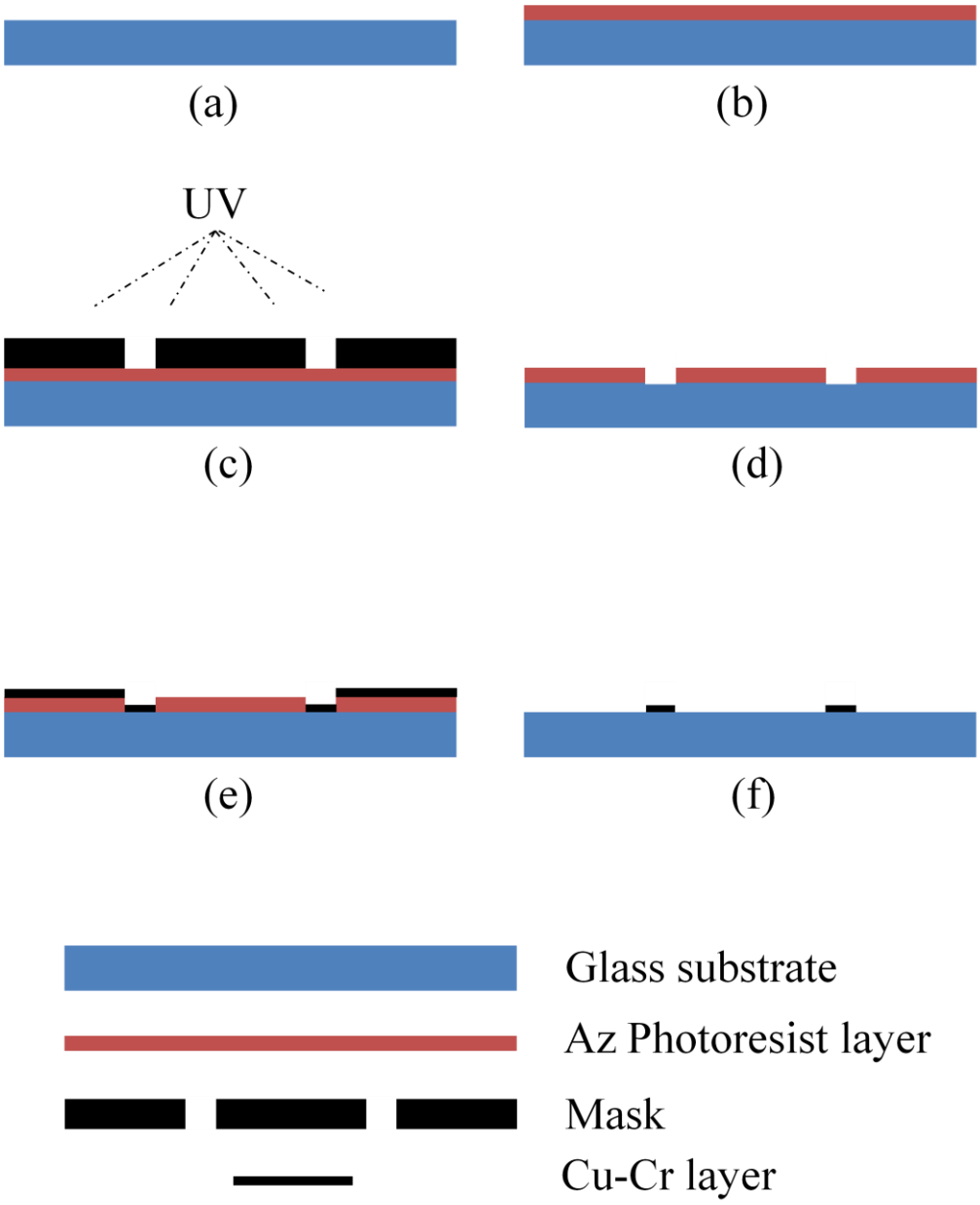

Figure 4.1. Overview of microheater fabrication process. (a) Cleaned glass substrate, (b) spin coating with AZ 1512, (c) mask aligning and UV exposure through mask, (d) development of AZ pattern, (e) thermal deposition of 110 nm of Cu-Cr layer and (f) removal of polymer layer and final thin film heater.

After fabricating the heater we calibrated it with infrared camera and also with Peltier element apparatus. We also did simulations to get a preliminary idea about the steady state and transient behavior of the system.

4.1. Recipe for polymer pattern formation, metal deposition and evolution of result

4.1.1. Polymer pattern formation

We used AZ 1512 photoresist to make the patterns required for thermal deposition on the microscope coverslip for fabricating microheater. AZ 1512 is a popular positive photoresist supplied by AZ electronics. It has very good reproducible characteristics for pattern formation. The process conditions are very mild and easily tunable. But we had to develop a well defined processing recipe as we had to deal with not so conventional substrate. The manufacturer recipe which is provided only for Silicon substrates does not cover the processing conditions which are required for the coverslips.

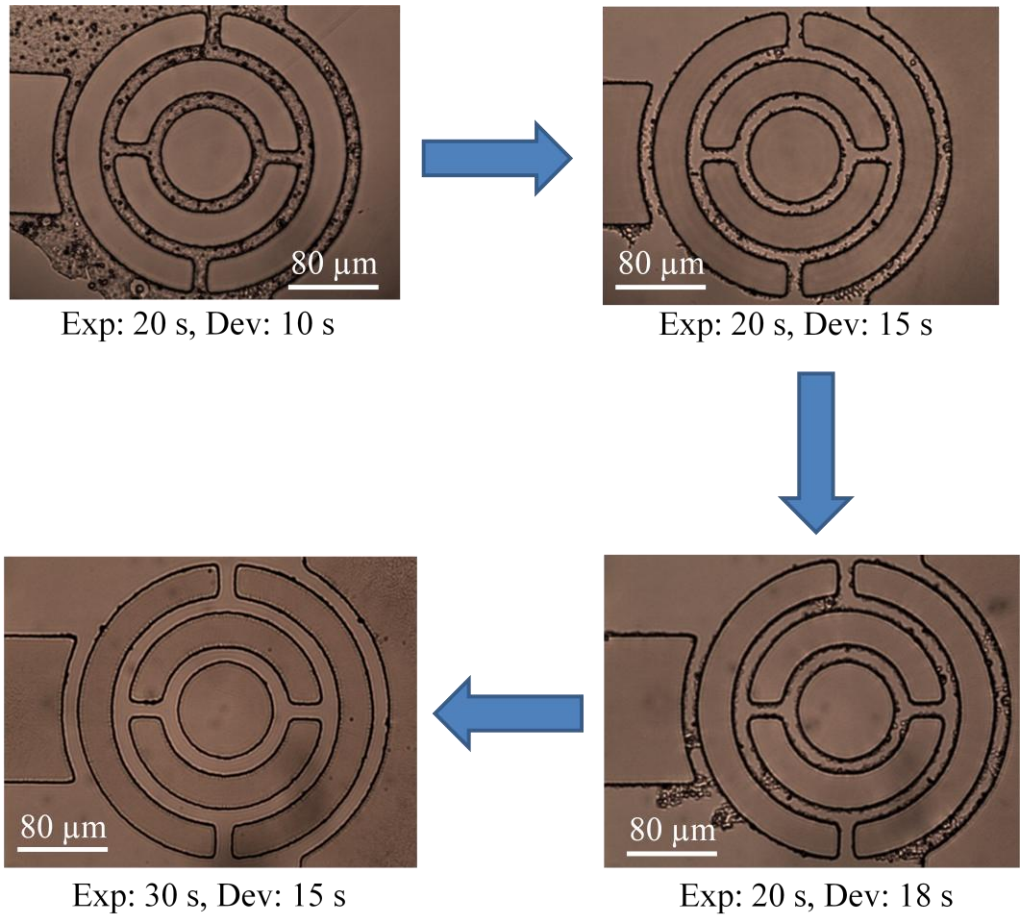

Figure 4.2. Gradual development of the recipe for microheater pattern fabrication using photolithography. ***Exp* means exposure time in mask aligner and *Dev* means development time for pattern formation.

We used plastic masks designed with autocad and manufactured by CAD/Art services Inc. For optimizing our own recipe, we started the experiments of microheater fabrication on 1mm thick glass and once we got good results with those samples, we moved into working with 200 µm coverslips. We found out that UV exposure and development times are the most important factors that affect the quality of the photoresist pattern on the glass substrate produced in clean room at UH nanofabrication facility. The exact combination of exposure time and etching time is found by numerous number of experiments. To get better resolution of the edges of the samples we used the same filter which we used in case of pattering SU-8 photoresist for microchannel fabrication. The experimental trial and error results are reflected in figure 4.2. In this figure we can see optimization of exposure time and etching time gradually. We can see that except for the final sample, there are remains of polymers at the bottom which would make metal layer deposition in those patterns unsuccessful.

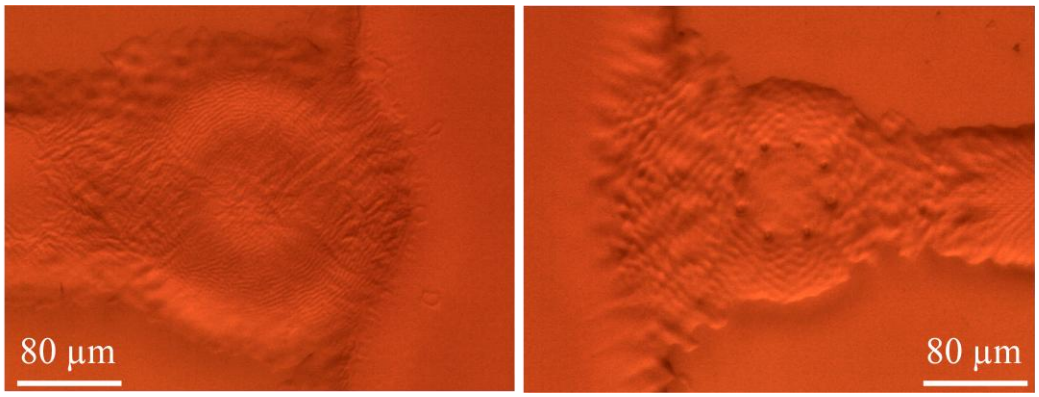

Figure 4.3. Examples of underexposed samples of AZ resist pattern.

From figure 4.3., we can see the effect of inappropriate exposure. As the exposure values were nor sufficient, the polymers did not dissolve after development properly and we did not get proper pattern formation.

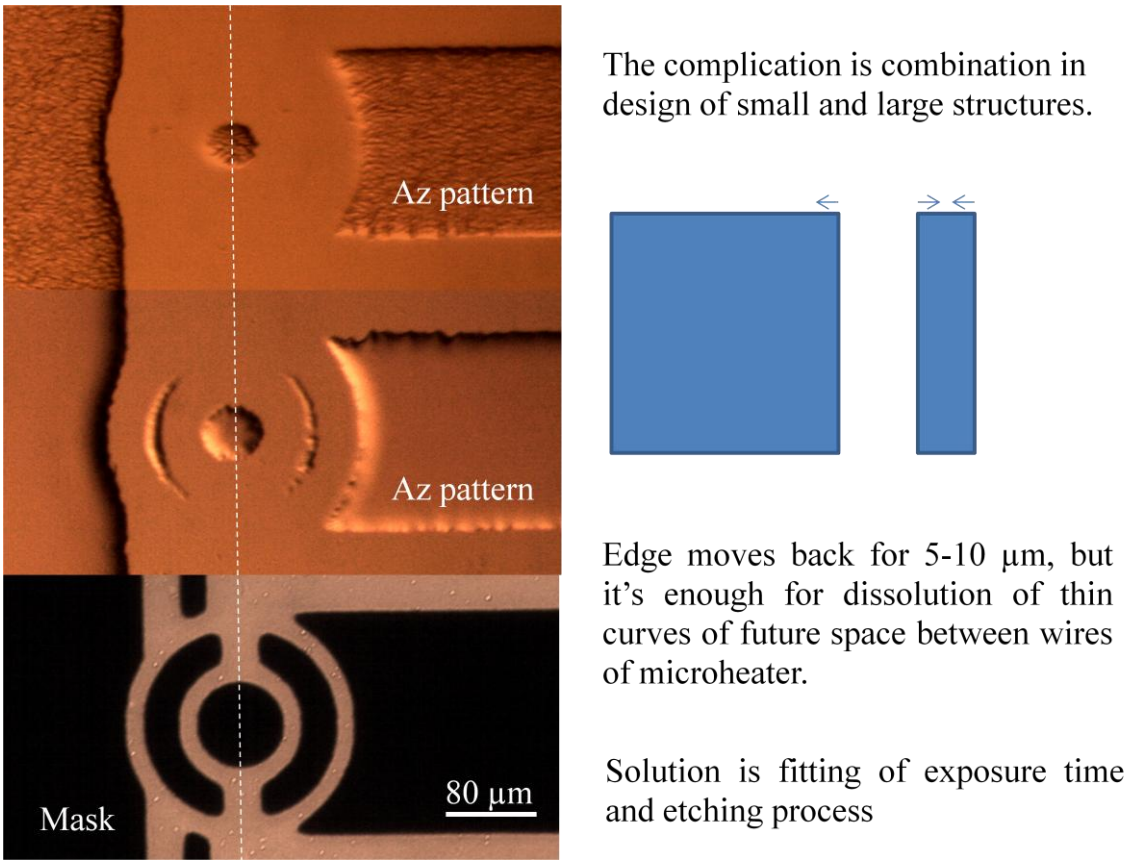

Figure 4.4. Effect of exposure time and etching process on the AZ photoresist pattern.

Figure 4.4. illustrates a unique observation where the exposure time and etching time combination affect the size variations in the structure and lead to undesired pattern formation. Basically inexact exposure lead to dissolution of small structures. Thus small patterns are not formed properly and eventually we cannot use these patterns for microheater fabrication though they may not have any polymer residue. These are the issues which have to be taken care of by using proper exposure time and etching periods. Considering all these factors and after numerous trials we came up with recipes which gives good pattern formation as in the last picture from figure 4.2. The final recipe with and without the filter and their comparison with the manufacturer recipe are given in table 4.1.

Table 4.1. The final recipe and comparison with manufacturer and recipe without filter.

Process	**Manufacturer Recipe w/o filter**	**Recipe with filter**	**Final recipe with filter**
Cleaning	1. Soap cleaning in ultrasonic bath 2. Boiling in H_2SO_4:HNO_3 (3:1) Mixture 3. Acetone and DI water rinsing 4. Drying with air	1. Soap cleaning in ultrasonic bath 2. Boiling in Sulfuric acid:Nitric Acid (3:1) Mixture 3. Acetone and DI water rinsing 4. Drying with air	1. Soap cleaning in ultrasonic bath 2. Boiling in Sulfuric acid:Nitric Acid (3:1) Mixture 3. Acetone and DI water rinsing 4. Drying with air
Dehydrate	10 min (150°C)	10 min (150°C)	10 min (150°C)
Spin Coating	500 rpm @ 100 rpm/s (10 sec) 4000 rpm @ 300 rpm/s (20 sec)	350 rpm @ 100 rpm/s (20 sec) 1200 rpm @ 300 rpm/s (25 sec)	350 rpm @ 100 rpm/s (20 sec) 1200 rpm @ 300 rpm/s (25 sec)
Post-coating relaxation	------	15-20 min	15-20 min
Soft bake	95°C/1 min	95°C/1 min	95°C/1 min
Pre-exposure relaxation & cooling	8 min	10 min	10 min
Exposure	30 s	20 s	30 s
Development	60-120 s	20 s	15 s
Rinse and dry	DI Water followed by air drying	DI water followed by air drying	DI water followed by air drying

4.1.2. Thin metal layer deposition and etching

Films which have thickness less than few microns and are created by condensing monolayer of materials on the surface are known as thin films (170). Thin films are produced by several established techniques which are mostly developed due to requirements arising in the MEMS industry. Figure 4.5 shows the classification of thin metal film deposition processes.

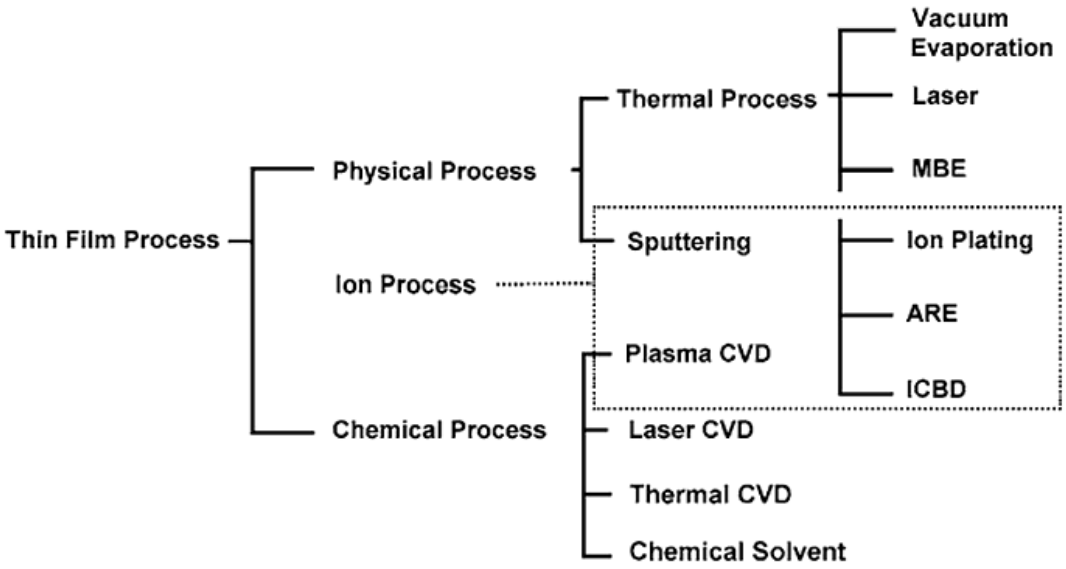

Figure 4.5. Classification of thin film deposition processes. (adapted from ref.170).

Thermal evaporation is one of the most used PVD methods of metal deposition on substrates in microfabrication processes. The material which needs to be deposited is used as a source material and it is evaporated under high vacuum in a resistively heated boat. The evaporated material travels to the substrate and condenses on it in a layer-by-layer fashion. The layers are monatomic. The schematic of the process can be seen from figure 4.6. We deposited thin metal layer on the patterned polymer layer by thermal evaporation using an in-house thermal evaporator under high vacuum in Dr. Paul Ruchhoeft's laboratory.

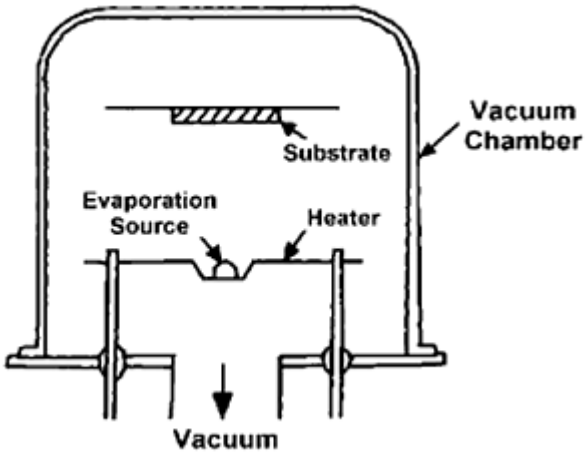

Figure 4.6. Schematic of thermal evaporation process. (adapted from ref. [170]).

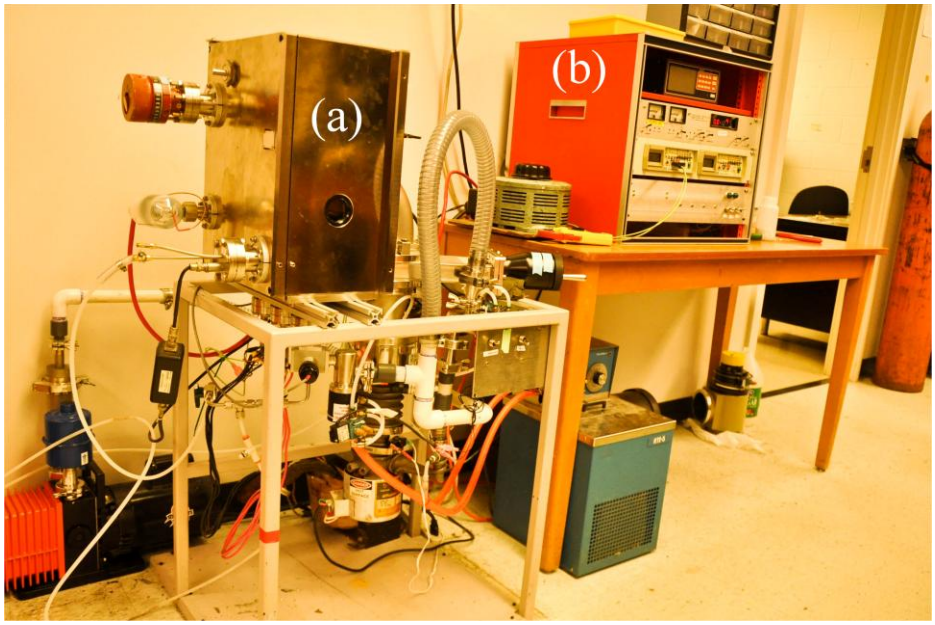

Figure 4.7. Thermal evaporator setup for metal thin film deposition: (a) evaporator chamber and (b) evaporator monitor and control module.

Figure 4.8. Schematic cross-sectional view of the microheater on the cover glass.

We tested different materials for fabricating the resistive microheater. At first we successfully deposited 100 nm nichrome ($\alpha = 0.0004\Omega^{\circ}C^{-1}$) layer but this gave us very poor temperature resistance coefficient. Then we decided to fabricate the microheater from Platinum (Pt), known as the best resistive heater material ($\alpha = 0.00392\Omega^{\circ}C^{-1}$). But the robustness of the thermal evaporator was not sufficient to give us the desired evaporation temperature for Pt pellets. Thus we decided to use copper (Cu) ($\alpha = 0.0039\Omega^{\circ}C^{-1}$) as the material of construction. At first we could not achieve good adhesion of Cu because it does not stick well to glass substrate. But then we decided to add a layer of very thin (~10 nm) of Chromium (Cr) between the Cu layer and glass substrate. This resulted in good adhesion of thin film to the substrate. Thus our present thin film heater is constructed of first a Cr layer of about 110 nm and then a 100 nm layer of Cu as shown in figure 4.8. After metal deposition we use acetone with Q-tips carefully to etch the AZ 1512 polymer from the coverslip to bring out only the thin film layer.

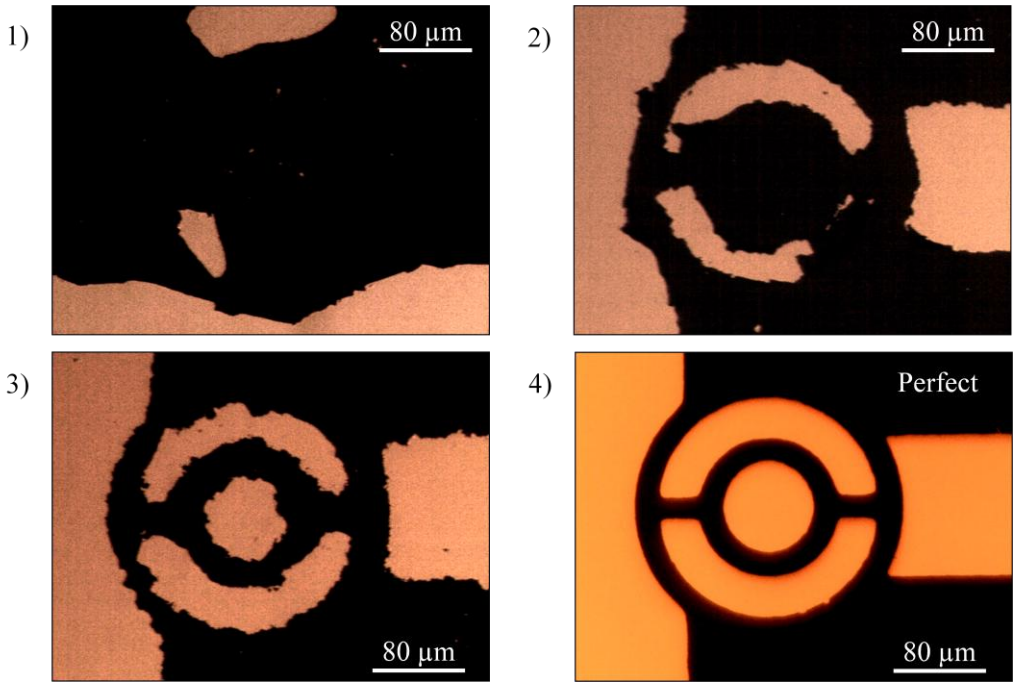

Figure 4.9. The progress in microheater fabrication (micrographs of heater sample with 160 µm outer diameter).

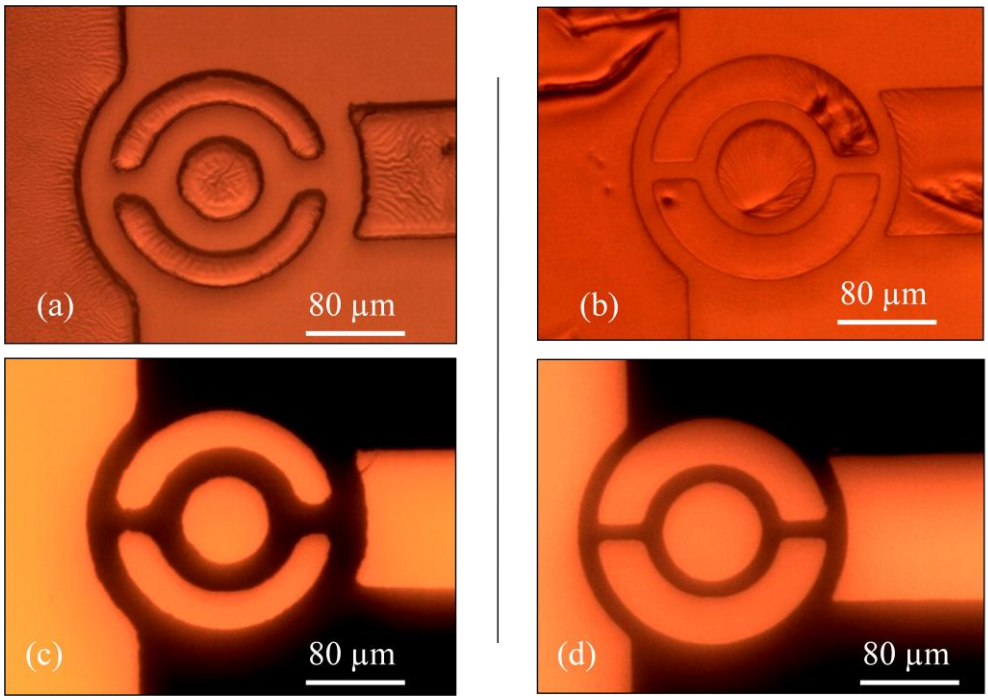

Figure 4.10. Comparison between AZ 1512 patterns (a, b) and corresponding heater samples (c, d, respectively) depending on use of quartz filter. Edge effect from AZ patterns depending on the processing conditions.

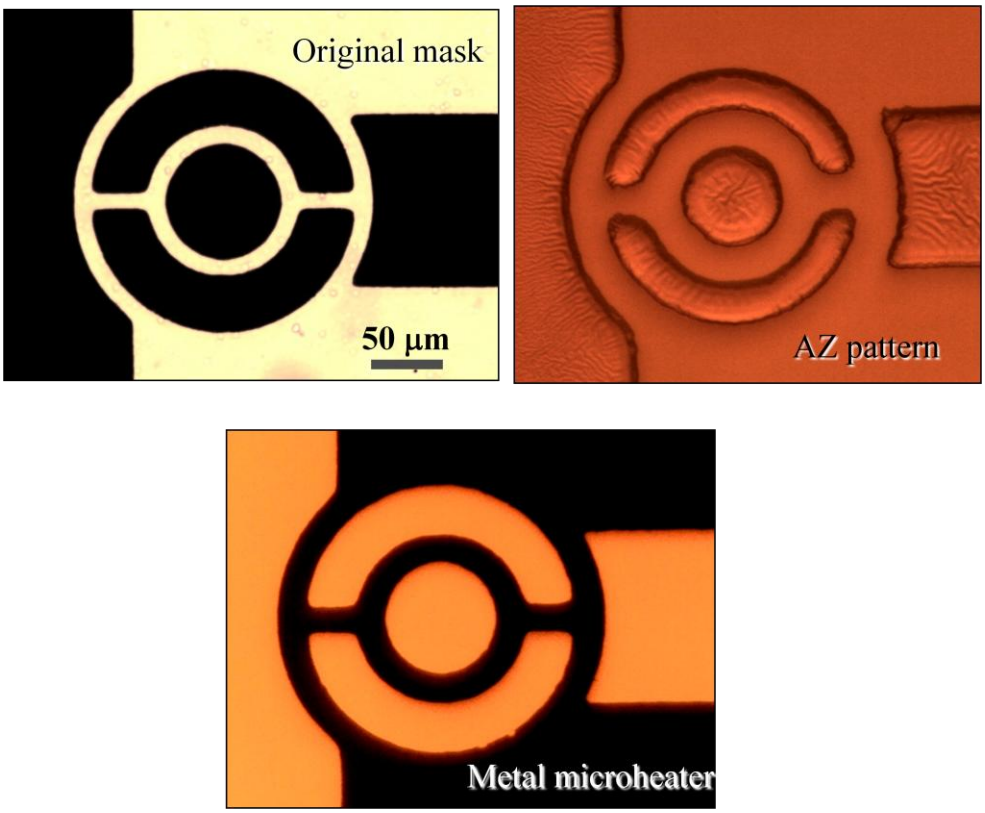

Figure 4.11. The transition of designed mask to photolithographic pattern and then realization into desired thin film heater.

From numerous fabrication attempts we find that the AZ photoresist pattern formation largely affects the sharpness of the edges of the final microheater sample as can be seen from figure 4.10. The final realization of the heater is given in figure 4.11 and figure 4.12 shows the substrate after three consecutive stages of fabrication.

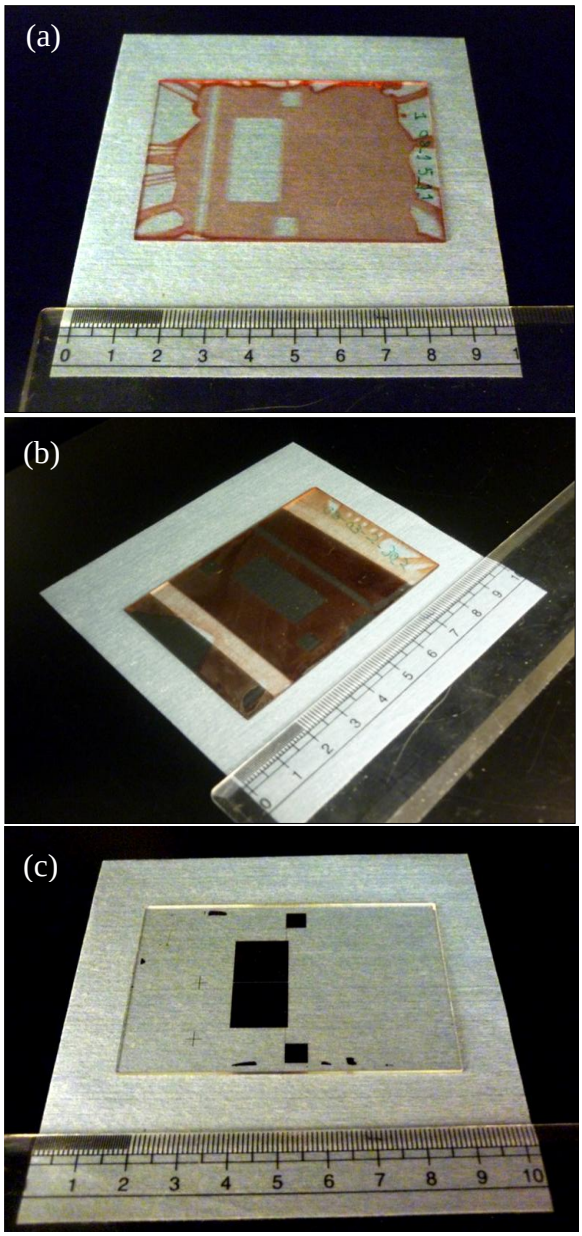

Figure 4.12. Sample view after each stage of microheater fabrication: (a) sample after spincoating and development of AZ 1512 polymer layer on coverslip, (b) sample after thermal deposition of metal with polymer layers and (c) final sample only with thin metal layer after etching of polymer layer.

4.2. Heater contacts and calibration

As the dimensions of our microheater are quite small (on the order of hundreds of microns), it is not possible to attach any thermocouple or RTDs to measure the temperature of the droplet. Thus we use voltage difference to calculate the resistance and from the resistance know the temperature. For this reason we need to calibrate the heater and know the relationship between the resistance and temperature.

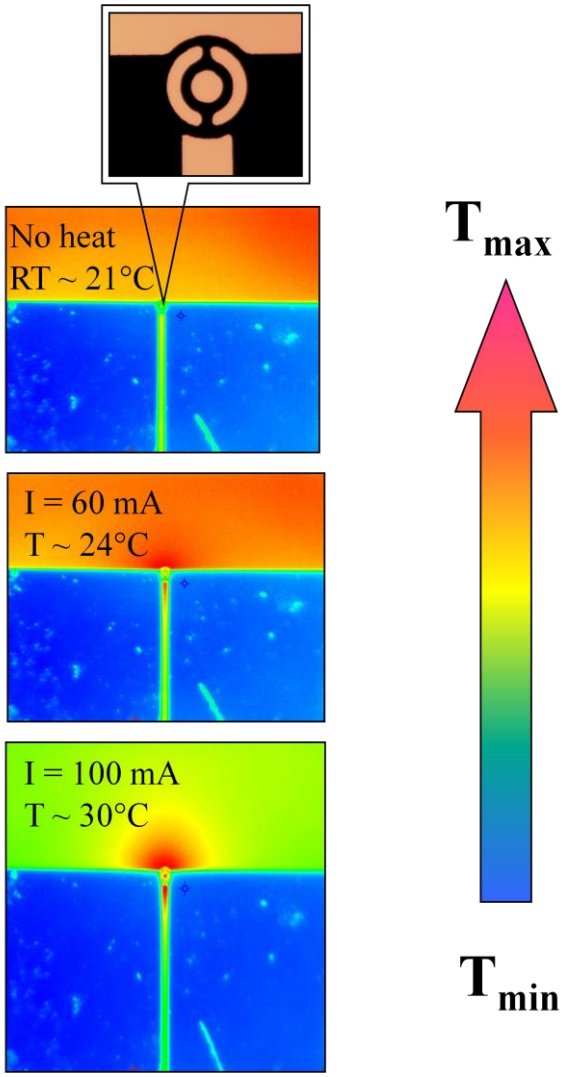

Figure 4.13. Infrared camera pictures showing resistive heating in microheater. (160 μm heater diameter).

After we have fabricated the thin film heater, we prepare the contacts from copper tape and glue them using conductive electrical paste Conducto-lube (from Cool-amp) with the lids of the microheater. We connect the copper lids using alligator clips to Keithley 2400 power source and voltage measurement device NI-6361 from National Instrument. Then we supply current starting from the order 10 mA to 100 mA. The resistive heater gets heated at the centre and the temperature rise has been observed by infrared camera. We have evidence of heating from infrared camera as in figure 4.13. From infrared camera calibration test we have found an upper bound for applicable current for our configuration of 160 µm outer diameter heater. This is about 120 mA above which burn out of the heater occurs due to large increase in the resistance coefficient of temperature of the thin film material. It can be seen from figure 4.14.

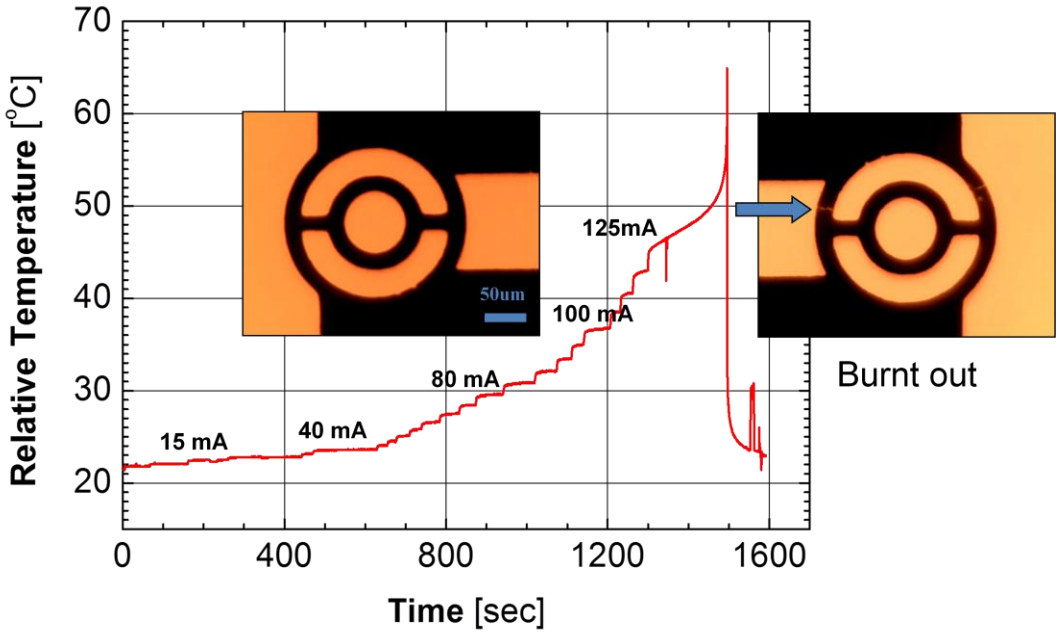

Figure 4.14. Calibration of microheater with infrared camera.

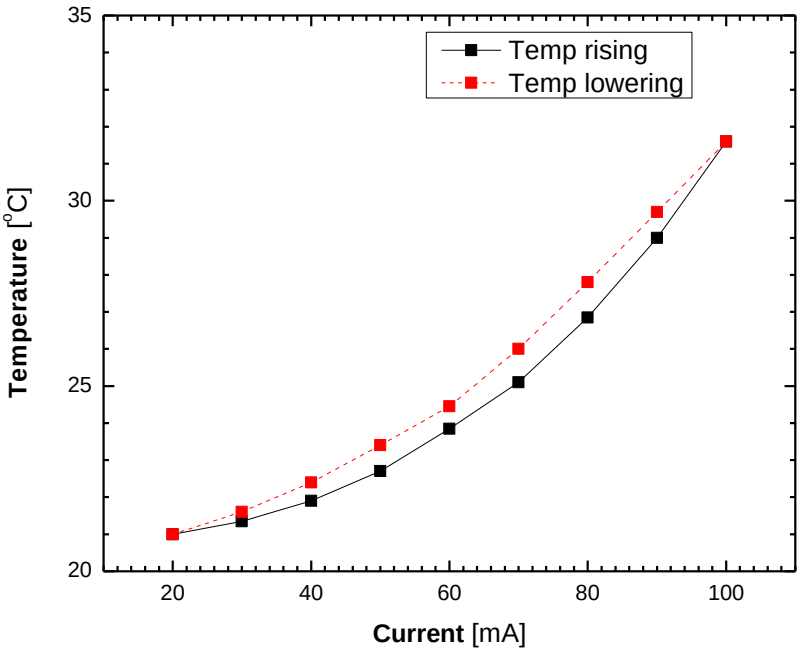

Figure 4.15. Quadratic dependence of temperature on current and hysteresis from infrared camera calibration data.

The temperature data from another set of experiment with infrared camera (figure 4.15) show quadratic dependence on current which is the characteristic of Joule's resistive heating. But we also notice an interesting thing that the temperature rise from and decreasing back to room temperature through current supply has a hysteresis pattern. There may be two possibilities. First, this may be an artifact of experiment as the time interval for the ramping up and coming down was not much. So the heater may not have sufficient time to come back to the corresponding value of temperature. On the other hand, it may reflect one important characteristics of the microheater, lag time and this may interfere in our experiment in future if we want to have some fluctuating operating temperature. To ensure better calibration, we must get rid of such hysteresis.

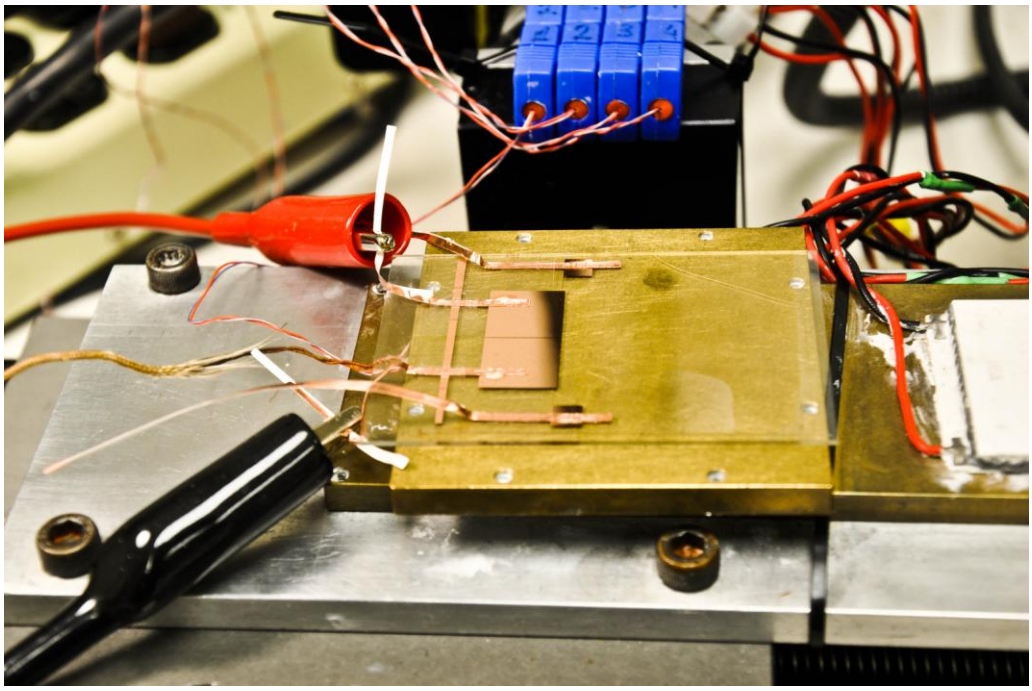

Figure 4.16. Heater sample with Cu tape contacts on the Peltier element apparatus.

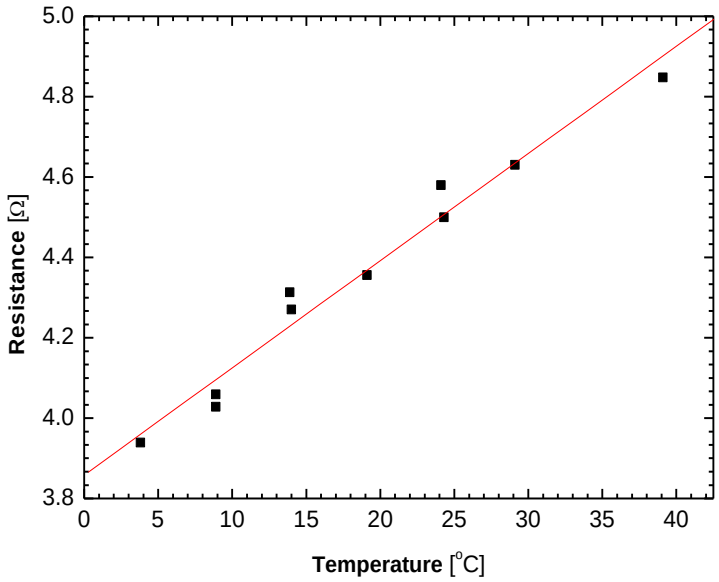

Figure 4.17. Resistance versus temperature calibration curve from Peltier element giving temperature coefficient of resistance value of 0.026 $\Omega^{\circ}C^{-1}$.

We use Peltier element to calibrate the heater with respect to resistance to find out the temperature coefficient of resistance ($\Omega^{\circ}C^{-1}$) of the heater material. This helps us to

know the relationship among the voltage, current, resistance and temperature when we analyze the data from infrared camera and Peltier element apparatus together.

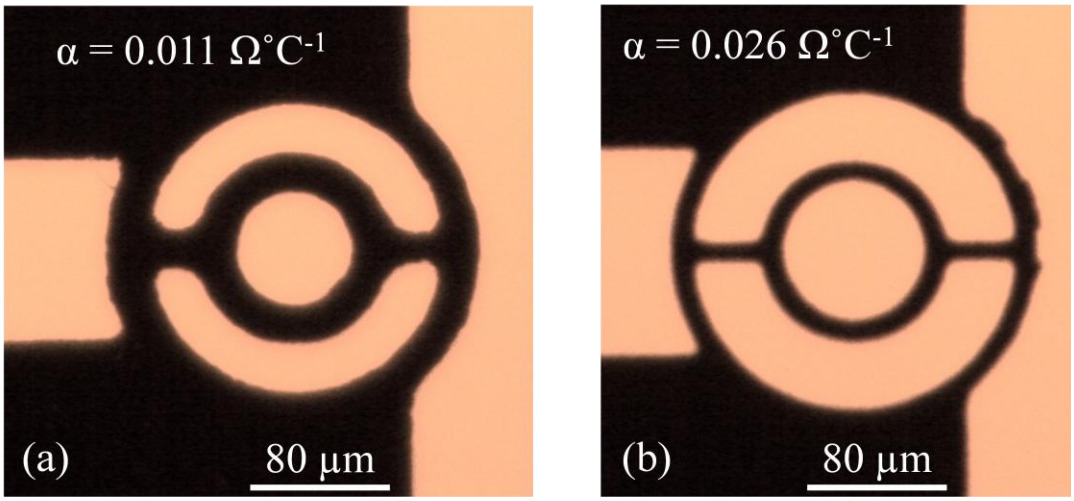

Figure 4.18. The dependence of temperature resistance coefficient on the shapes of the heaters which result from different fabrication parameters. (a) Microheater fabricated on thick glass without quartz filter and (b) microheater fabricated on thin glass with quartz filter.

In figure 4.17, we show the resistance dependence on temperature for the heater showed in figure 4.18(b). From figure 4.18, we also see the dependence of temperature resistance coefficient on heater shape as the values are quite different for two slightly different shapes differing in the fabrication procedure. The values are 0.026 $\Omega^{\circ}C^{-1}$ and 0.011 $\Omega^{\circ}C^{-1}$ respectively. From this we reason that the calibration of heater is not universal. It depends on the fabrication parameters. So we will have to do calibration for each heater separately. This emphasizes the need of better calibration procedure which will ensure less error in the measurements and more reliability. This also demonstrate the need for a very consistent fabrication recipe.

4.3. Computer simulations performed

For the purpose of obtaining supersaturation, our goal is to ramp the temperature of the HbS solution droplet from 5˚C to 25˚C by resistive heating. The time required for the heating should be very small e.g., on the order of 10-100 ms to be comparable with the timescale of nucleation. Initially we had a design for the heater which was based on our primary calculation to start with. In that design we had one ring of heater in the centre as the heating element and the outer diameter of the heater was 160 μm. After some experimental determination of the heater temperature, we decided to improve our heater deign based on steady state and transient state simulations. For this reason we carried out steady state and transient state simulations in ANSYS FLUENT software. Aritra Sur, graduate student working with Dr. Dong Liu at Mechanical Engineering, performed the simulations.

For the simulation purpose, we used a simpler geometry. We assumed the whole microfluidic chip to be a block of 5×5 mm^2 area and 1.2 mm of height. This block is made of the same material as the glass substrate for the channel. The heater is at the centre of the bottom surface. The assumptions behind smaller description of the chip is that the dimensions of the chip (3000×2000 μm^2) compared to the small microheater (160 μm diameter circular area of thickness 10 μm) is 1000 times greater. So the effect on the entire chip would be negligible and the approximation would be quite practical. There is a control volume of air to account for the natural convection from the environment. The control volume is attached to the heater side of the chip and has double the height of the chip and same area. We neglected the top surface convection due to Boussinesq approximation. The geometry is depicted in figure 4.19.

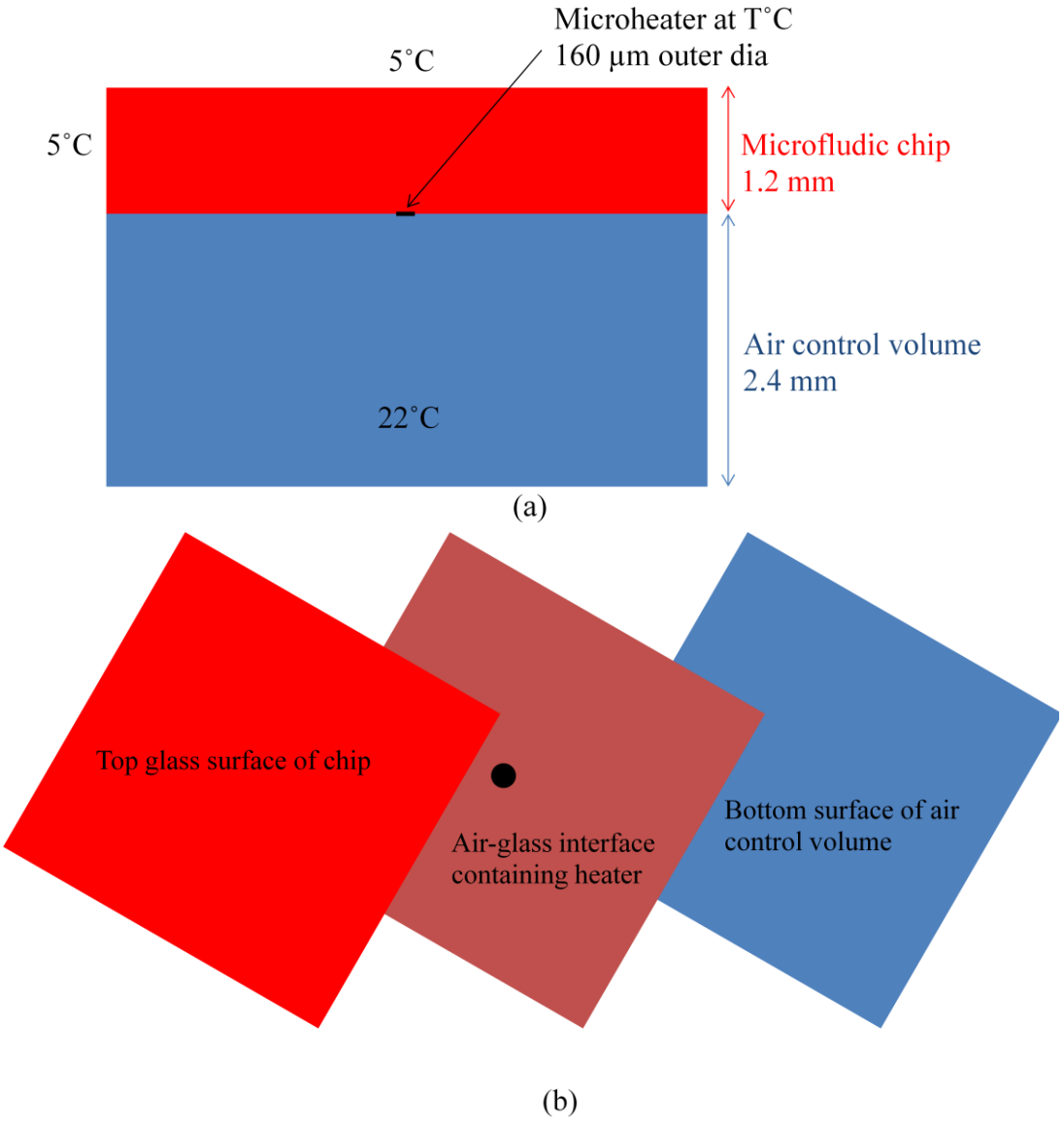

Figure 4.19. (a) The cross-sectional view of the simulation geometry and (b) top view of the simulation geometry.

ANSYS FLUENT solves the energy equation in the following form:

$$\frac{\partial}{\partial t}(\rho E) + \nabla.(\vec{v}(\rho E + p)) = \nabla.(k_{eff}\nabla T - \sum_j h_j \vec{J}_j + (\overline{\overline{T}}_{eff}.\vec{v})) + S_h \qquad (4.1.)$$

where k_{eff} is the effective conductivity (k + k_t, where k_t is the turbulent thermal conductivity, defined according to the turbulence model being used), and J_j is the diffusion flux of species j. The first three terms on the right-hand side of equation 4.1.

represent energy transfer due to conduction, species diffusion, and viscous dissipation, respectively. S_h includes the heat of chemical reaction, and any other volumetric heat sources. When heat is added to a fluid and the fluid density varies with temperature, a flow can be induced due to the force of gravity acting on the density variations. Such buoyancy-driven flows are termed natural-convection (or mixed-convection) flows and is modeled in ANSYS FLUENT. The boundary conditions are also shown in figure 4.19(a). We took air temperature to be 22˚C and also took the whole chip to be at 5˚C initially. We varied the heater temperature to find out the steady state temperature distribution and also in case of transient state of the system to find out the time required to reach steady state. The results and plots are summarized below.

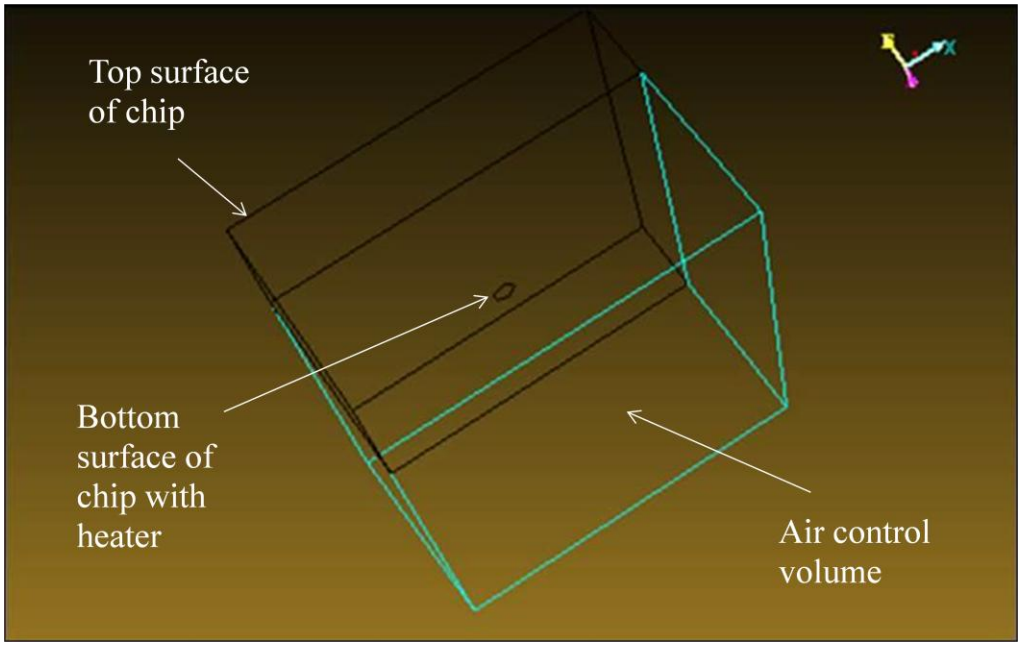

Figure 4.20. Simulation geometry in the ANSYS FLUENT environment.

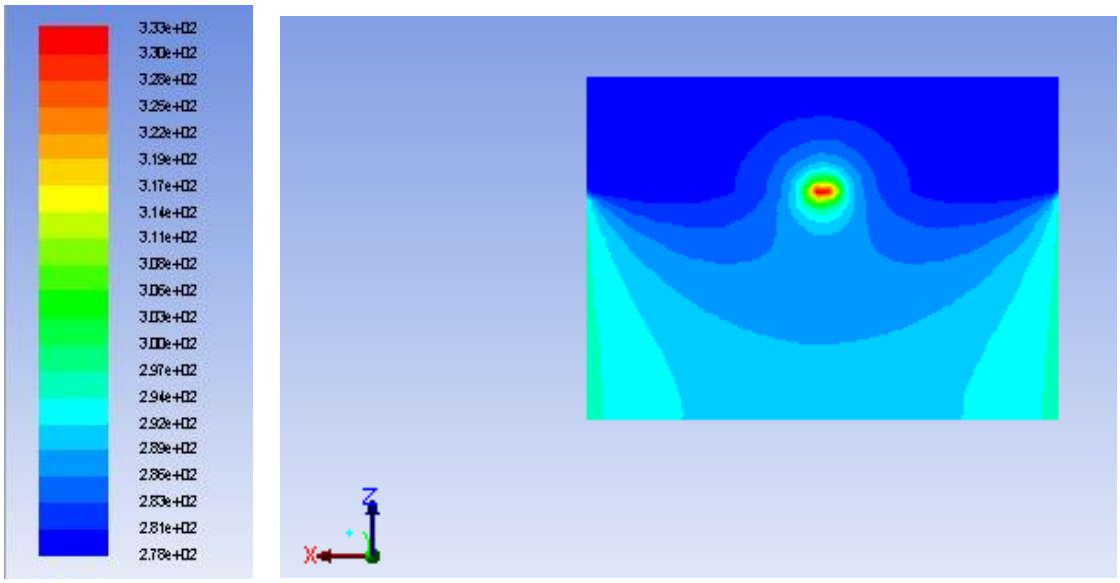

Figure 4.21. Temperature distribution through the central part of the geometry for heater temperature of 60˚C.

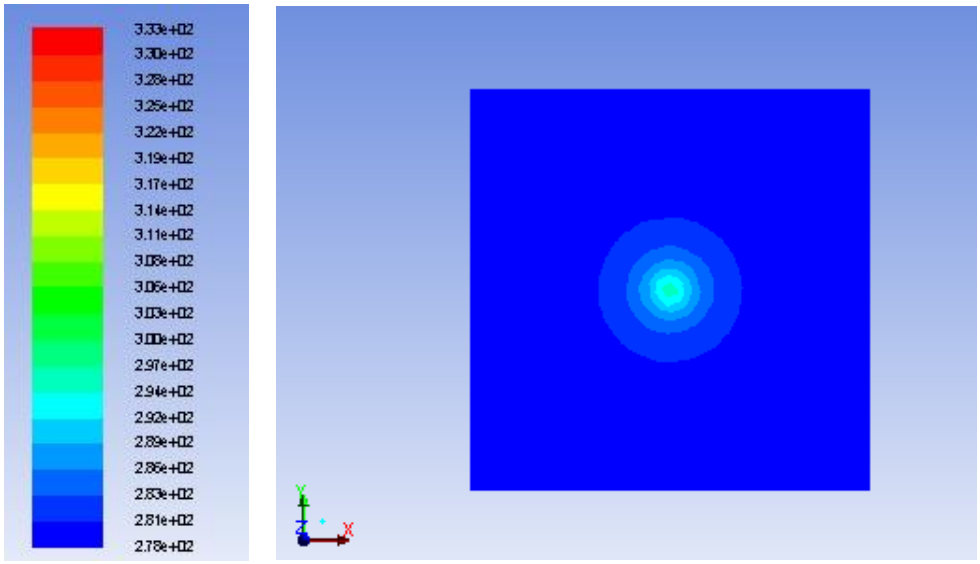

Figure 4.22. Temperature distribution at the channel surface i.e., 0.2 mm above bottom of chip for heater temperature of 60˚C.

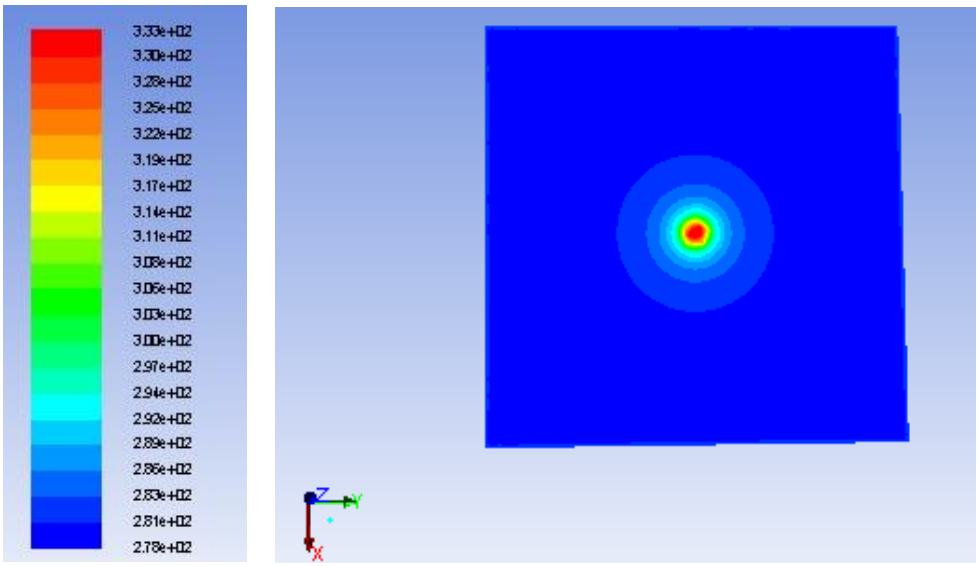

Figure 4.23. Temperature distribution at the heater surface i.e., at bottom of chip for heater temperature of 60˚C.

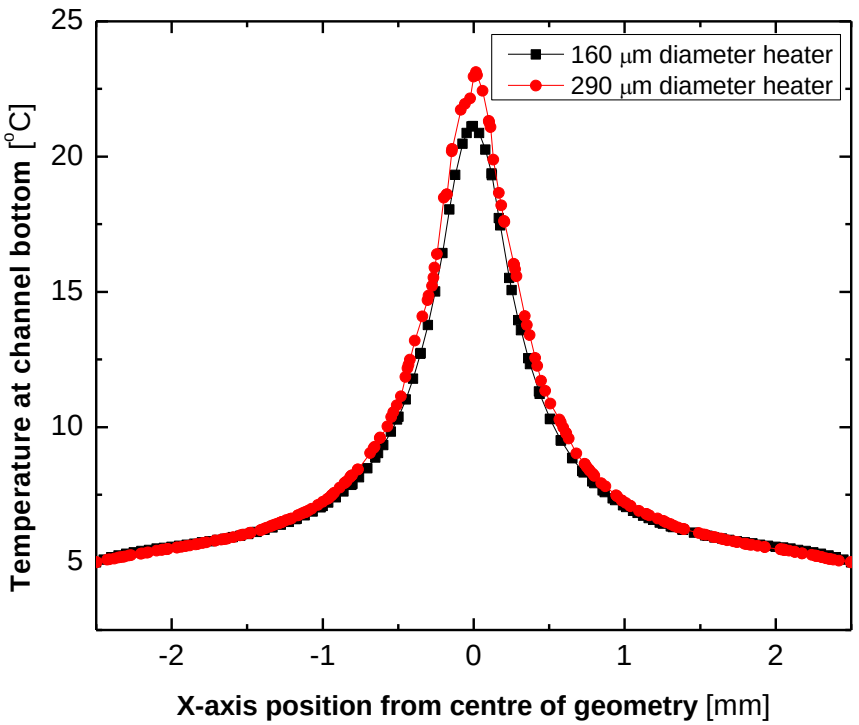

Figure 4.24. Temperature distribution at the channel bottom along the central line for heater temperature of 60˚C.

The steady simulations of heater temperature indicate that the 160 μm diameter heater cannot go to the desired operating temperature of 25˚C. It also shows that if we use larger heater diameter, then it will be able to achieve the higher temperature as can be seen from the plot in figure 4.24.

Hence we redesigned our heater with 290 μm outer diameter as shown in figure 4.25. Then we ran the simulations with redesigned heater. From the steady state simulations, we can find a linear relationship between the heater temperature and the channel bottom temperature which we can use to know the exact droplet temperature (figure 4.26). Combining this data with infrared camera data we will be able to estimate the power requirement for the specific droplet temperature. Temperature field distributions from simulations (figures 4.24. & 4.26.) are crucial as we will store droplets away from the heater centre and do not want the droplets to be heated earlier.

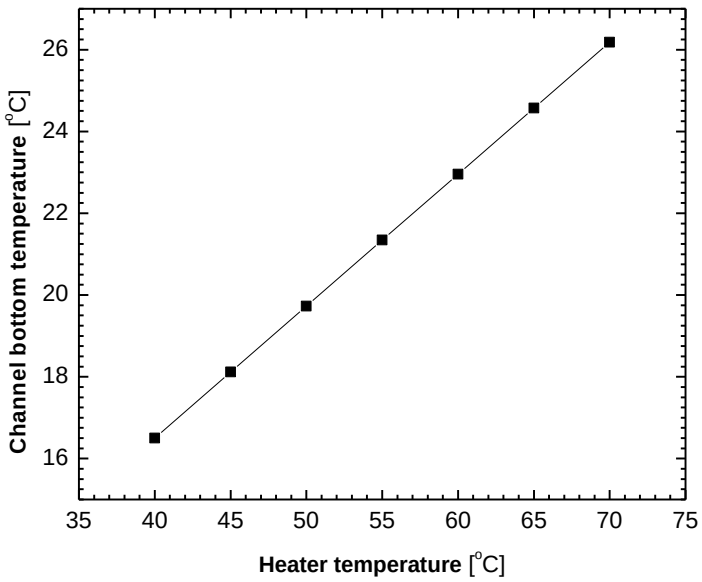

Figure 4.25. Linear relationship between heater temperature and channel bottom temperature obtained from steady state simulation; (290 μm heater diameter).

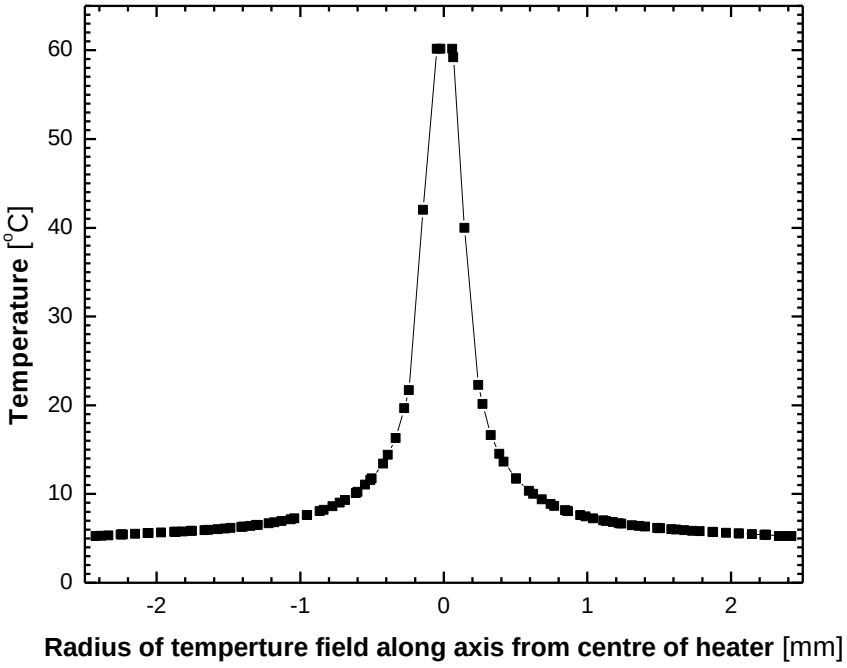

Figure 4.26. Radius of temperature field on the surface as a function of current.

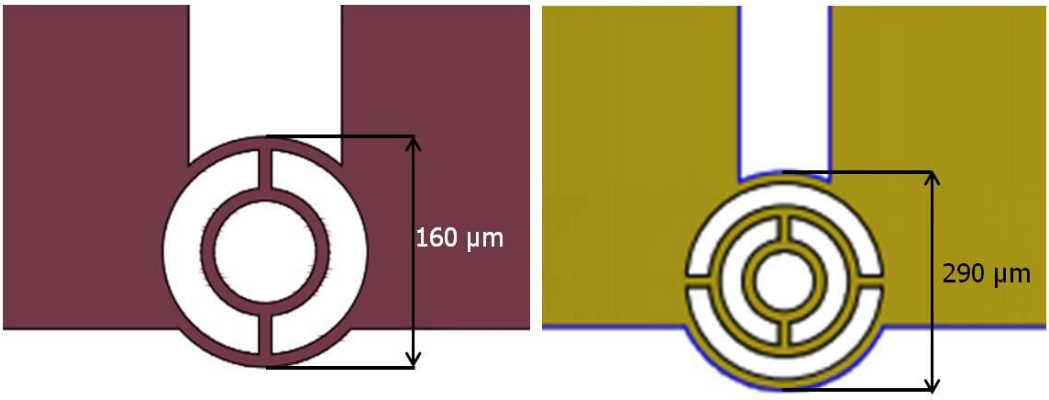

Figure 4.27. The change in the design of heater based on the simulations. (a) illustrates the old design having two rings with outer diameter 160 µm and (b) shows new design having three rings with outermost diameter being 290 µm.

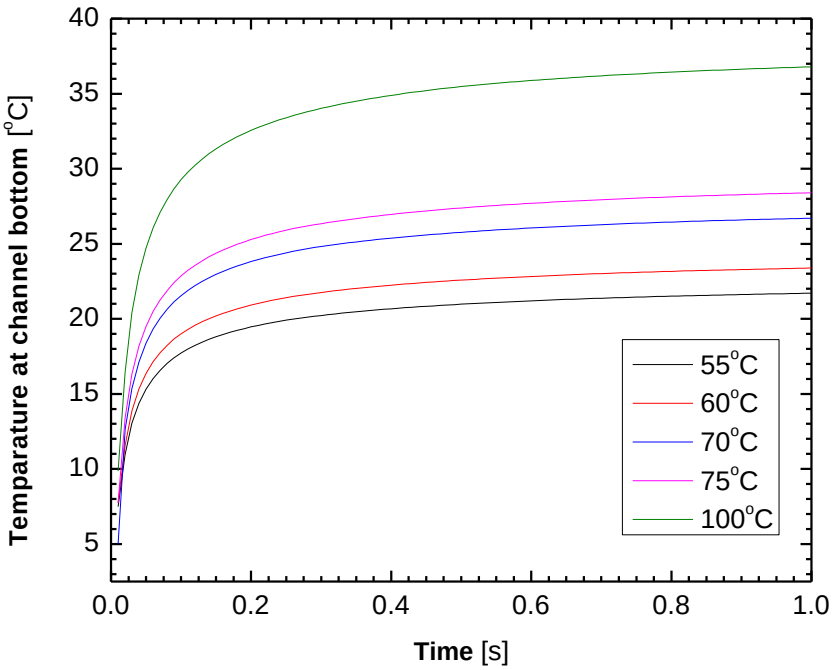

Figure 4.28. Transient temperature data at the channel bottom for different heater temperatures; (290 µm heater diameter).

The transient state simulation results (figure 4.28) show that with 100˚C heater temperature, the desired 25˚C temperature can be achieved within 50 ms, though it will take more time to stabilize. This data will be useful for us to design our control parameters for temperature management.

4.4. Experiments performed to compare simulation data

To compare the simulation data we try to find the temperature distribution experimentally. Though there are still scopes to improve the experimental setup, we are discussing the primary results here. From the simulations we can obtain the temperature distribution at the bottom of the chip where the heater is situated as shown in figure 4.26. Now we design an experiment where we keep the heater sample in the same way that it

will be in the chip i.e., in conjunction with 1 mm glass substrate. Then we place the conjugated chip on Peltier element apparatus where the heater is faced up and the opposite side of the chip is attached with Peltier element.

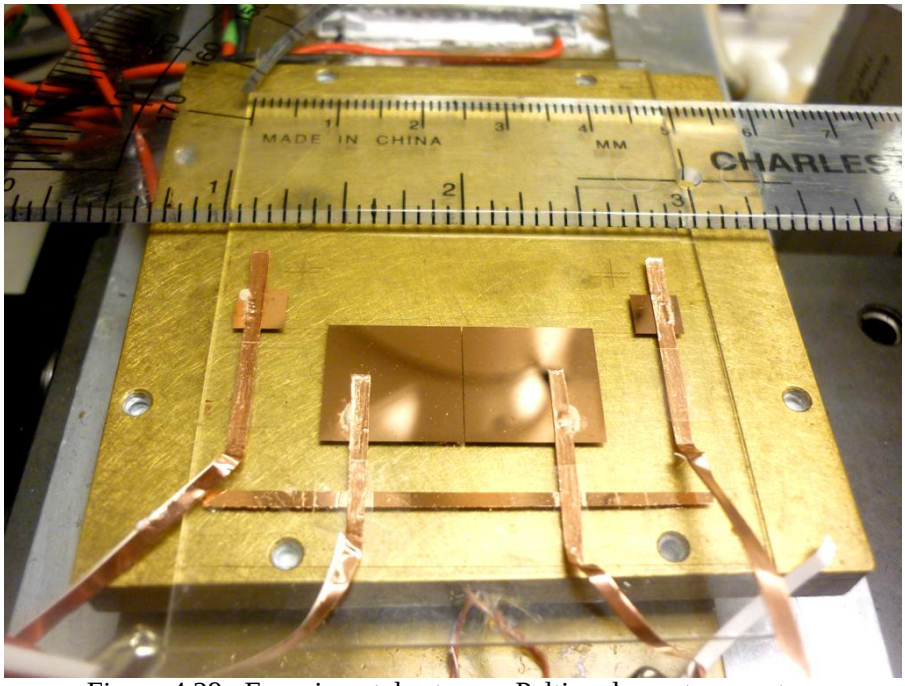

Figure 4.29. Experimental setup on Peltier element apparatus.

In figure 4.29 we show the experimental setup on Peltier element apparatus. We cleaned connecting copper tape by contact cleaner pen, improved connection by a silver containing electrical conductive lubricant and fixed metallic tapes by adhesive tape. Thin glass slide (0.2 mm) with deposited microheater + thick glass (1 mm) are placed on Peltier element at 5°C, thermal contact is provided by silicon oil between flats. When we turn on the Peltier element to have the temperature at 5˚C, this resembles the exact initial conditions of in nucleation experiment. As the Peltier element is running at 5˚C which is much lower than the dew point temperature in the laboratory, we see dew drops from moisture in the air on the surface of the heater as shown in figure 4.30. Now we supply current to the heater through contacts and observe the surface features evolved from the

heating. We observe appearance of small clear circle originating at the position of the heater. The circle clear of dew drops indicates that in the circle the temperature is higher than the dew point and at the edge it becomes equal to the dew point temperature. So we can calculate the radius of the circle and compare it with the simulation results to see if it matches. From different current input we obtain a radius vs. current curve as shown in figure 4.31.

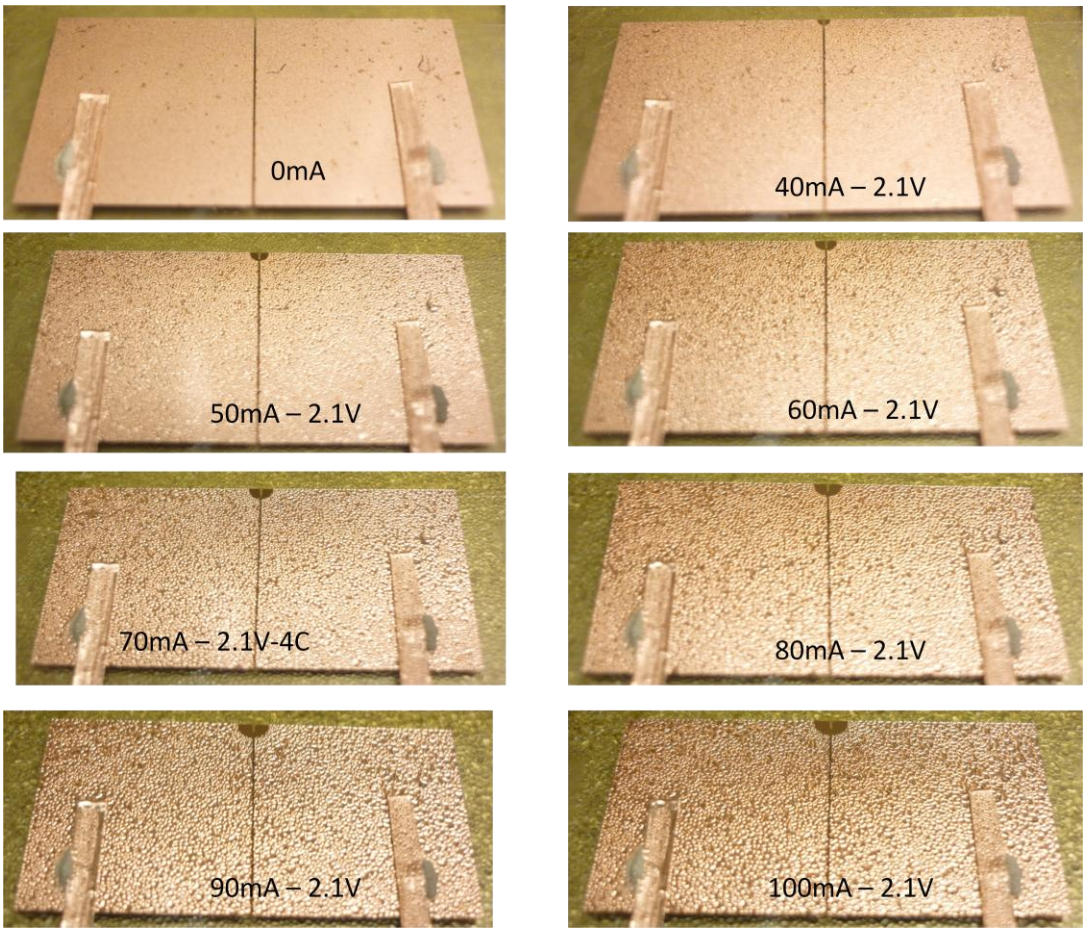

Figure 4.30. The heater surface with dew drops on it and circle originating at the heater centre. The circle indicates the temperature field in which the temperature is higher than the dew point at the laboratory condition. Dew point 16.0 ± 0.1 °C. Peltier element apparatus temperature 4.4 ± 0.1 °C.

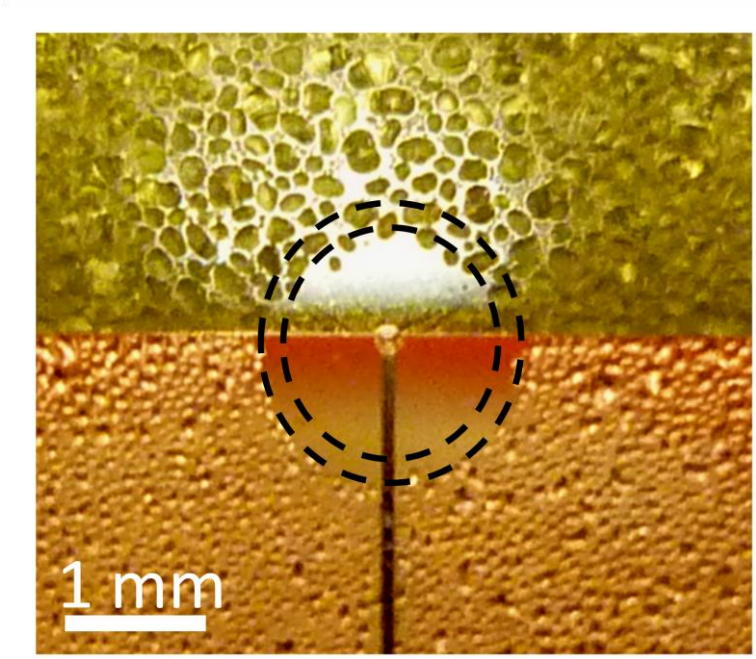

Figure 4.31. Close up view of the dew drop circle on the heater side of the chip for determining the radius of the temperature field.

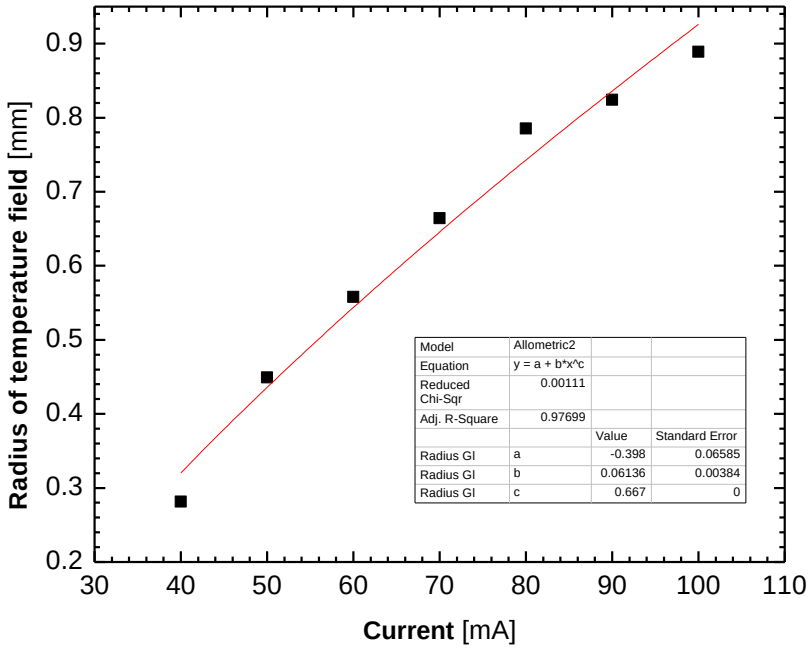

Figure 4.32. Radius of temperature field on the surface as a power function of current.

Now we can compare the data from simulation with the data from experiment in the following manner for heater temperature of 60˚C:

1. First we take the temperature of heater to be 60˚C and find out the required current from curve in figure 3.13. From the curve, the relation between temperature of heater and supplied current at 2.1 volts is as follows:

$$T = 20.6 - 0.006I + 0.001I^2. \qquad (3.2.)$$

So from equation 3.2. we find the current value to be ~200 mA.

2. Now for this value of current (~200 mA) we can find the radius of temperature field at the edge of which the temperature is 16˚C. The value is found to be 1.70 mm.

This calculation is based on the assumption that the heater gives a spherical temperature field. For spherical temperature field from Joule's heating:

$$I^2Rt = C\Delta T\rho(4/3\,\pi r^3), \qquad (3.3.)$$

where I=supplied current, R=resistance of the heater, t=time of current flow, C=specific heat of the substrate, ΔT=temperature difference, r=sphere radius of the temperature field. From this equation we can see that the current would have a 2/3 power dependence on temperature field radius. We find the same relationship from the experimental curve shown in figure 4.32.

3. Now if we compare this result with simulation result (the value is about 0.40 mm as shown in figure 4.26), we can see that the temperature field from experiment is about a factor of 4 larger than it has been estimated from simulation.

This is just a rough estimate. We need to design more experiments to find better comparison with the simulation results.

4.5. Conclusions

In summary, we have formulated the recipe for pattern formation in AZ photoresist layer and final heater fabrication using thermal evaporator. We found that Cu thin film adhesion to glass is enhanced by incorporation of intermediate Cr layer. We calibrated the heater with infrared camera and also with Peltier element apparatus. We found out a break point of power input to the heater where burning of heater occurs due to excessive heat generation. We performed computer simulations to check the effectiveness of our design and improved the design accordingly. Simulation results were compared with an experiment based on dew point temperature.

CHAPTER 5

ASSEMBLY OF MICROFLUIDIC CHANNEL & LOCALIZED MICROHEATER

5.1. Channel pressure and port assembly

The assembly of our microfluidic chip is crucial as the purpose is to pass sickle cell hemoglobin solution and silicone oil through the channel at manageable rates to ensure formation of droplets of HbS solution. We have to use pumps with pressure ranges such that we will able to achieve the liquid flow up to several pL/min. The properties f pump should allow us to create droplets of 2 pL volume. At this moment overcoming capillary effect during ingress of fluid becomes a critical issue due to small micron dimensions of our channel. Application of very high pressure during pumping of fluid lead to separation of substrates and penetration of liquid between the layers instead of liquid passing through the channel. So we were having problem in pumping of liquid from large port into very narrow channel. To overcome this problem we designed a gradually decreasing channel as shown in the following figure.

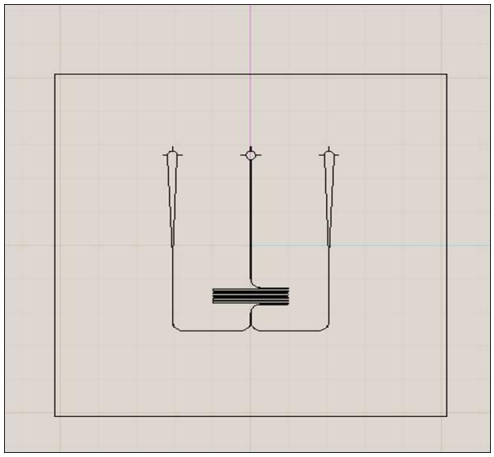

Figure 5.1. The microfluidic device having channels with gradually decreasing width starting from inlet ports.

As the necessary pressure P to push liquid into microchannel is inversely proportional to surface square S under actuating force F

$$P = F/S \qquad (5.1.)$$

Now we know, section of required channel: $5 \cdot 10^{-6}$ m × $40 \cdot 10^{-6}$ m = $2 \cdot 10^{-10}$ m^2 and initial section of gradual entrance: $5 \cdot 10^{-6}$ m × $2 \cdot 10^{-3}$ m = $1 \cdot 10^{-8}$ m^2. So, for the ratio between the pressure exerted in the port of entry to the pressure that is required in the channel, we get $P_2/P_1 = 10^{-2}$. So for the huge change in the pressure the gradual narrowing of the width is crucial.

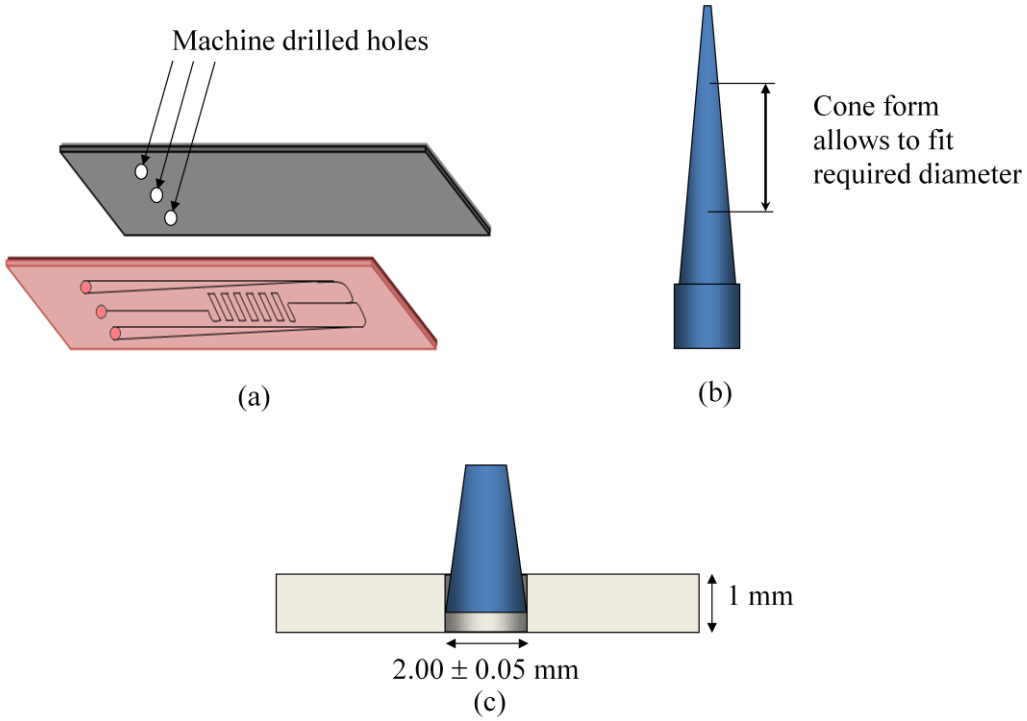

Figure 5.2. (a) Machine drilled holes on the substrate to fit the channel inputs, (b) cone length of the microliter pipette tip to fit the holes and (c) fitting of machined pipette tips into hole.

To manage the high pressure of the liquid at entrance it is necessary for us to have good ports which will help us pass our liquid through our channel. The ports that we use will have to be biocompatible as well. So to fit in the parameters (such as holes in the glass substrates for inlets) we used 1000 μL pipette tips. The cone shaped pipette is cut

into such a way that the broader end would fit the hole in the glass substrate and on the top we can put the proper tubing. It is very important that to attach the ports we use household superglue, because we tried to use several special types of glue. But none of them worked well because most of them do not work with glass and PTFE together. Figure 5.2. illustrates the port management.

5.2. Bonding of two substrates

Assembly of MEMS and microfluidic devices has been of great interest since the invention of MEMS technology to facilitate formation of integrated devices (171). There are several forms of bonding techniques depending on the surface morphology of the substrates and the required bonding strength. The bonding strategies used in the laboratories can be shortlisted as in table 4.1:

Table 5.1. An overview of MEMS & Micorfludics bonding [adapted from Ref. (171)].

Procedure	**Temperature**	**Hermeticity**	**Reliability**
Epoxy bonding	Low	PDMS (No)/SU8(Yes)	Not certain
Eutectic bonding	Medium	Yes	Not certain
Anodic bonding	Medium	Yes	Good
Fusion bonding	Very high	Yes	Good
Integrated process	High	Yes	Good
Low temperature bonding	Low	Not certain	Not certain
Brazing	Very high	Yes	Good

5.2.1. Custom made vice

Considering all the available options, we tried at first to bind the pieces together with small binding clips. Before using binder clips we used oxygen plasma etching to render both the surfaces hydrophilic which would go face to face (i.e., the channel containing polymer layer face of 1 mm microscope glass slide and the face opposite to microheater containing side of 200 μm coverslip). Afterwards we aligned them in DI water and then used the binder clips to hold them together and put them in oven at 100˚C for about 20 minutes (172). We got quite good bonding using this method but the pressure was not sufficient to induce good adhesion throughout the entire surface. Then following the procedure as in Ref. (173), we decided to design a simple custom made vice (as shown in figure 5.3) out of smooth aluminum plates (having surface roughness of 2.5 μm) where the applied bonding pressure is known from the nut pitch and exerted torque from a graduated torque wrench.

Figure 5.3. Custom-made vice made of aluminum plates of high surface roughness (~2.5 μm). The combined chip go in between two plates. The screw on the top is adjustable by torque wrench from which exact applied pressure is known.

The purpose of the device from which we can know the exact applied pressure is that it gives us the option for optimization of applied pressure to the extent which will give us sufficient bonding throughout the polymer layer but will not induce cracking.

5.2.2. Determination of glass transition temperature

With required high pressure we choose also to apply high temperature while the combined chip is under pressure. The idea behind this is to induce adhesion and reflow characteristics among the cured polymer molecules at temperature close to their glass transition temperature (173). For this reason we tried to find out the working temperature range from differential scanning calorimetry (DSC) data from our cured SU-8 samples. Differential scanning calorimeter (DSC) is an equipment which gives the data for phase transition based on the thermal heat capacity change of materials. Basically it calculates the heat intake or release by the sample while the temperature of the sample holder is linearly increased. For amorphous materials, it gives the information about the glass transition temperature (T_g). The glass transition temperature is the temperature at which the amorphous solid attains reflow characteristics. For polymers T_g is a characteristic property.

From DSC data (as shown in figure 5.4), we can see that the best operating temperature would be below 130˚C (T_g of cured SU-8 sample). We did the 1st heating experiment up to 200˚C and found to temperature for phase change. First one was the glass transition temperature (T_g) and the second one is the melting temperature which we confirmed from 2nd heating data. The 2nd heating was done after cooling of sample from 1st heating highest temperature. The second heating did not show any phase change

which means during the first heating the polymer structure was fully destroyed. The knowledge of the T_g has enabled us to better understand the processing conditions using this SU-8 polymer. We also need to maintain the temperature higher than boiling point of water to remove moisture after we have bonded the samples using DI water.

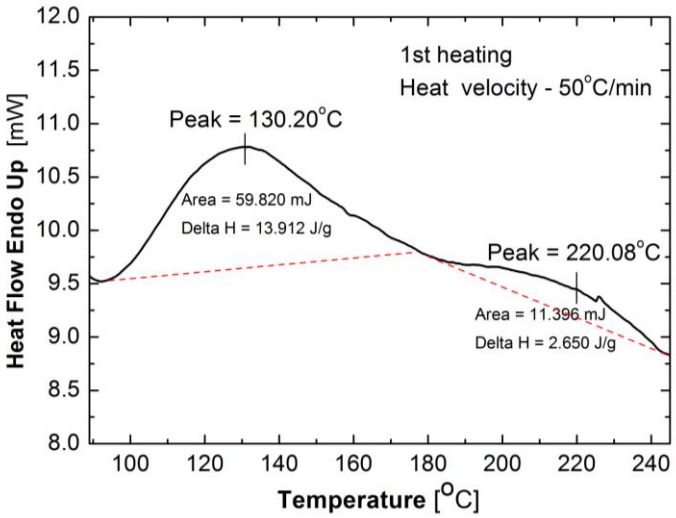

(a)

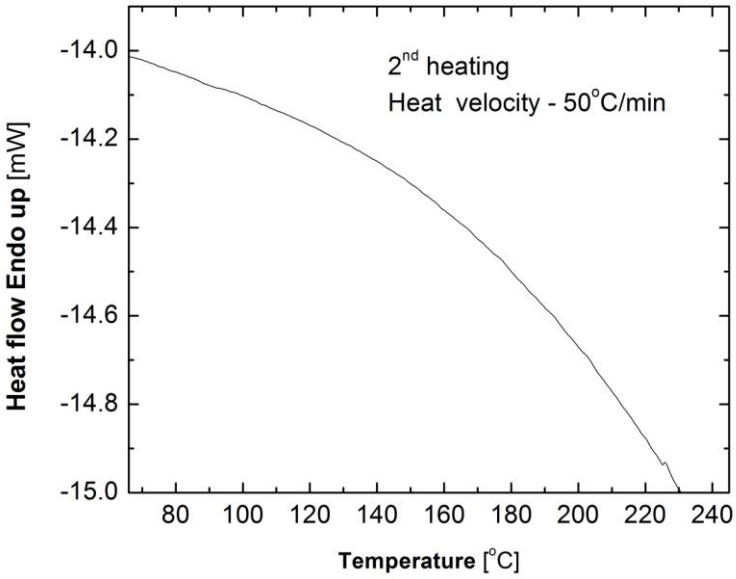

(b)

Figure 5.4. (a) Differential scanning calorimetry data showing glass transition temperature of cured SU-8 polymer during 1st heating and (b) no phase change during 2nd heating after cooling down indicating complete destruction of polymer structure above 200°C during 1st heating.

5.2.3. Bonding torque and temperature relationship

After we got the DSC data, we were able to test the combination of applied pressure on the chip and bonding temperature in which we must operate. So we tested two schemes for putting the chip in between the two surfaces of the custom made vice: (i) only two substrates attached to each other and (ii) having a third substrate (a 1 mm glass slide) on the heater side of the coverslip to protect it from breaking.

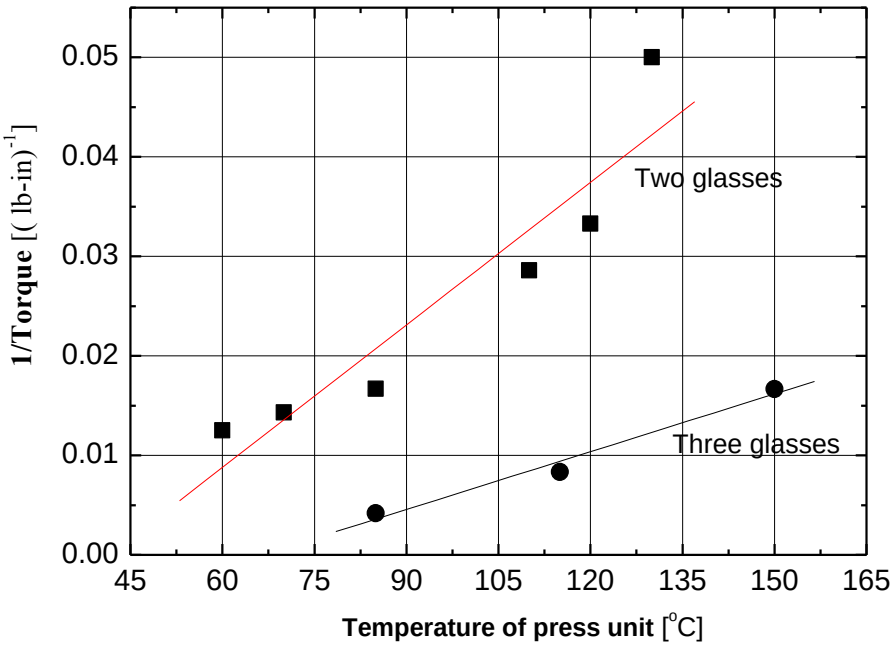

Figure 5.5. Reciprocal relationship between the applicable torque of the custom made vice and bonding temperature. Filled square (■) shows the cracking points when the microfluidic and microheater combine chip is pressed without any support and filled circle (•) shows the cracking points for the assembly with support on the side of the heater.

We first raised the temperature of the custom made vice in convection oven and then we put the combined samples inside the custom made vice and applied pressure from lower to higher ones. After each time we applied the pressure, we checked the sample for cracks and if cracks were found, we noted the temperature and pressure. We

measured the temperature of the custom made vice with Omega HH506R thermometer. Thus we got reciprocal dependence of applied torque on temperature of the custom made vice. From this curves (as shown in figure 5.5), we can optimize the applicable pressure and temperature under which cracking of the samples would not occur.

From the relationship between torque and temperature, we decided to test different temperature and pressure condition under which it would be safe to operate. After several trials we found a processing condition of 200 lb-in of torque at 100˚C. But when we examined the channel geometry, we found that the channel had melted and had been closed by the melted portion. Then after few trials we found that the final operating condition for obtaining good bonding would be to pressurize at first the samples with the custom made vice with 180 lb-in torque to confirm the flatness of the samples and then to lower the torque to 50 lb-in and bake in the oven at 100˚C for an hour.

5.2.4. Oxygen plasma treatment and SU-8 surface roughness

Though the required pressures were enough to combine the two chips together initially, the resulting bonded chips did not have good alignment. Then we decided to use oxygen plasma treatment using RIE 80 machine in UH nanofabrication facility. We wanted to use oxygen plasma to have good alignment of the samples initially through some increased adhesion in the layer initially. Oxygen plasma induces hydrophilicity and also increases surface roughness (174). Subjecting the SU-8 layer and glass coverslip to oxygen plasma we increase surface roughness and hydrophilicity to induce adhesion.

We also characterized SU-8 surface roughness through AFM imaging of SU-8 layer. We found that surface roughness depends on the plasma power more than it

depends on time for the same given energy. The more the power of the plasma, the higher the surface roughness as can be seen from figure 5.6. So it is advisable to use less power to avoid excess roughness.

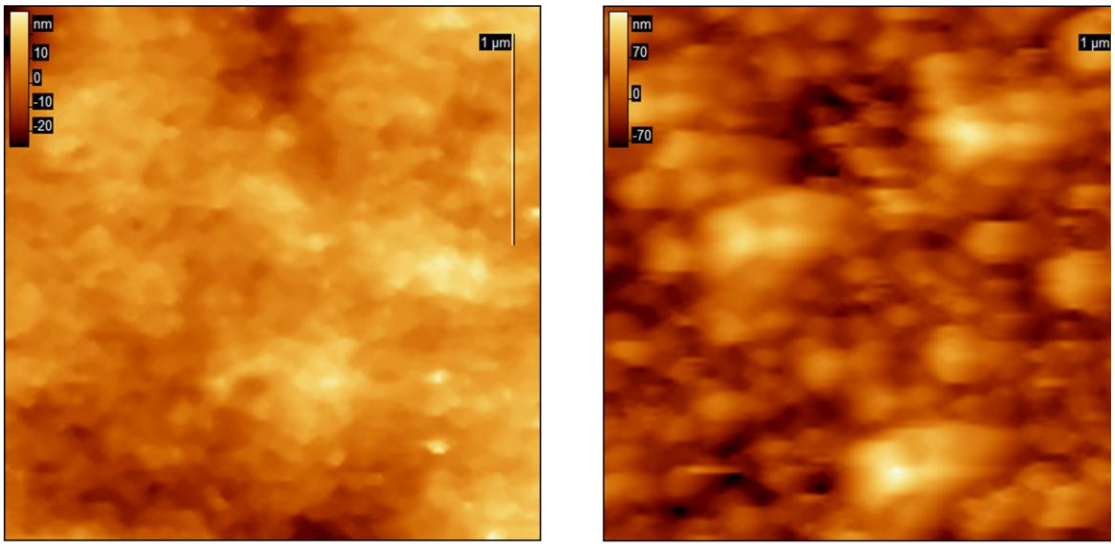

Figure 5.6. AFM characterization of SU-8 surface. It is clear that for 50W, 720 s combination the surface roughness is lower than for 300W, 120 s combination which indicates towards strong dependence of surface roughness on oxygen plasma power.

Table 5.2. Values of surface roughness of cured SU-8 3005 polymer layer from AFM characterization.

SU-8	**Roughness (nm) of 1 µm^2 scan area**	**Roughness (nm) of 100 µm^2 scan area**
Untreated	0.84	7.75
50 W, 720 s	6.98	23.73
300 W, 120 s	39.06	54.41

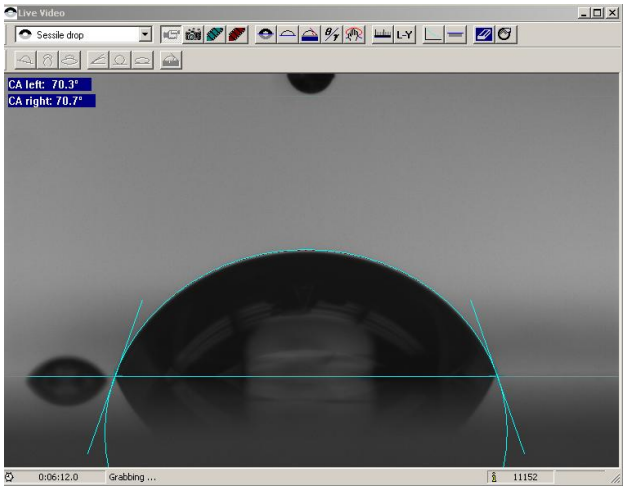

(a)

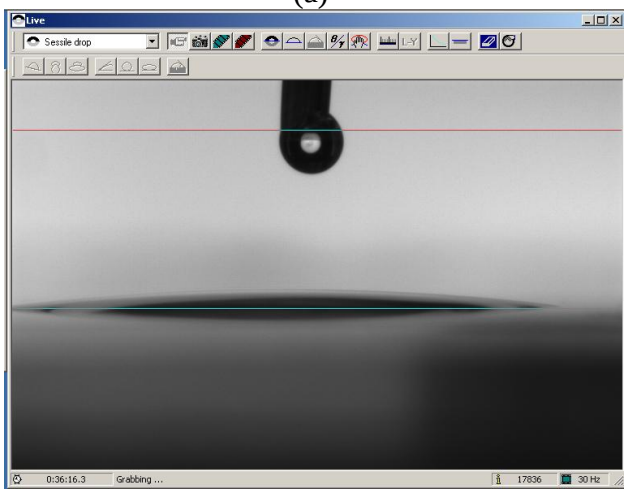

(b)

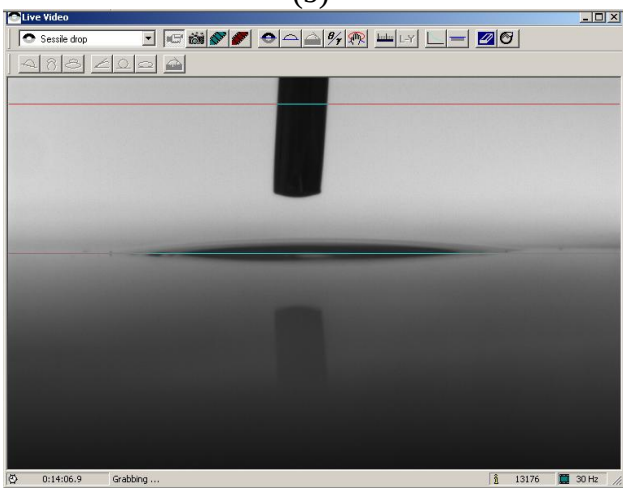

(c)

Figure 5.7. (a) Untreated SU-8 3005 sample having contact angle of 70˚. (b) and (c) show the flatness of water droplet on SU-8 surface immediately after oxygen plasma treatment having conditions of 50W×80s and 300W×30s, respectively.

Due to oxygen plasma treatment SU-8 3005 surface is charged by active C=O and COO group, which modifies wetting of polymer surface to hydrophilicity [1, 2]. For characterizing SU-8 surface roughness and hydrophilicity, we also used contact angle measurement. We measured contact angles of several samples of SU-8 which differed in oxygen plasma treatment power and duration. We found that the untreated SU-8 layer had contact angle of about 70˚, while the treated samples had very low contact angles. We also observe the response of hydrophilicity of treated SU-8 layers. We see that the induced hydrophilicity reduces as the days pass. This observation confirms that the adhesion between the substrates in the final chip would decrease with increasing time. From table 5.3, we can see that just after oxygen plasma, all the three different samples (differing in plasma intensity not in energy) have almost the same values of contact angles and the values are almost 10 times smaller than the untreated contact angles. The hydrophilicity was so strong that the machine was not able to calculate the contact angles for some instances due to lack of curvature (as can be seen from figure 4.7). It is also seen that as the time progresses the contact angles increase indicating loss of hydrophilicity.

Table 5.3. Wetting of SU-8 samples (Contact angle values (degree)~±2°).

Time/Treatment condition	**Untreated Sample**	**300W×30s**	**100W×90s**	**50W×180s**
0 day (1 hour)	70	7.5	8.8	9.2
3 days		18.5	28.8	33.2
7 days		28.4	35.2	38.3

5.2.5. Manual cleaning of channel

Before bonding the samples, it is very important to make sure that there is no dust particle inside the channel. Because if there is any, it may hinder the primary purpose of the microfluidics device i.e., flow through channel. For this reason we have found a unique way to clean the channel under optical microscope with the help of cactus needles. Sharpness of the end of such needle should be about 2 um like a lot of others similar bio-objects. Such size allows us to use it for 20-40 μm microchannel cleaning easily under optical microscope.

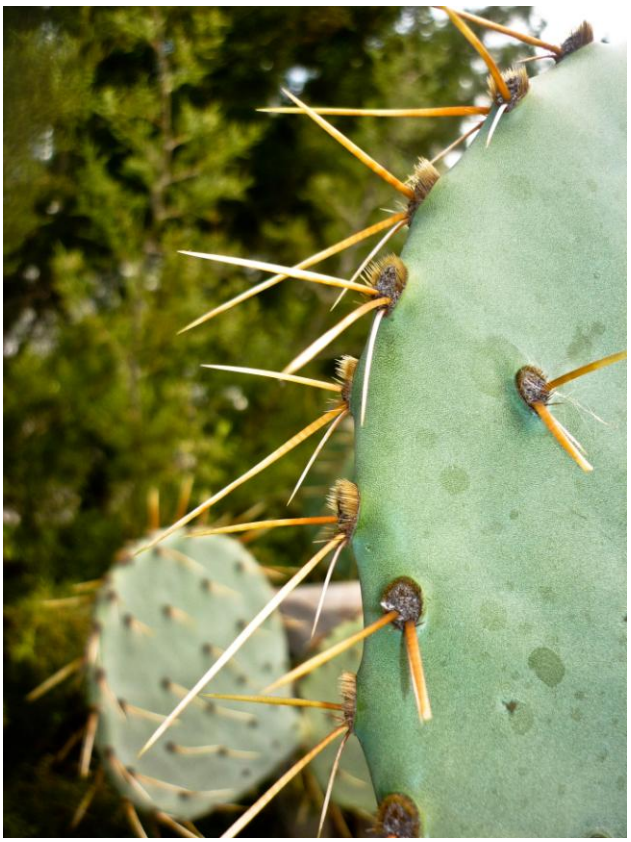

Figure 5.8. Sharp needles (thickness of tip~2μm) of cactus used for manual cleaning of channels before bonding.

5.3. Final recipe and ready chip

The final recipe was developed after lots of experimentations and comparing numerous successful and unsuccessful bound chip. The bonding strecgth of the chip depends on the area of the chip which are bound together and from figure 5.9 (a) & (b) we cna see examples of unsuccessful and successful bonding, respectively. The white area in the chip shoes the bound area and the other parts are not bonded well enough.

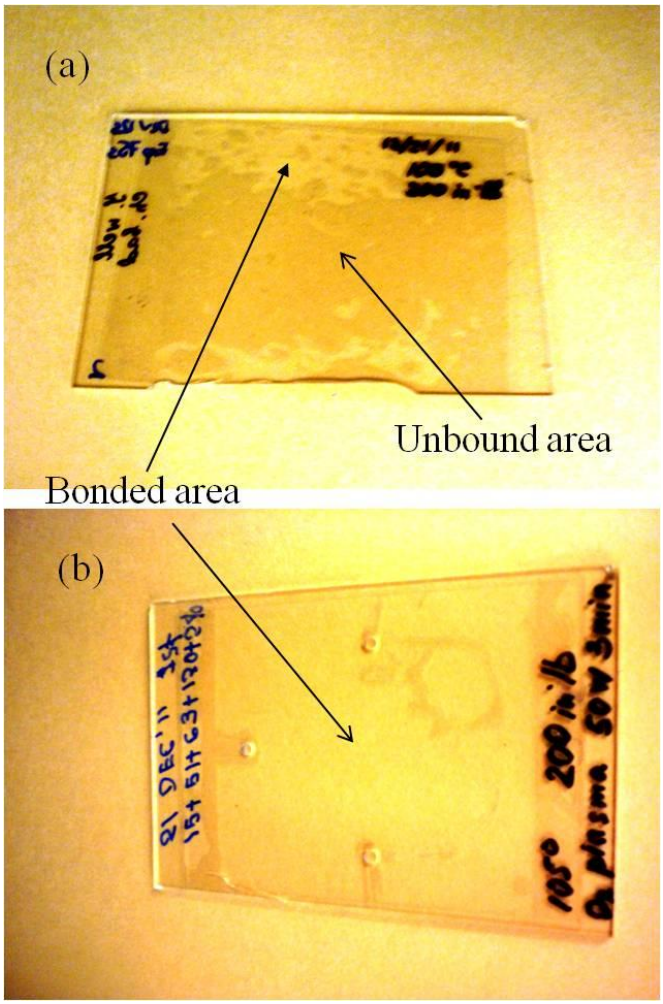

Figure 5.9. (a) Unsuccessful bonding showing large unbound area and (b) successful bonding.

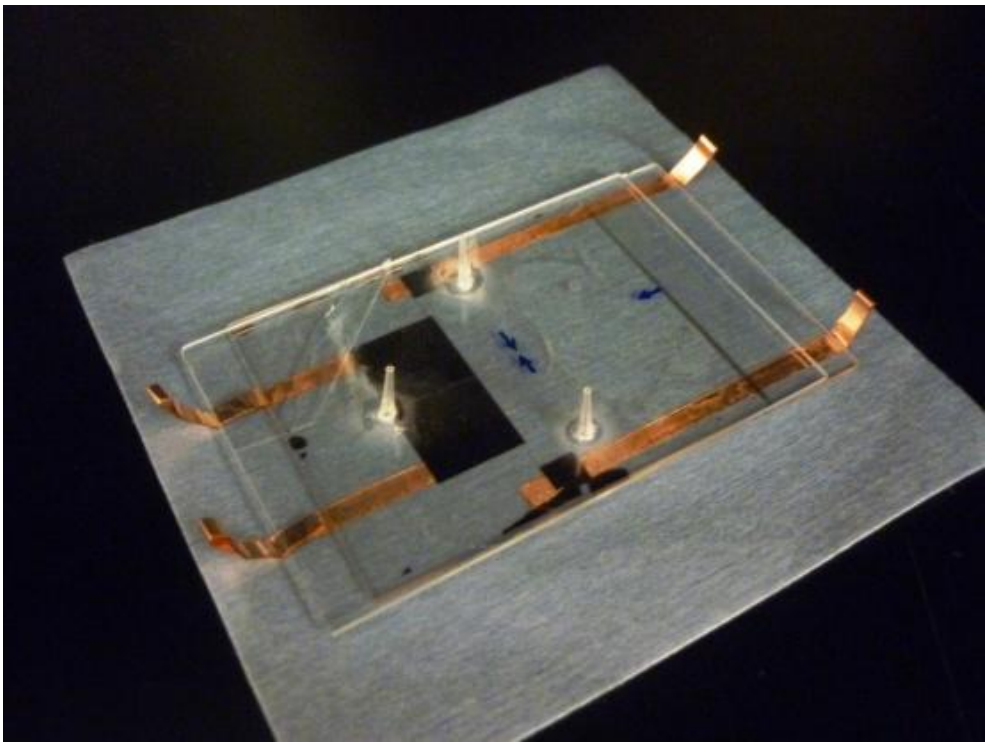

Figure 5.10. The final bonded chip with both microfluidic channel and microheater.

Finally, we arrive at the following recipe which would give us reliable bonding:

1. First we treat the bonding surfaces with oxygen plasma using 50W power for 180 s.
2. Immediately (within 2-5 minutes) after oxygen plasma treatment, we align the microfluidic channel and microheater in DI water.
3. Then we use the custom made vice to apply 180 lb-in torque to the sandwich sample to ensure nanoscale flatness of SU-8 layer.
4. We reduce the pressure to 50 lb-in and put the vice with the sample into convection oven for heating up to 105˚C for about 1 hour to ensure complete removal of moisture and good adhesion.
5. After we take out the vice and release the sample from its jaw and examine for the bonded areas.

Figure 5.11. Reactive ion etching machine (RIE 80) in UH Nanofabrication Facility for oxygen plasma treatment.

Figure 5.12. Convection ovens in UH Nanofabrication Facility used in baking during bonding.

5.4. Conclusions

In summary, for bonding the microheater and microfluidic channel together we designed a custom made vice and also characterized the bonding pressure and temperature. We found a way of reinforcing the bonding configuration by having another glass substrate as support. We observed shift in melting point of cured SU-8 under high pressure. Thus two step pressing recipe is formulated.

CHAPTER 6

MANAGEMENT & CONTROL OF MICROFLUIDIC CHIP

The management of the microfluidic device is still under progress and there are several schemes and sectors which we are looking into at this moment. Our goal is to prepare a fully automated experimental setup where the flow of the fluids, temperature egress, nucleation experiment and microscopy etc. will be controlled centrally in a computer control module.

6.1. Liquid flow in microchannel

At present we are trying to achieve droplet flow inside the microfluidic chip. The final bonded chip is also shown in figure 6.1. The final chip contains the fluidic connections with ports and tubings.

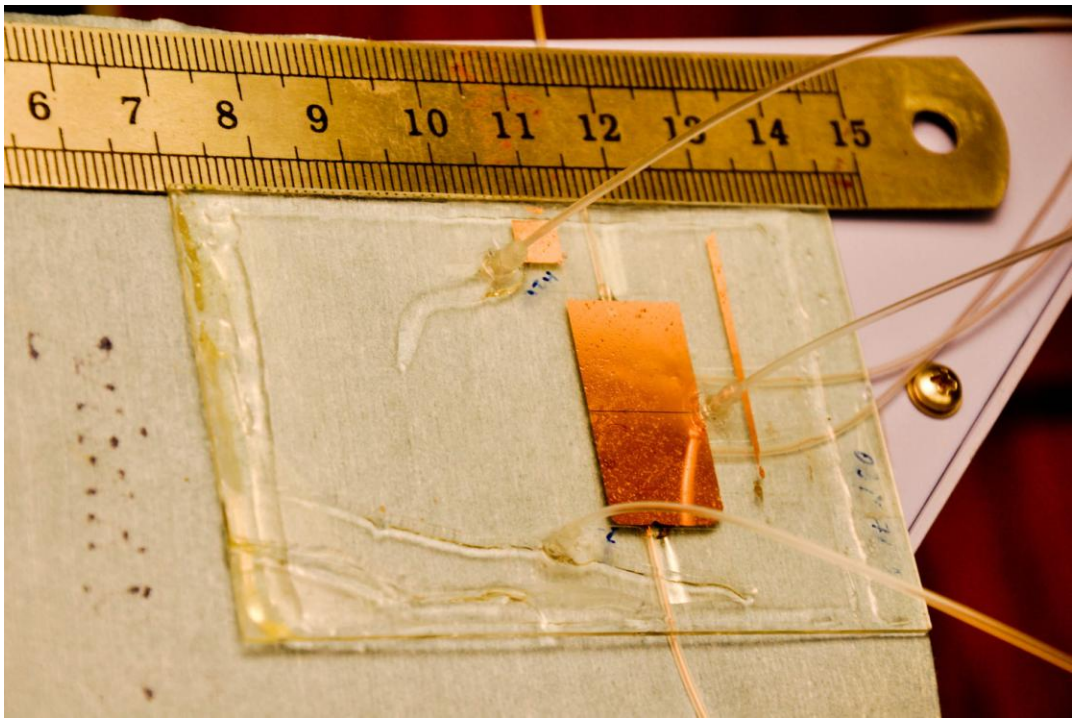

Figure 6.1. Final bonded microfluidic chip with ports and tubings for fluid flow.

We tried to observe the channel over the heater in the conjugated sample. The bright field images are shown in figure 6.2(a, b) and one DIC (differential interference contrast microscopy) image (figure 6.2(c)) shows the liquid in the channel. It is crucial for us to have DIC imaging as the HbS fibers are only visible with DIC imaging.

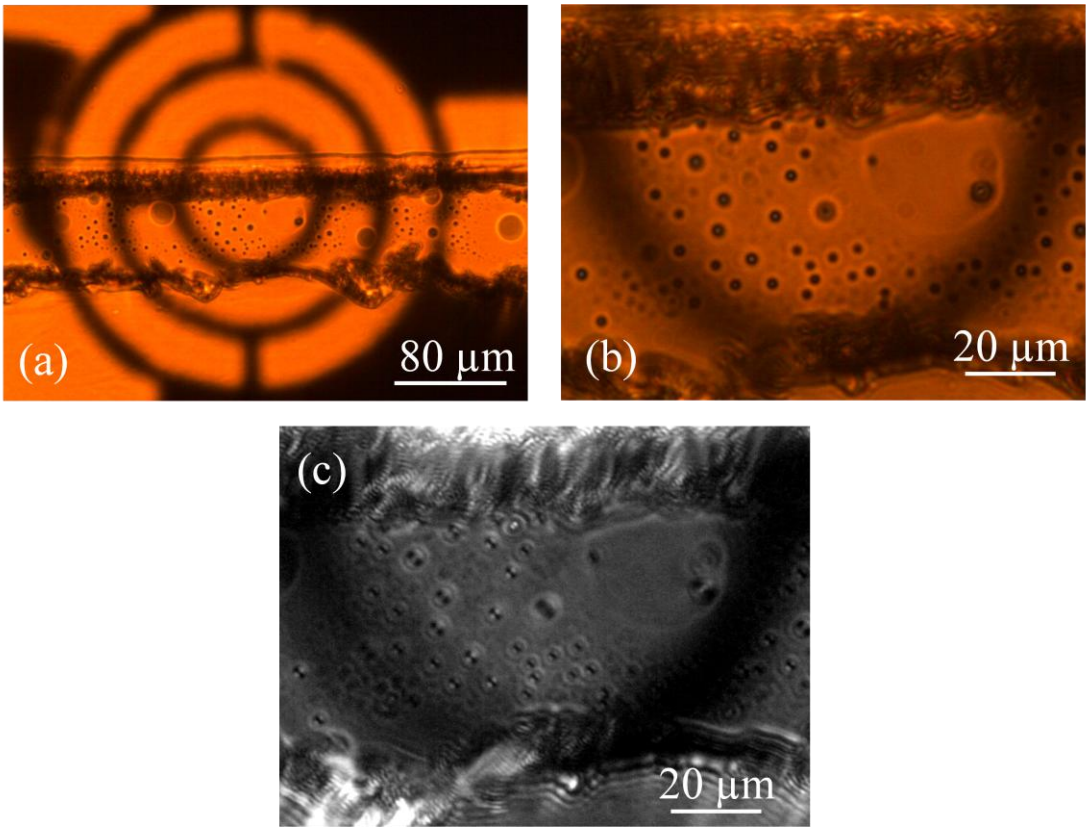

Figure 6.2. The geometry of channel (of not so good sample) and silicone oil in the channel. (a) shows the channel geometry with heater geometry in the background in bright field imaging through 20× objective lens, (b) shows silicone in the channel imaged in bright field with 63× objective lens and (c) shows clearer image of silicone oil in the channel in DIC mode with 63× objective lens.

We also observed water plug movement (as model liquid instead of HbS aqueous solution) by the carrier fluid silicone oil. Figure 6.3 shows the movement of plug. Though we are yet to improve required size of the droplets through manipulation of flow rates of silicone oil and water, we confirmed the possibility of droplet formation in our channel by this observation.

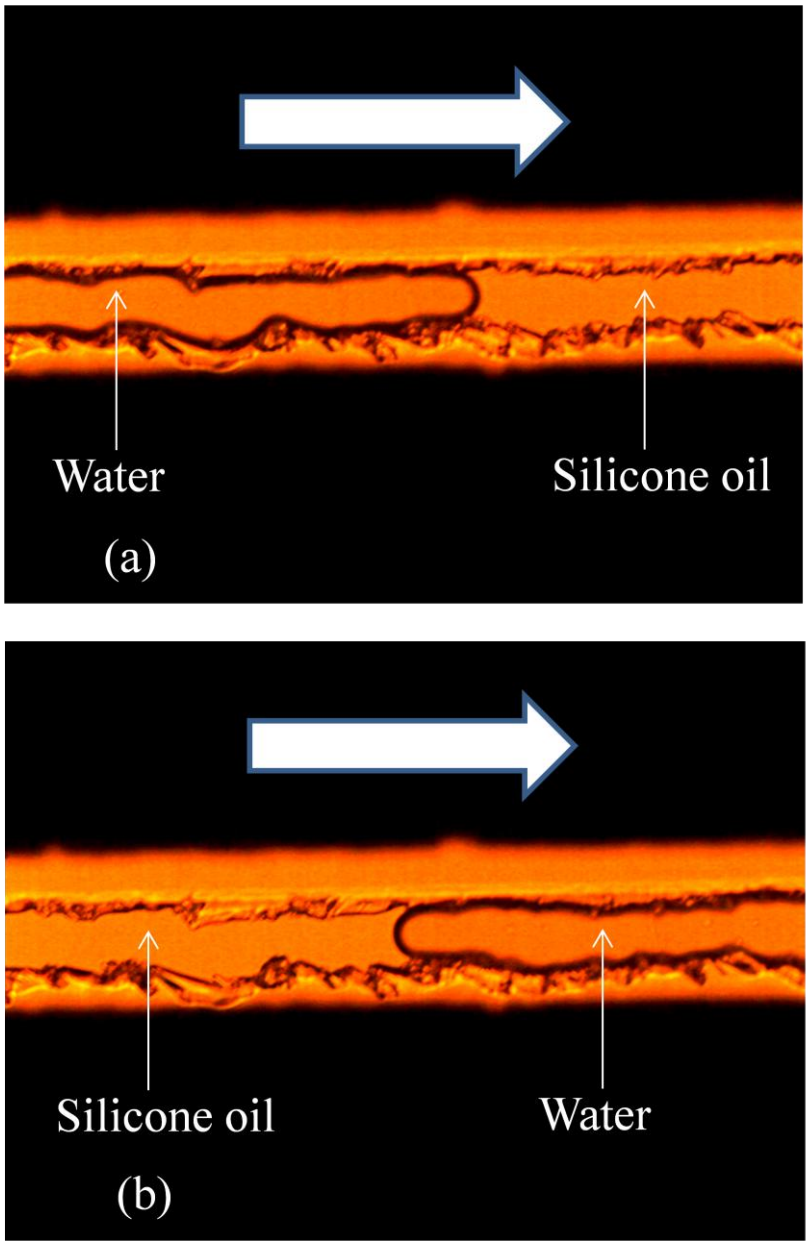

Figure 6.3. Flow of water plug encapsulated by carrier fluid silicone oil. (a) shows the entering of the water plug in the field of view of 20× objective lens from left. (b) shows water plug leaving the field of view from left to right.

6.2. Control of microfluidics and LabView

To generate droplets and control their size distribution, we need to have full control over the flow rates of the liquids involved. For the fluidic control we use two

Harvard PHD Ultra pumps as shown in figure 6.4. We have developed a LabView program to simultaneously control the pumping of the liquids.

Figure 6.4. Harvard PHD Ultra pumps used for controlling flow rate of liquid into microchannel.

For the temperature control at first we decided to employ PID control scheme to our setup. Primary idea was to measure the resistance values of the heater and then to convert it to temperature values using calibration curves; after that to compare the values with the desired set point and provide PID feedback to the power source to generate required power. But the time required for the temperature ramp should be on the order of tens of milliseconds. PID control requires feedback from the system and with so small timescale it is quite difficult to communicate among voltage measuring device (NI 6361), computer and power source. For this reason we decided to use open loop current supply where we will first raise the temperature to the desired value with higher current supply in orders of tens of milliseconds and then lower the current supply to maintain the temperature at the set point. This will basically be not a control system rather it will be a management system where without any feedback we will set the parameters such that the system reaches the set point.

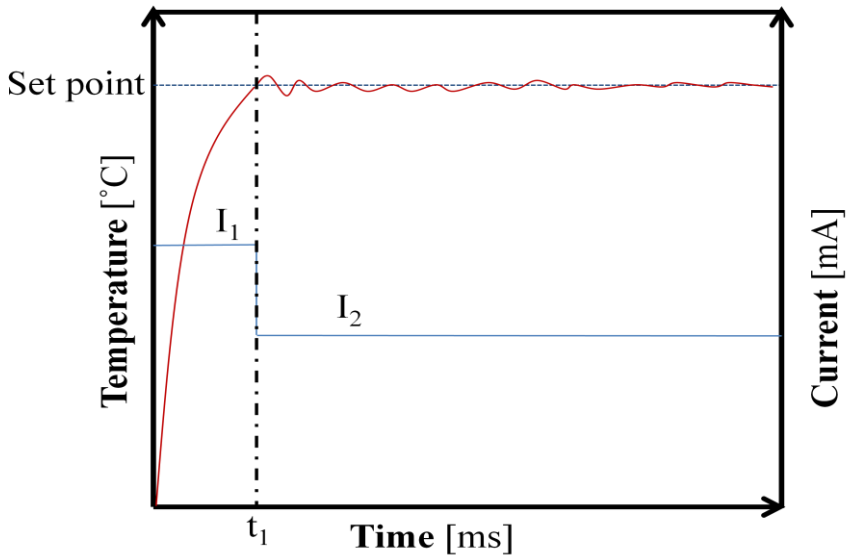

Figure 6.5. Graphical representation of proposed temperature management scheme for achieving required supersaturation of HbS solution. I_1 current will be supplied to reach the temperature set point in time t_1 and then another current I_2 will be supplied to maintain the temperature at the set point.

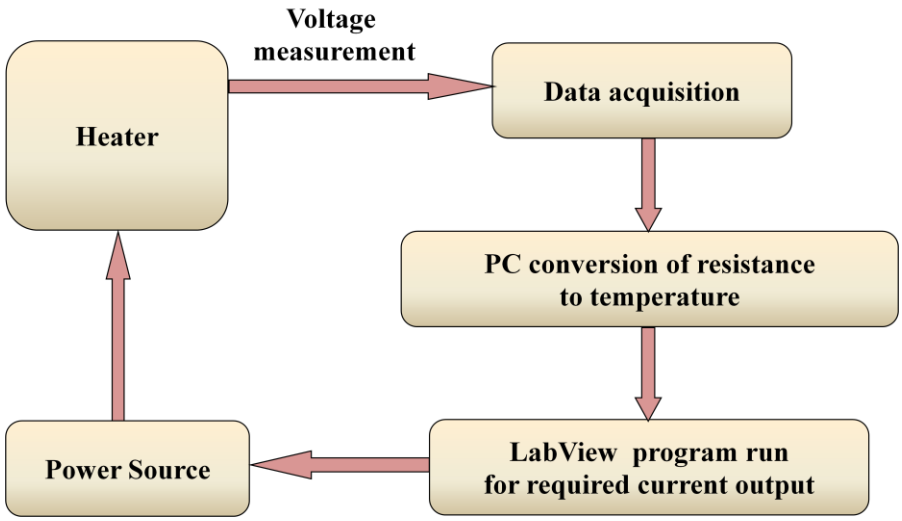

Figure 6.6. Schematic of temperature management for HbS nucleation experiment.

We developed separate LabView codes for managing the pumps, for the voltage measurement device and also to operate the power source (Keithley 2400). We are yet to combine the codes together to formulate the overall control scheme. We provide a representative code below.

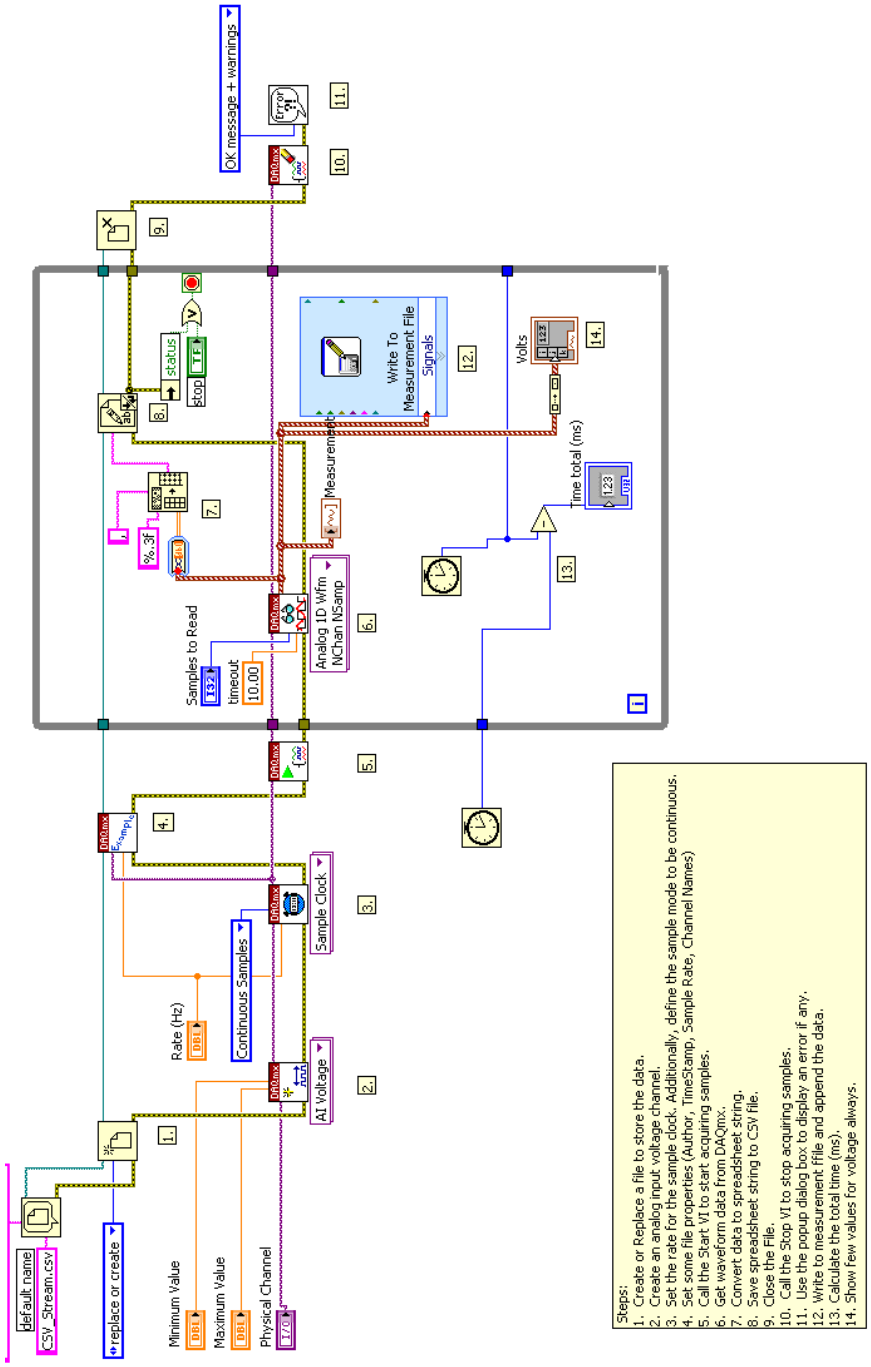

Figure 6.7. LabView code for voltage measurement with NI-6361.

6.3. Conclusions

We observed liquid flow in channel with bright field and DIC microscopy. We have outlined and generated LabView codes for fluidic control and temperature management.

CHAPTER 7

CONCLUSIONS & FUTURE WORKS

7.1. Overall conclusions

1. We have designed and developed microfluidic chip for study of sickle cell hemoglobin (HbS) polymerization.
2. We have developed microfluidic channel and localized microheater preparation recipes and optimized the parameters involved.
3. We calibrated the microheater with both infrared camera and Pettier element apparatus. We carried out computer simulations and compared with experimental results to some extent.
4. We achieved bonding parameters to provide good adhesion between substrates.
5. We observed plug flow of liquids in the microfluidic channel and proposed LabView control of microfluidics and temperature management.

7.2. Future works

7.2.1. Improvements of nucleation kinetics experimental setup

As we are trying to develop an automated microfluidic system for observation of nucleation of sickle cell hemoglobin polymers, a lot of work is yet to be accomplished. At present we have finished the primary stage of developing the fabrication procedures of microfluidics chip and characterization of different parameters regarding the temperature calibration for heating process. The issues which we need to deal with in the future have a wide spectrum. We are discussing here the initiatives we are taking to address these issues.

1. We need to further test the current recipe for channel fabrication and characterize the parameters involved to have better reproducibility of samples. We will look into the exposure and baking conditions and optimize them to provide better resolution of channel dimensions.
2. We need to change the design of the microchannel junction to have more control over the droplet size. At present our design contains Y-junction where silicone oil and aqueous solution of HbS meet. We intend to use either T-junction or flow focusing (as shown in figure 7.1.) to improve the droplet dynamics and size control parameters.

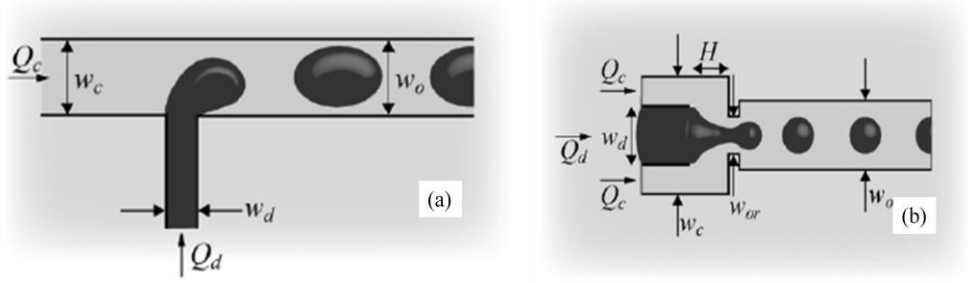

Figure 7.1. Channel junction geometries intended to use in future: (a) T-junction & (b) flow focusing type junction.

3. We need to design reliable experiments to find out the temperatures of the heater upon applying current. We need to know whether our results coincide with the simulations performed. In this way we can validate our assumptions regarding the modeling during simulation.
4. We need to find better connection method for wiring the lids of the microheater with power source and voltage measurement device. Because the current copper tape-alligator clip combination is not stable enough to produce consistent measurements.

5. We need to improve and combine the LabView codes for faster temperature ramping and data processing and control. Also pumping needs to be integrated to make it an automated system.

7.2.2. Improving method of free heme determination

In chapter 1, we discussed about the role of free heme in sickle cell hemoglobin polymerization. It is evident that free heme has significant effect on HbS polymerization by inducing thermodynamic interaction forces among the HbS and itself. Our group demonstrated that addition of heme in heme-free HbS solution induces higher rates of polymerization. It is also evident that removing free heme from HbS solution arrests polymerization. Our group used spectroscopic method to determine the level of free heme present in HbS solution (5). But the method resulted in very low sensitivity (~10 μm) and high level of error (~50%). So it is important to find a reliable and sensitive method for determining free heme concentration in solutions.

Current method of heme determination which we are investigating is based on chemiluminescence of luminol by Horseradish peroxidase enzyme reconstituted with free heme in the solution. Chemiluminescence is one form of luminescence among several kinds which occurs due to the effect of a chemical reaction taking place in the system and this reaction produces an intermediate excited substance which emits light before it goes to the stable the stable state. The emission of light is mostly in visible spectrum. Here we use Horseradish peroxidase (HRP) enzyme (14) which acts as an electron donor for the hydrogen peroxide and would contribute to the cleavage of the hydrogen peroxide to have hydroxyl ions those will react with the luminol to produce light emitting product.

Basically HRP is a hemoprotein which can be found in commercial form without the heme group in it. This is known as Apo-peroxidase. This apo-peroxidase, when comes in contact with the heme molecule in a solution, can reconstitute themselves to peroxidase and gain the enzymatic activity. This is the basis for the present experiment which allows direct measurement of heme concentration in any solution from the intensity of the chemiluminescent reaction between luminol and hydrogen peroxide under the catalysis of peroxidase. The intensity is directly proportional to the rate of reaction which is, in turn, proportional to the available enzymes following the heme-apo-peroxidase reconstitution reaction. Thus it gives a direct measurement of heme concentration that is present in the solution and unknown concentrations can be determined using the standard curves obtained from known concentration. So our aim is to improve this method of heme determination and use it in conjunction with HbS nucleation experiment to confirm our hypothesis of free heme effect on HbS polymerization.

REFERENCES

1. Beutler, E. (2001) The sickle cell diseases and related disorders. in *Williams Hematology, 6th Edition* (Beutler, E., Lichtman, M. A., Coller, B. S., Kipps, T. J., and Seligsohn, U. eds.), McGraw Hill, New York. pp 581-605.
2. Vekilov, P. (2007) *Brit. J. Haematol.* **139**, 173-184.
3. (2003) *Red Cell Membrane Transport in Health and Disease* 1 edition ed., Springer.
4. Pawliuk, R., Westerman, K. A., Fabry, M. E., Payen, E., Tighe, R., Bouhassira, E. E., Acharya, S. A., Ellis, J., London, I. M., Eaves, C. J., Humphries, R. K., Beuzard, Y., Nagel, R. L., and Leboulch, P. (2001) *Science* **294**, 2368-2371.
5. Uzunova, V. V., Pan, W., Galkin, O., and Vekilov, P. G. (2010) *Biophys. J.* **99**, 1976-1985.
6. Hebbel, R. P., Morgan, W. T., Eaton, J. W., and Hedlund, B. E. (1988) *Proceedings of the National Academy of Sciences* **85**, 237-241.
7. Liu, S. C., Zhai, S., and Palek, J. (1988) *Blood* **71**, 1755-1758.
8. Voet, D., and Voet, J. G. (1997) *Biochemistry*, 2nd ed., John Wiley & Sons Ltd.
9. Hazelwood, L. F. (2001) *Can't Live Without It: The Story of Hemoglobin in Sickness and in Health* 1st ed., Nova Publishers.
10. Perutz, M. F., Rossmann, M. G., Cullis, A. F., Muirhead, H., Will, G., and North, A. C. T. (1960) *Nature* **185**, 416-422.
11. Ranney, H. M., and Sharma, V. (2001) Structure and Function of Hemoglobin. in *Williams Hematology, 6th Edition* (Beutler, E., Lichtman, M. A., Coller, B. S., Kipps, T. J., and Seligsohn, U. eds.), McGraw Hill, New York. pp 345-353.

12. http://bio3400.nicerweb.com/Locked/media/ch14/protein_structure-quaternary.html.

13. Uzunova, V. V. (2010) Free Heme and Sickle Cell Hemoglobin Polymerization. in *Department of Chemical & Biomolecular Engineering*, University of Houston, Houston.

14. Takahashi, S., and Masuda, T. (2009) *COMBINATORIAL CHEMISTRY & HIGH THROUGHPUT SCREENING* **12**, 532-535.

15. Gelin, B. R., Lee, A. W.-M., and Karplus, M. (1983) *Journal of Molecular Biology* **171**, 489-559.

16. Dill, K., and Bromberg, S. (2003) *Molecular Driving Forces: Statistical Thermodynamics in Chemistry and Biology*, Garland Science, New York.

17. Cannon, J. B., Kuo, F., Pasternack, R. F., Wong, N. M., Muller-Eberhard, U. (1984) *Biochemistry* **23**, 3715-3721.

18. Tipping, E., Ketterer, B., Christodoulides, L. (1979) *Biochem. J.* **180**, 327-337.

19. Ginsburg, H., Demel, R. A. (1983) *Biochimica et Biophysica Acta* **732** 316-319.

20. Solar, I., Shaklai, N. (1989) *Biochemica et Biophysica Acta* **983**, 199-204.

21. Leclerc, L., Vasseur, C., Bursaux, E., Marden, M., Poyart, C. (1988) *Biochimica et Biophysica Acta* **946** 49-56.

22. Jarolim, P., Lahav, M., Liu, S., Palek, J. (1990) *Blood* **76**, 2125-2131.

23. Chou, A. C., Fitch, C. D. (1980) *J. Clin. Invest.* **66**, 856-858.

24. Kirschner-Zilber, I., Rabizadeh, E., Shaklai N. (1982) *Biochimica et Biophysica Acta* **690**, 20-30.

25. Orjih, A. V., Banyal, H. S., Chevli, R., Fitch, C.D. (1981) *Science* **214**, 667-669.

26. Fitch, C. D., Chevli, R., Banyal, H. S., Philips, G., Pfaller, M. A., Krogstad, D. J. . (1982) *Antimicrobial Agents and Chemotherapy*, 819-822.

27. Goldstein, L., Teng, Z., Zeserson, E., Patel, M., Regan, R. F. (2003) *Journal of Neuroscience Research* **73**, 113–121.

28. Vanderveldt, G. M., Regan, R. M. (2004) *Free Radical Research* **38**, 431-437.

29. Bhoite-Solomon, V., Kessler-Icekson, G., Shaklai, N. (1993) *In Vitro Cellular & Developmental Biology - Animal* **29**, 636-642.

30. Jacob, H. S., Brain, M. C., Dacie, J. V., Carrell, R. W., Lehmann, H. (1968) *Nature* **218**, 1214-1217.

31. Janney, S. K., Heinrich Joist, J., Fitch, C. D. (1986) *Blood* **67**, 331-333.

32. Miller, Y. I., Shaklai, N. (1999) *Biochimica et Biophysica Acta* **1454**, 153-164.

33. Miller, Y. I., Felikman, Y., Shaklai, N. (1995) *Biochimica et Biophysica Acta* **1272**, 119-127.

34. Eaton, W. A., Henry, E. R., Hofrichter, J., and Mozzarelli, A. (1999) *Nature Structural Biology* **6**, 351.

35. Goldman, L., and Ausiello, D. A. (2008) *Cecil Medicine*, Saunders Elsevier.

36. Perutz, M. F., Wilkinson, A. J., Paoli, M., and Dodson, G. G. (1998) *Annual Review of Biophysics and Biomolecular Structure* **27**, 1-34.

37. Vekilov, P. G. (2008) *Aiche J.* **54**, 2508-2515.

38. http://www.nhlbi.nih.gov/health/health-topics/topics/sca/.

39. Higgins, J. M., Eddington, D. T., Bhatia, S. N., and Mahadevan, L. (2007) *Proceedings of the National Academy of Sciences* **104**, 20496-20500.

40. Stuart, M. J., and Nagel, R. L. (2004) *Lancet* **364**, 1343-1360.

41. Herrick, J. (2001) *Yale J Biol Med.* **74**, 179-184.

42. Pauling, L., Itano, H. A., Singer, S. J., and Wells, I. C. (1949) *Science* **111**, 543-548.

43. Ingram, V. M. (1956) *Nature* **178**, 792-794.

44. Noguchi, C. T. (2008) Pathophysiology of Sickle Cell Anemia: Hemoglobin S Polymerization.

45. Li, S., and Sun, B. (2011) *Advances in Cell Mechnics*, Springer.

46. Eaton, W. A., and Hofrichter, J. (1990) Sickle cell hemoglobin polymerization. in *Advances in protein chemistry* (Anfinsen, C. B., Edsal, J. T., Richards, F. M., and Eisenberg, D. S. eds.), Academic Press, San Diego. pp 63-279.

47. Wishner, B., Ward, K., Lattman, E., and Love, W. (1975) *J. Mol. Biol.* **98**, 179-194.

48. Dykes, G. W., Crepeay, R. H., and Edelstein, S. J. (1978) *Nature* **272**, 506-510.

49. Dykes, G. W., Crepeay, R. H., and Edelstein, S. J. (1979) *J. Mol. Biol.* **130**, 451-472.

50. Pan, W., Galkin, O., Filobelo, L., Nagel, R. L., and Vekilov, P. G. (2007) *Biophys. J.* **92**, 267-277.

51. Cao, Z., and Ferrone, F. A. (1996) *J Mol Biol* **256**, 219-222.

52. Cao, Z., and Ferrone, F. A. (1997) *Biophys J* **72**, 343-352.

53. Cao, Z., Liao, D., Mirchev, R., Martin de Llano, J. J., Himanen, J. P., Manning, J. M., and Ferrone, F. A. (1997) *J Mol Biol* **265**, 580-589.

54. Hofrichter, J., Ross, P. D., and Eaton, W. A. (1976) *Proc. Natl. Acad. Sci. USA.* **73**, 3035-3039.

55. Ross, P. D., Hofrichter, J., and Eaton, W. A. (1977) *J. Mol. Biol.* **115**, 111-134.

56. Hofrichter, H., Ross, P. D., and Eaton, W. A. (1974) *Proc. Natl. Acad. Sci. USA* **71**, 4864-4868.

57. Ferrone, F. A., Hofrichter, H., and Eaton, W. A. (1985) *J. Mol. Biol.* **183**, 611-631.

58. Ferrone, F. A., Hofrichter, H., and Eaton, W. A. (1985) *J. Mol. Biol.* **183**, 591-610.

59. Ueda, Y., and Bookchin, R. M. (1984) *J Lab Clin Med* **104**, 146-159.

60. Platt, O. S., Orkin, S. H., Dover, G., Beardsley, G. P., Miller, B., and Nathan, D. G. (1984) *J Clin Invest* **74**, 652-656.

61. Brugnara, C. (2001) *Blood Cells Mol Dis* **27**, 71-80.

62. Eaton, W. A., and Hofrichter, J. (1995) *Science* **268**, 1142-1143.

63. Bridges, K. R., Barabino, G. D., Brugnara, C., Cho, M. R., Christoph, G. W., Dover, G., Ewenstein, B. M., Golan, D. E., Guttmann, C. R., Hofrichter, J., Mulkern, R. V., Zhang, B., and Eaton, W. A. (1996) *Blood* **88**, 4701-4710.

64. Eaton, W. A. (2003) *Biophys Chem* **100**, 109-116.

65. Eaton, W. A., and Hofrichter, J. (1987) *Blood* **70**, 1245-1266.

66. Abraham, D. J., Gazze, D. M., Kennedy, P. E., and Mokotoff, M. (1984) *J Med Chem* **27**, 1549-1559.

67. Abraham, D. J., Kennedy, P. E., Mehanna, A. S., Patwa, D. C., and Williams, F. L. (1984) *J Med Chem* **27**, 967-978.

68. Perutz, M. F., and Lehmann, H. (1968) *Nature* **219**, 902-909.

69. Manning, J. M., and Acharya, A. S. (1984) *Am J Pediatr Hematol Oncol* **6**, 51-54.

70. Mehanna, A. S. (2001) *Current Medicinal Chemistry* **8**, 79-88.

71. Ohnishi, S. T. (1994) Introduction. in *Membrane Abnormalities in Sickle Cell Disease* (Ohnishi, S. T., and Ohnishi, T. eds.), CRC Press, Boca Raton. pp 2-17.

72. Hebbel, R. P. (1991) *Blood* **77**, 214-237.

73. Embury, S. H. (2004) *Microcirculation* **11**, 101–113.

74. Serjeant, G. R., Petch, M. C., and Serjeant, B. E. (1973) *J Lab Clin Med* **81**, 850-856.

75. Coletta, M., Hofrichter, J., Ferrone, F. A., and Eaton, W. A. (1982) *Nature* **300**, 194-197.

76. el-Hazmi, M. A. (1992) *Acta Haematol* **88**, 67-71.

77. Amin, B. R., Bauersachs, R. M., Meiselman, H. J., Mohandas, N., Hebbel, R. P., Bowen, P. E., Schlegel, R. A., Williamson, P., and Westerman, M. P. (1991) *Hemoglobin* **15**, 247-256.

78. Weatherall, M. W., Higgs, D. R., Weiss, H., Weatherall, D. J., and Serjeant, G. R. (2005) *Clin Lab Haematol* **27**, 384-390.

79. Manodori, A. B., Matsui, N. M., Chen, J. Y., and Embury, S. H. (1998) *Blood* **92**, 3445-3454.

80. Hebbel, R. P. (1997) *J. Clin. Invest.* **99**, 2561-2564.

81. Hebbel, R. P., Osarogiagbon, R., and Kaul, D. (2004) *Microcirculation* **11**, 129-151.

82. Hebbel, R. P. (2004) *Microcirculation* **11**, 99-100.

83. Vichinsky, E. (2002) *The Lancet* **360**, 4350-4356.

84. Ferrone, F. A. (2004) *Microcirculation* **11**, 115-128.

85. Kaul, D., Fabry, M., and Nagel, R. (1989) *Proc. Natl. Acad. Sci. USA* **86**, 3356-3360.

86. Rioual, F., Biben, T., and Misbah, C. (2004) *Phys Rev E* **69**, 061914.

87. Fischer, T. M. (2007) *Biophys J* **93**, 2553-2561.

88. Briehl, R. W., and Nikopoulou, P. (1993) *Blood* **81**, 2420-2428.

89. Samuel, R. E., Guzman, A. E., and Briehl, R. W. (1993) *Blood* **82**, 3474-3481.

90. Koduri, P. R., Leon, M., Honig, G. R., and Lu, S. J. (1999) *Am J Hematol* **62**, 62-62.

91. Samuel, R. E., Salmon, E. D., and Briehl, R. W. (1990) *Nature* **345**, 833-835.

92. Briehl, R. W. (1995) *J. Mol. Biol.* **245**, 710-723.

93. Galkin, O., Nagel, R. L., and Vekilov, P. G. (2007) *J. Mol. Biol.* **365**, 425-439.

94. Galkin, O., and Vekilov, P. G. (2004) *J. Mol. Biol.* **336**, 43–59.

95. Galkin, O., Chen, K., Nagel, R. L., Hirsch, R. E., and Vekilov, P. G. (2002) *Proc. Natl. Acad. Sci. USA* **99**, 8479-8483.

96. Rotter, M. A., Kwong, S., Briehl, R. W., and Ferrone, F. A. (2005) *Biophysical Journal* **89**, 2677-2684.

97. Vekilov, P. G. (2005) Kinetics and Mechanisms of Protein Crystallization at the Molecular Level. in *Methods in Molecular Biology, vol. 300: Protein Nanotechnology, Protocols, Instrumentation, and Applications* (Vo-Dinh, T. ed.), Humana Press, Totowa, NJ. pp 15-52.

98. Vekilov, P. G., Galkin, O., Pettitt, B. M., Choudhury, N., and Nagel, R. L. (2008) *J Mol Biol* **377**, 882-888.

99. Fronticelli, C., and Gold, R. (1976) *J Biol Chem* **251**, 4968-4972.

100. Carrager, B., Bluemke, D. A., Gabriel, B., Potel, M. J., and Josephs, R. (1988) *Journal of Molecular Biology* **199**, 315-331.

101. Choudhury, N., and Pettitt, B. M. (2005) *J. Am. Chem. Soc.* **127**, 3556-3567.

102. Choudhury, N., and Pettitt, B. M. (2005) *J. Phys. Chem. B* **109**, 6422 -6429.

103. Choudhury, N., and Pettitt, B. M. (2006) *J. Phys. Chem. B* **110**, 8459-8463.

104. Reviakine, I., Georgiou, D. K., and Vekilov, P. G. (2003) *J. Am. Chem. Soc.* **125**, 11684-11693.

105. Elhadj, S., De Yoreo, J. J., Hoyer, J. R., and Dove, P. M. (2006) *PNAS* **103**, 19237-19242.

106. Galkin, O., Pan, W., Filobelo, L., Hirsch, R. E., Nagel, R. L., and Vekilov, P. G. (2007) *Biophys. J.* **92**, 902-913.

107. Galkin, O., and Vekilov, P. G. (2000) *Proc. Natl. Acad. Sci. USA* **97**, 6277-6281.

108. Anderson, V. J., and Lekkerkerker, H. N. W. (2002) *Nature* **416**, 811 - 815.

109. ten Wolde, P. R., and Frenkel, D. (1997) *Science* **277**, 1975-1978.

110. Vekilov, P. G. (2004) *Crystal Growth and Design* **4**, 671-685.

111. Lutsko, J. F., and Nicolis, G. (2006) *Phys. Rev. Lett.* **96**, 046102.

112. Shiryayev, A., and Gunton, J. D. (2004) *Journal of Chemical Physics* **120**, 8318-8326.

113. Lomakin, A., Asherie, N., and Benedek, G. B. (2003) *Proc. Natl. Acad. Sci. USA* **100**, 10254-10257.

114. Vivares, D., Kaler, E., and Lenhoff, A. (2005) *Acta Crystallogr D Biol Crystallogr*. **61**, 819-825.

115. Pan, W., Kolomeisky, A. B., and Vekilov, P. G. (2005) *J. Chem. Phys.* **122**, 174905.

116. Filobelo, L. F., Galkin, O., and Vekilov, P. G. (2005) *J. Chem. Phys.* **123**, 014904.

117. Leunissen, M. E., Christova, C. G., Hynninen, A.-P., Royall, C. P., Campbell, A. I., Imhof, A., Dijkstra, M., van Roij, R., and van Blaaderen, A. (2005) *Nature* **437**, 235-240.

118. Garetz, B., Matic, J., and Myerson, A. (2002) *Phys. Rev. Lett.* **89**, 175501.

119. Aber, J. E., Arnold, S., and Garetz, B. A. (2005) *Phys. Rev. Lett.* **94**, 145503.

120. Qian, R. Y., and Botsaris, G. D. (2004) *Chemical Engineering Science* **59**, 2841-2852.

121. Gower, L. B. (2008) *Chemical Reviews* **108**, 4551-4627.

122. Krishnan, R., and Lindquist, S. L. (2005) *Nature* **435**, 765-772.

123. Gliko, O., Neumaier, N., Pan, W., Haase, I., Fischer, M., Bacher, A., Weinkauf, S., and Vekilov, P. G. (2005) *J. Amer. Chem. Soc.* **127**, 3433-3438.

124. Gliko, O., Pan, W., Katsonis, P., Neumaier, N., Galkin, O., Weinkauf, S., and Vekilov, P. G. (2007) *J. Phys. Chem. B* **111**, 3106-3114.

125. Stradner, A., Sedgwick, H., Cardinaux, F., Poon, W. C. K., Egelhaaf, S. U., and Schurtenberger, P. (2004) *Nature* **432**, 492-495.

126. SanBiagio, P. L., and Palma, M. U. (1991) *Biophysical J.* **60**, 508-512.

127. Manno, M., Biagio, P. L. S., and Palma, M. U. (2004) *PROTEINS: Structure, Function, and Bioinformatics* **55**, 169–176.

128. Angell, C. A. (1995) *Science* **267**, 1924-1935.

129. Frauenfelder, H., Sligar, S., and Wolynes, P. (1991) *Science* **254**, 1598-1603.

130. Jones, C. W., Wang, J. C., Ferrone, F. A., Briehl, R. W., and Turner, M. S. (2003) *Faraday Discussions* **123**, 221-235.

131. Falk, J. E. (1964) *Porphyrins and Metalloporphyrins*, Elsevier Publishing Company.

132. Nguyen, N. T., and Wereley, S. T. (2006) *Fundamentals and Applications of Microfluidics*, Artech House Inc.

133. Whitesides, G. M. (2006) *Nature* **442**, 368-373.

134. Shiku, H., Saito, T., Wu, C.-C., Yasukawa, T., Yokoo, M., Abe, H., Matsue, T., and Yamada, H. (2006) *Chemistry Letters* **35**, 234-235.

135. Lorenz, H., Despont, M., Fahrni, N., LaBianca, N., Renaud, P., and Vettiger, P. (1997) *Journal of Micromechanics and Microengineering* **7**, 121.

136.http://www.inems.com/mems_course_area/02_fabrication/miniaturization/patterntransfer/Photolithography/Photolithography.htm.

137. Lorenz, H., Laudon, M., and Renaud, P. (1998) *Microelectronic Engineering* **41-42**, 371-374.

138. Zhang, X., Du, L., Zhu, Y., and Liu, C. (2011) *Micro & Nano Letters* **6**, 397-401.

139. Lorenz, H., Despont, M., Fahrni, N., Brugger, J., Vettiger, P., and Renaud, P. (1998) *Sensors and Actuators A: Physical* **64**, 33-39.

140. Che-Hsin, L., Gwo-Bin, L., Bao-Wen, C., and Guan-Liang, C. (2002) *Journal of Micromechanics and Microengineering* **12**, 590.

141. Yang, R., and Wang, W. (2005) *Sensors and Actuators B: Chemical* **110**, 279-288.

142. Audrain, M. T. (2008) Evaluation of SU-8 AND Ruthenium Oxide: Materials for Microfluidic Devices. in *Department of Materials Science and Engineering*, Missouri University of Science and Technology.

143. Del Campo, A., and Arzt, E. (2008) *Chemical Reviews* **108**, 911-945.

144. http://www.sigmaaldrich.com/catalog/product/aldrich/654027?lang=en&region=US.

145. http://www.pherobase.com/database/floral-compounds/floral-taxa-compounds-detail-gamma-butyrolactone.php.

146. Carlier, J., Arscott, S., Thomy, V., Fourrier, J. C., Caron, F., Camart, J. C., Druon, C., and Tabourier, P. (2004) *Journal of Micromechanics and Microengineering* **14**, 619.

147. Shaw, J. M., Gelorme, J. D., LaBianca, N. C., Conley, W. E., and Holmes, S. J. (1997) *IBM Journal of Research and Development* **41**, 81-94.

148. www.microchem.com.

149. Abgrall, P., Conedera, V., Camon, H., Gue, A.-M., and Nguyen, N.-T. (2007) *Electrophoresis* **28**, 4539-4551.

150. Saito, T., Wu, C.-C., Shiku, H., Yasukawa, T., Yokoo, M., Ito-Sasaki, T., and Abe, H. (2006) *The Analyst* **131**, 1006-1011.

151. Kyu-Youn, H., Chin-Sung, P., Joon-Ho, K., Kahp-Yang, S., Eun-Chul, C., and Nam, H. (2010) *Journal of Micromechanics and Microengineering* **20**, 117001

152. Kohlmeier, T., and Gatzen, H. H. (2002) *Journal of Magnetism and Magnetic Materials* **242-245, Part 2**, 1149-1152.

153. Shirtcliffe, N. J., Aqil, S., Evans, C., McHale, G., Newton, M. I., Perry, C. C., and Roach, P. (2004) *Journal of Micromechanics and Microengineering* **14**, 1384.

154. Zhang, J., Tan, K. L., and Gong, H. Q. (2001) *Polymer Testing* **20**, 693-701.

155. Thomas, A. A., Anders, M. J., Dan, A. Z., and Jörg, H. (2006) *Journal of Micromechanics and Microengineering* **16**, 1819.

156. Liu, G., Tian, Y., and Kan, Y. (2005) *Microsyst. Technol.* **11**, 343-346.

157. Vestergaard, R. K., and Bouwstra, S. (2000) *Microsyst. Technol.* **6**, 214–217.

158. Anhoj, T. A., Jorgensen, A. M., Zauner, D. A., and Hübner, J. (2006) *Journal of Micromechanics and Microengineering* **16**, 1819.

159. Tanaka, T., Morigami, M., and Atoda, N. (1993) *Japanese Journal of Applied Physics* **32**, 6059.

160. Lee, S. J., Shi, W., Maciel, P., and Cha, S. W. (2003) Top-edge profile control for SU-8 structural photoresist. in *University/Government/Industry Microelectronics Symposium, 2003. Proceedings of the 15th Biennial.*

161. Williams, J. D., and Wang, W. (2004) *J. Microlithogr. Microfabr.Microsyst.* **3**, 563–568.

162. Hwa Seng, K., Kuo-Kang, L., and Fan-Gang, T. (2003) *Journal of Micromechanics and Microengineering* **13**, 822.

163. Aslam, M., and Hatfield, J. V. (2003) Fabrication of thin film microheater for gas sensors on polyimide membrane. in *Sensors, 2003. Proceedings of IEEE.*

164. Spannhake, J., Schulz, O., Helwig, A., Krenkow, A., Müller, G., and Doll, T. (2006) *Sensors* **6**, 405-419.

165. Hwang, W.-J., Shin, K.-S., Roh, J.-H., Lee, D.-S., and Choa, S.-H. (2011) *Sensors* **11**, 2580-2591.

166. Junghoon, Y., Christopher, R. F., Byunghoon, B., Richard, I. M., and Mark, A. S. (2008) *Journal of Micromechanics and Microengineering* **18**, 125001.

167. Williams, L. D., Okandan, M., and Blair, S. (2008) *J. Micro-Nanolithogr. MEMS MOEMS* **7.**

168. Lee, H. Y., Moon, S., Park, S. J., Lee, J., Park, K. H., and Kim, J. (2008) *Electronics Letters* **44**, 1460-1461.

169. Cai, Z., Li, X., Hu, Q., and Zeng, X. (2009) *Materials Science and Engineering: B* **157**, 15-19.

170. Wasa, K., Kitabatake, M., and Adachi, H. (2004), William Andrew.

171. Hsu, T.-R. (2004) *MEMS Packaging*, The Institute of Electrical Engineers.

172. Yu-Tzu, C., and Denz, L. (2007) *Journal of Micromechanics and Microengineering* **17**, 1978.

173. Serra, S. G., Schneider, A., Malecki, K., Huq, S. E., Brenner, W., and Campus, I. (2007) *Science And Technology* **2035**, 11-14.

174. Walther, F., Heckl, W. M., and Stark, R. W. (2008) *Applied Surface Science* **254**, 7290-7295.